Turun yliopisto
University of Turku

THE SUPERMASSIVE BINARY BLACK HOLE SYSTEM OJ287

Pauli Pihajoki

TURUN YLIOPISTON JULKAISUJA – ANNALES UNIVERSITATIS TURKUENSIS
Sarja - ser. AI osa - tom. 492 | Astronomica - Chemica - Physica - Mathematica | Turku 2014

University of Turku

Faculty of Mathematics and Natural Sciences
Department of Physics and Astronomy
University of Turku
FI-20014 Turku
Finland

Supervised by

Prof. Mauri Valtonen
FINCA
University of Turku
Finland

Reviewed by

Dr. Tuomas Savolainen
Max Planck Institute for Radio Astronomy
Max Planck Society
Germany

Dr. Peter Johansson
Department of Physics
University of Helsinki
Finland

Opponent

Prof. Jochen Heidt
Landessternwarte Königstuhl
University of Heidelberg
Germany

The originality of this thesis has been checked in accordance with the University of Turku quality assurance system using the Turnitin OriginalityCheck service.

ISBN 978-951-29-5790-3 (PRINT)
ISBN 978-951-29-5791-0 (PDF)
ISSN 0082-7002
Painosalama Oy - Turku, Finland 2014

Acknowledgements

This thesis, both the introduction and the research articles, have my name on them and are considered to be my work. In actuality, this thesis is a synthesis of efforts, not only by those whose names appear on the introduction and the articles, but also many others who have contributed indirectly, since no man is an island after all. Many of these numerous contributors will be left out by necessity of brevity, but for these unnamed contributions I am no less grateful.

Foremost, I extend my gratitude to my supervisor, Prof. Mauri Valtonen. He presented me with the topic of my research, contributed significantly to the articles, and advised me whenever I had misunderstood something, had a gap in my knowledge or had blundered something in general.

I wish to thank my esteemed opponent, Prof. Jochen Heidt, for agreeing to travel to Finland to present his assessment of my thesis. Likewise, my thanks to Dr. Tuomas Savolainen and Dr. Peter Johansson for their valuable effort in reviewing this work.

I am also grateful for the work done by all of my collaborators, without which major parts of the research could not have been done. I am particularly indebted to all the observers for the data on OJ287 that I have had the pleasure to use. My thanks to Esko Gardner as well, for valiantly trying to catch all my grammar mistakes.

I would also like to thank Seppo Mikkola, who supervised my Master's thesis, and ignited the interest I now have in things both numerical and theoretical. I also thank Juha-Pekka Pellonpää, who was similarly involved in my Master's thesis, and to whom I owe much of the occasional moments of clarity concerning a multitude of theoretical issues. My thanks also to Heikki Salo for his advice on numerical simulations.

Major financial support for this thesis was provided by the Turku University Foundation and Magnus Ehrnrooth Foundation, and for this I am very grateful. I also thank University of Turku and Aalto University for

employment as a scientist.

The work on this thesis was not done *in vacuo*, but rather in the comfortable atmosphere of Tuorla Observatory. The fine people at the Observatory contributed much to the quality of my working environment, especially via the coffee table and lunch discussions on a great variety of esoteric topics. My thanks to everyone who have partaken in these small events.

Likewise, the company and support of my circle of friends has been invaluable. My thanks to the old crew and the new crew. You know who you are.

I also wish to express my general gratitude for all the giants, some listed in the bibliography, whose shoulders I have clambered onto to steal a peek. In addition, a very special thanks to Marcus, Lucius and Eckhart for important insights not related to the subject at hand.

Finally, my thanks to my family for their perpetual support. Isä, äiti, kiitos kaikesta.

Turku, January 2014
Pauli Pihajoki

Everything is fitting for me, my Universe, which fits thy purpose.

Marcus Aurelius, Meditations, Book IV, 23
(transl. A. S. L. Farquharson)

Contents

Abstract

This doctoral thesis concerns the active galactic nucleus (AGN) most often referred to with the catalogue number OJ287. The publications in the thesis present new discoveries of the system in the context of a supermassive binary black hole model. In addition, the introduction discusses general characteristics of the OJ287 system and the physical fundamentals behind these characteristics. The place of OJ287 in the hierarchy of known types of AGN is also discussed.

The introduction presents a large selection of fundamental physics required to have a basic understanding of active galactic nuclei, binary black holes, relativistic jets and accretion disks. Particularly the general relativistic nature of the orbits of close binaries of supermassive black holes is explored with some detail. Analytic estimates of some of the general relativistic effects in such a binary are presented, as well as numerical methods to calculate the effects more precisely. It is also shown how these results can be applied to the OJ287 system.

The binary orbit model forms the basis for models of the recurring optical outbursts in the OJ287 system. In the introduction, two physical outburst models are presented in some detail and compared. The radiation hydrodynamics of the outbursts are discussed and optical light curve predictions are derived. The precursor outbursts studied in Paper III are also presented, and tied into the model of OJ287.

To complete the discussion of the observable features of OJ287, the nature of the relativistic jets in the system, and in active galactic nuclei in general, is discussed. Basic physics of relativistic jets are presented, with additional detail added in the form of helical jet models. The results of Papers II, IV and V concerning the jet of OJ287 are presented, and their relation to other facets of the binary black hole model is discussed.

As a whole, the introduction serves as a guide, though terse, for the physics and numerical methods required to successfully understand and simulate a close binary of supermassive black holes. For this purpose, the

introduction necessarily combines a large number of both fundamental and specific results from broad disciplines like general relativity and radiation hydrodynamics. With the material included in the introduction, the publications of the thesis, which present new results with a much narrower focus, can be readily understood.

Of the publications, Paper I presents newly discovered optical data points for OJ287, detected on archival astronomical plates from the Harvard College Observatory. These data points show the 1900 outburst of OJ287 for the first time. In addition, new data points covering the 1913 outburst allowed the determination of the start of the outburst with more precision than was possible before. These outbursts were then successfully numerically modelled with an N-body simulation of the OJ287 binary and accretion disc.

In Paper II, mechanisms for the spin-up of the secondary black hole in OJ287 via interaction with the primary accretion disc and the magnetic fields in the system are discussed. Timescales for spin-up and alignment via both processes are estimated. It is found that the secondary black hole likely has a high spin.

Paper III reports a new outburst of OJ287 in March 2013. The outburst was found to be rather similar to the ones reported in 1993 and 2004. All these outbursts happened just before the main outburst season, and are called precursor outbursts. In this paper, a mechanism was proposed for the precursor outbursts, where the secondary black hole collides with a gas cloud in the primary accretion disc corona. From this, estimates of brightness and timescales for the precursor were derived, as well as a prediction of the timing of the next precursor outburst.

In Paper IV, observations from the 2004–2006 OJ287 observing program are used to investigate the existence of short periodicities in OJ287. The existence of a $\sim$50 day quasiperiodic component is confirmed. In addition, statistically significant 250 day and 3.5 day periods are found. Primary black hole accretion of a spiral density wave in the accretion disc is proposed as the source of the 50 day period, with numerical simulations supporting these results. Lorentz contracted jet re-emission is then proposed as the reason for the 3.5 day timescale.

Paper V fits optical observations and mm and cm radio observations of OJ287 with a helical jet model. The jet is found to have a spine–sheath structure, with the sheath having a much lower Lorentz gamma factor than the spine. The sheath opening angle and Lorentz factor, as well as the

helical wavelength of the jet are reported for the first time.

Tiivistelmä

Tässä väitöskirjatutkimuksessa on keskitytty tutkimaan aktiivista galaksiydintä OJ287. Väitöskirjan osana olevat tieteelliset julkaisut esittelevät OJ287-systeemistä saatuja uusia tuloksia kaksoismusta-aukkomallin kontekstissa. Väitöskirjan johdannossa käsitellään OJ287:n yleisiä ominaisuuksia ja niitä fysikaalisia perusilmiöitä, jotka näiden ominaisuuksien taustalla vaikuttavat. Johdanto selvittää myös OJ287-järjestelmän sijoittumisen aktiivisten galaksiytimien hierarkiassa.

Johdannossa käydään läpi joitakin perusfysiikan tuloksia, jotka ovat tarpeen aktiivisten galaksiydinten, mustien aukkojen binäärien, relativististen suihkujen ja kertymäkiekkojen ymmärtämiseksi. Kahden toisiaan kiertävän mustan aukon keskinäisen radan suhteellisuusteoreettiset perusteet käydään läpi yksityiskohtaisemmin. Johdannossa esitetään joitakin analyyttisiä tuloksia tällaisessa binäärissä havaittavista suhteellisuusteoreettisista ilmiöistä. Myös numeerisia menetelmiä näiden ilmiöiden tarkempaan laskemiseen esitellään. Tuloksia sovelletaan OJ287-systeemiin, ja verrataan havaintoihin.

OJ287:n mustien aukkojen ratamalli muodostaa pohjan systeemin toistuvien optisten purkausten malleille. Johdannossa esitellään yksityiskohtaisemmin kaksi fysikaalista purkausmallia, ja vertaillaan niitä. Purkausten säteilyhydrodynamiikka käydään läpi, ja myös ennusteet purkausten valokäyrille johdetaan. Johdannossa esitellään myös Julkaisussa III johdettu prekursoripurkausten malli, ja osoitetaan sen sopivan yhteen OJ287:n binäärimallin kanssa.

Johdanto esittelee myös relativististen suihkujen fysiikkaa sekä OJ287-systeemiin liittyen että aktiivisten galaksiydinten kontekstissa yleisesti. Relativististen suihkujen perusfysiikka esitellään, kuten myös malleja kierteisistä suihkuista. Julkaisujen II, IV ja V OJ287-systeemin suihkuja koskevat tulokset esitellään binäärimallin kontekstissa.

Kokonaisuutena johdanto palvelee suppeana oppaana, joka esittelee tarvittavan fysiikan ja tarpeelliset numeeriset menetelmät mustien aukkojen

binäärijärjestelmän ymmärtämiseen ja simulointiin. Tätä tarkoitusta varten johdanto yhdistää sekä perustuloksia että joitakin syvällisempiä tuloksia laajoilta fysiikan osa-alueilta kuten suhteellisuusteoriasta ja säteily-hydrodynamiikasta. Johdannon sisältämän materiaalin avulla väitöskirjan julkaisut, ja niiden esittämät tulokset, ovat hyvin ymmärrettävissä.

Väitöskirjan julkaisuista ensimmäinen esittelee uusia OJ287-systeemistä saatuja havaintopisteitä, jotka on paikallistettu Harvardin yliopiston observatorion arkiston valokuvauslevyiltä. OJ287:n vuonna 1900 tapahtunut purkaus nähdään ensimmäistä kertaa näissä havaintopisteissä. Uudet havaintopisteet mahdollistivat myös vuoden 1913 purkauksen alun ajoittamisen tarkemmin kuin aiemmin oli mahdollista. Havaitut purkaukset mallinnettiin onnistuneesti simuloimalla OJ287-järjestelmän mustien aukkojen paria ja kertymäkiekkoa.

Julkaisussa II käsitellään mekanismeja OJ287:n sekundäärisen mustan aukon spinin kasvamiseen vuorovaikutuksessa primäärin kertymäkiekon ja systeemin magneettikenttien kanssa. Julkaisussa arvioidaan maksimispinin saavuttamisen ja spinin suunnan vakiintumisen aikaskaalat kummallakin mekanismilla. Tutkimuksessa havaitaan sekundäärin spinin olevan todennäköisesti suuri.

Julkaisu III esittelee OJ287-systeemissä maaliskuussa 2013 tapahtuneen purkauksen. Purkauksen havaittiin muistuttavan vuosina 1993 ja 2004 tapahtuneita purkauksia, joita kutsutaan yhteisnimityksellä prekursoripurkaus (precursor outburst). Julkaisussa esitellään purkauksen synnylle mekanismi, jossa OJ287-systeemin sekundäärinen musta aukko osuu primäärisen mustan aukon kertymäkiekon koronassa olevaan kaasupilveen. Mekanismin avulla johdetaan arviot prekursoripurkausten kirkkaudelle ja aikaskaalalle. Julkaisussa johdetaan myös ennuste seuraavan prekursoripurkauksen ajankohdalle.

Julkaisussa IV käytetään vuosina 2004–2006 kerättyjä havaintoja OJ287-systeemistä lyhyiden jaksollisuuksien etsintään. Julkaisussa varmennetaan systeemissä esiintyvä n. 50 päivän kvasiperiodisuus. Lisäksi tilastollisesti merkittävät 250 päivän ja 3,5 päivän jaksollisuudet havaitaan. Julkaisussa esitetään malli, jossa primäärisen mustan aukon kertymäkiekossa oleva spiraalitiheysaalto aiheuttaa 50 päivän jaksollisuuden. Mallista tehty numeerinen simulaatio tukee tulosta. Systeemin relativistisen suihkun emittoima aikadilatoitunut säteily esitetään aiheuttajaksi 3,5 päivän jaksollisuusaikaskaalalle.

Julkaisussa V sovitetaan kierresuihkumalli OJ287-systeemistä tehtyihin

optisiin havaintoihin ja millimetri- sekä senttimetriaallonpituuden radiohavaintoihin. Suihkun rakenteen havaitaan olevan kaksijakoinen ja koostuvan ytimestä ja kuoresta. Suihkun kuorella on merkittävästi pienempi Lorentzin gamma-tekijä kuin suihkun ytimellä. Kuoren avautumiskulma ja Lorentz-tekijä sekä suihkun kierteen aallonpituus raportoidaan julkaisussa ensimmäistä kertaa.

List of papers

This thesis consists of a review of the subject and the following original research articles:

I **The historical 1900 and 1913 outbursts of the binary blazar candidate OJ287**,
R. Hudec, M Bašta, **P. Pihajoki**, and M. Valtonen, A&A **559**, A20 (2013).

II **Outbursts from the secondary component in OJ 287 and the secondary spin-up**,
P. Pihajoki, Tidal Disruption Events and AGN Outbursts, EPJ Web of Conferences, eds. R. Saxton & S. Komossa **vol. 39**, 6006 (2012).

III **Precursor Flares in OJ287**,
P. Pihajoki, M. Valtonen, S. Zola, A. Liakos, M. Drozdz, M. Winiarski, W. Ogloza, D. Koziel-Wierzbowska, J. Provencal, K. Nilsson, A. Berdyugin, E. Lindfors, R. Reinthal, A. Sillanpää, L. Takalo, M. M. M. Santangelo, H. Salo, S. Chandra, S. Ganesh, K. S. Baliyan, S. A. Coggins-Hill, and A. Gopakumar, ApJ **764**, 5 (2013) [arXiv:1212.5206].

IV **Short time-scale periodicity in OJ 287**,
P. Pihajoki, M. Valtonen, and S. Ciprini, MNRAS **434**, 3122 (2013) [arXiv:1307.1113].

V **A helical jet model for OJ287**,
M. Valtonen, and **P. Pihajoki**, A&A **557**, A28 (2013) [arXiv:1307.1364].

List of Abbreviations

AGN	Active galactic nucleus/nuclei
AVA	Auxiliary Velocity Algorithm
AVP	Auxiliary Velocity and Position Algorithm
FRI	Fanaroff–Riley type I radio galaxy
FRII	Fanaroff–Riley type II radio galaxy
FSRQ	Flat spectrum radio quasar
GR	General relativity
GRB	Gamma ray burst
I98	Optical outburst model of Ivanov et al. (1998)
IC	Inverse Compton
IR	Infrared
IRAS	Infrared Astronomical Satellite Catalog
LBL	Low peaking BL Lac
LV96	Binary black hole model of Lehto & Valtonen (1996)
MHD	Magnetohydrodynamics
MRI	Magnetorotational instability
NRAO	National Radio Astronomy Observatory
PDE	Partial differential equation
PN	Post–Newtonian
PPN	Parametrized Post–Newtonian
Q	(Post–Newtonian) Quadrupole–monopole interaction
QSO	Quasi–stellar object
SDSS	Sloan Digital Sky Survey
SED	Spectral energy distribution
SMBB	Supermassive black hole binary
SMBH	Supermassive black hole
SO	(Post–Newtonian) Spin–orbit interaction
SR	Special relativity
SS	(Post–Newtonian) Spin–spin interaction
SSC	Synchrotron Self–Compton
UV	Ultraviolet
VLA	Very Large Array
VLBI	Very Long Baseline Interferometry

Chapter 1

Introduction

The visible Universe as we know it can be characterized as consisting of voids interspersed with filaments and clusters of galaxies, forming a foam-like structure. The galaxies, in turn, are great accumulations of stars, gas and dust embedded in dark matter haloes, and have supermassive black holes (SMBH) in their centers in nearly all cases. A supermassive black hole can be the result of two different scenarios. In one case, the SMBH was initially a stellar mass black hole, which is the remnant of a supernova explosion of a massive star, and grew afterwards by accreting matter and merging with other black holes. It is also possible that it may have collapsed directly from the matter within the nucleus of a proto-galaxy (Begelman et al. 2006). If all types of black holes are considered together, they range in mass from several solar masses to tens of billions of solar masses. Within the framework of general relativity theory (GR), it can be said that all this mass is contained within in a single point, the singularity, which is hidden inside a spheroidal volume. The outer limit of this volume is often called the event horizon, and at its location the gravitation acceleration towards the black hole becomes so great that even light cannot escape from it.

We observe that the centers of some of these galaxies exhibit an unusual brightness across all or some of the frequency bands of electromagnetic radiation, from radio to gamma rays. This radiation often varies on very short timescales indicating the compactness of the source, by causality. In addition, powerful two-sided outflows called jets, extending all the way to kiloparsec scales are sometimes observed. These characteristics are what defines an active galactic nucleus (AGN). Today, we understand that the phenomena observed in AGNs are most likely powered by accretion of matter into the central SMBH of the galaxy (for a review, see Ferrarese & Ford 2005).

The different AGN display a very wide variety of physical characteristics in spectral energy densities, polarization, variability timescales, estimated absolute brightness and the type of host galaxy. Thus, many different categories of AGNs have been defined to satisfactorily include each object. A significant step forward in understanding these objects came with the realization that many of the differences we observe can be explained by variations in the observation angle (Antonucci 1993; Urry & Padovani 1995).

The object studied in this thesis, OJ287, is commonly categorized as a *blazar*. This means that we are looking at this AGN nearly along its jet, with evidence that the angle between the jet and line of observation is $\angle 30$ at most (Padovani & Urry 1990). For OJ287, this angle is likely around $\angle 2$ (Savolainen et al. 2010; Agudo et al. 2012), and the observed radiation is dominated by the jet, which causes OJ287 to appear very bright, violently variable and displaying characteristics of synchrotron emission. However, among all blazars and indeed all AGN, OJ287 is unique in the respect that it is rather firmly established to produce very nearly periodical optical outbursts every 12 years. Historical observations of the system, beginning in late 19th century, confirm the continuing existence of these outbursts, and in 1988 a binary black hole model was proposed based on this observed phenomenon (Sillanpää et al. 1988). Since 1996, the binary black hole model revised in Lehto & Valtonen (1996) has successfully predicted one minor and four major optical outbursts (Valtonen et al. 2011a). There have been no major optical outbursts that the model has not predicted, and more importantly, no outburst in the predicted cycle has failed to appear entirely. The success of the model makes OJ287 a very likely candidate for a SMBH binary (SMBB).

In this thesis, we present a review of OJ287 in the context of a supermassive binary black hole model, and peer-reviewed publications of new discoveries within this context. In Chapter 2, we briefly review the physical characteristics of OJ287 and discuss the historical context of the object, the progress in optical periodicity searches and the resulting binary black hole model. Chapter 3 reviews the general relativistic basics required for understanding binary black holes, presents the problem of calculating the orbit of a binary black hole, and some solutions to this problem. The nature of the optical outbursts and possible mechanism for them are discussed in Chapter 4. In Chapter 5, the characteristics of the relativistic jet of OJ287 are reviewed, along with recent results. A summary of the publications

included in this thesis is presented in Chapter 6. Finally, conclusions and possible future work are discussed in Chapter 7.

Chapter 2

Overview of the OJ287 system

2.1 Historical perspective

The quasi-stellar object (QSO) or quasar OJ287 is visible in the optical wavelengths as a variable point source with an approximate magnitude of 15.4 in the V-band (Véron-Cetty & Véron 2010). Its scientific history, however, starts with a detection as a radio source in 1967 (Dickel et al. 1967). After this, like many astronomical objects, OJ287 has accrued many identifiers along the years, such as IRAS 08519+2017 in the Infrared Astronomical Satellite catalog, NRAO 0852+20 in the National Radio Astronomy Observatory survey catalog or SDSS J085448.87+200630.7 in the Sloan Digital Sky Survey catalog. However, the designation it's most commonly known by, OJ287, is from the Ohio Sky Survey catalog compiled between 1965 and 1971 at the Ohio State University Radio Observatory with the famous Big Ear radio telescope[1] (Kraus et al. 1968). Soon afterwards, the optical counterpart of OJ287 was detected, and it was first classified as a stellar object (Thompson et al. 1968). Already at that time, it aroused interest due to its peculiar spectral characteristics (Jauncey et al. 1970).

In short fashion, after the initial mentions, new discoveries on characteristics of OJ287 started pooling. Eventually, it was reclassified as an AGN, and then a blazar, an AGN with the jet aligned very close to the direction of the Earth, with recent observations suggesting an angle of $\angle 2$

[1]The Big Ear was also the radio telescope that picked up the legendary "Wow!" signal, at a frequency very near that of the neutral hydrogen line at 1420.4 MHz. This detection has been at times touted as a signal from an extraterrestrial intelligence (Gray 1994).

between jet axis and line of observation (Savolainen et al. 2010; Agudo et al. 2012). Among blazars, it was further categorized as a BL Lac object, based on strong optical polarization and rapid, large-amplitude brightness variations, and a featureless spectrum with very weak emission lines (Stein et al. 1976). This categorization goes even further, with the finest subcategory now being Low Peaking BL Lac (LBL), which indicates that the OJ287 synchrotron peak resides at sub-mm to IR frequencies (Padovani & Giommi 1995).

Already by the early 1970's, there were hints of both intraday and long term variability of the OJ287 system in the optical regime (Craine & Warner 1973; Frohlich et al. 1974). By 1985, the study of short term optical variability in OJ287 had progressed to the point that more detailed dynamical models involving hotspots in an accretion disc were proposed (Carrasco et al. 1985). In 1986 evidence was presented for an optical period of ~ 4 years (Li et al. 1986), but it was not until 1988, when the collation of long term optical data led to the discovery of the optical 12 year period and the proposition of a binary black hole in the OJ287 system (Sillanpää et al. 1988).

The discovery of the 12 year period was in part possible due to the fact that OJ287 is situated very near the ecliptic, and has been often unintentionally photographed in the past. Searches of photographic plate archives for images containing OJ287 have yielded new data points that are especially important for the analysis of the otherwise poorly documented outbursts in the early 20th century. Paper I presents the results of one of such searches. The current full historical light curve is shown in Figure 2.1.

2.2 Basic observable characteristics

In J2000.0 coordinates, OJ287 has a right ascension of $8^{\mathrm{h}}54^{\mathrm{m}}48.875^{\mathrm{s}}$ and a declination of $20°6'30.64''$ (Lanyi et al. 2010), situating it near the ecliptic, in the constellation of Cancer. The neighbourhood of OJ287, in optical wavelengths, is shown in Figure 2.2.

BL Lac objects as a group are characterized by several observable characteristics: rapid brightness variations in radio, infrared and optical wavelengths, nonthermal continuum with most of the luminosity in infrared, featureless optical spectrum, and strong and variable polarization in radio and optical wavelengths (Strittmatter et al. 1972; Stein et al. 1976). De-

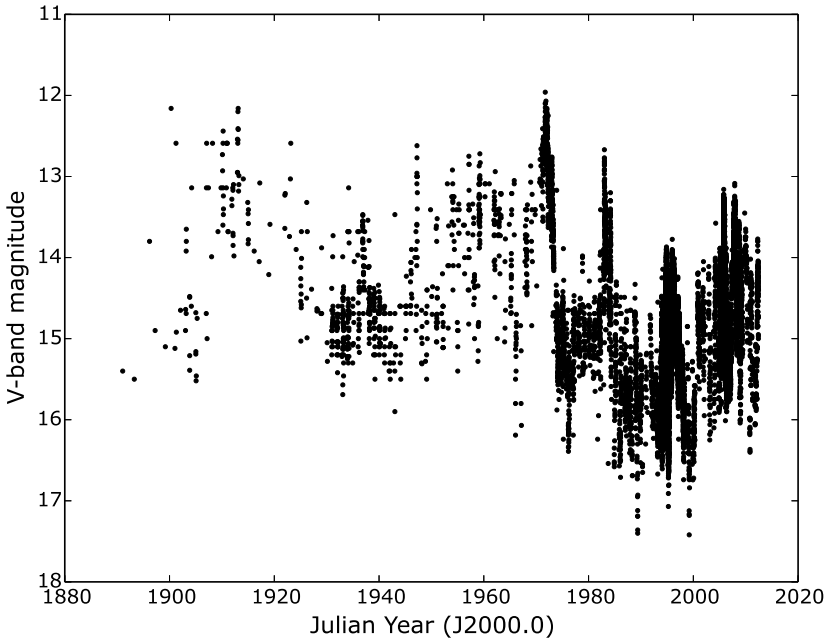

Figure 2.1: The historical optical light curve of OJ287, with data points derived from low quality plates and upper limit estimates omitted. All magnitudes have been converted to the V band, using relations $V = R+0.4$ (Valtonen et al. 2008b) and $V = B - 0.45$ (Takalo et al. 1994).

spite the usually featureless optical spectrum, a very tentative detection of an [OIII] line was made in Miller et al. (1978), suggesting $z = 0.306$. Later, a significant detection of a H_α line and weaker H_β and [OIII] lines was made in Sitko & Junkkarinen (1985), confirming the redshift and the definite extragalactic origin of OJ287. The latter detection was made during a period of low activity, so that the usually overwhelming featureless jet synchrotron emission was at a minimum.

The redshift of OJ287, $z = 0.306$ (Sitko & Junkkarinen 1985; Snellen et al. 2002), is average for a BL Lac object (Shaw et al. 2013). The SIMBAD database (Wenger et al. 2000) contains 1737 BL Lac objects, from which 1231 have redshift data, ranging from $z \sim 0$ to $z = 5.995$. However, 85%

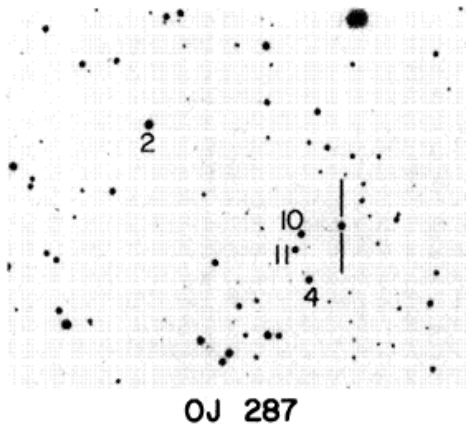

Figure 2.2: Optical finding chart of OJ287 with numbered field comparison stars from Smith et al. (1985). The image is a cropped feature from a Palomar Observatory Sky Survey photographic plate, with a width of approximately 15 arcminutes. OJ287 is located between the vertical bars.

of all BL Lacs have $z \leq 1.0$, and at $z \sim 0.3$, the cumulative distribution function of BL Lac redshifts is quite linear, which confirms that the redshift of OJ287 is not exceptional. The spectral energy distribution (SED) of OJ287 (Fig. 2.3) is double humped, as is typical for BL Lacs. The lower frequency bump is the synchrotron peak from jet emission, and the higher frequency bump is its inverse Compton counterpart. From Figure 2.3, it is evident that the spectrum of OJ287 is different at outburst times than during quiescence. The total apparent luminosity of OJ287 from radio to UV has been estimated as $2 \times 10^{46}\,\mathrm{erg\,s^{-1}}$ (Worrall et al. 1982). When radio and inverse Compton contributions are added, the total luminosity may be as high as $3 \times 10^{47}\,\mathrm{erg\,s^{-1}} \sim 7.8 \times 10^{13}\ L_\odot$ (Worrall et al. 1982), where $L_\odot = 3846 \times 10^{33}\,\mathrm{erg\,s^{-1}}$ is the luminosity of the Sun.

The host galaxy of OJ287 has proven to be hard to resolve adequately, and the estimates for its apparent magnitude in the R-band show considerable scatter from approximately 18.41 to 19.32 (Heidt et al. 1999; Villforth et al. 2010). Host galaxy size and morphology have proved as elusive to pin down, and no consensus is available (Villforth et al. 2010). In comparison, the apparent magnitude of OJ287 itself is around 15 on average in the R-band, explaining the difficulty in resolving the host galaxy. In radio

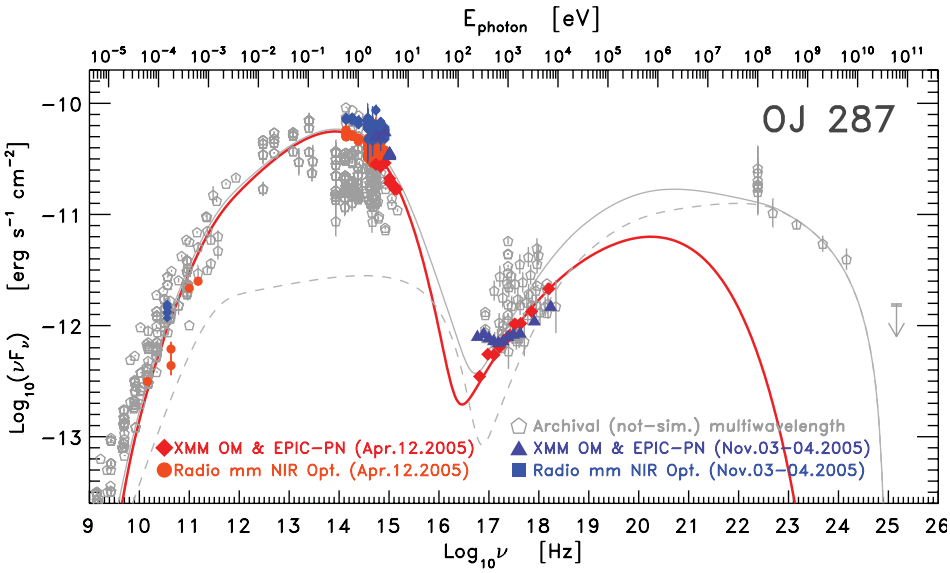

Figure 2.3: The SED of OJ287 during the 2005 November outburst (blue symbols) and before the outburst in 2005 April (red symbols). The red line is one component synchrotron self–Compton (SSC) fit to the data. Gray symbols and lines are archival data. Figure from Valtonen et al. (2012).

wavelengths, however, some details of the OJ287 system can be resolved. The prominent features are the bright and stationary radio core, and the moving 'clumps' of enhanced radio emission. These can be identified as originating from the relativistic jet in the OJ287 system, discussed in more detail in Chapter 5. Figure 2.4 shows the appearance of OJ287 at mm-scale radio wavelengths.

2.3 Development of the precessing binary black hole model

Since apparently nearly all massive galaxies host central SMBHs (Ferrarese & Ford 2005), and galaxies are known to grow via hierarchical merging in the ΛCDM universe (Benson 2010), it is to be expected that galaxies hosting multiple SMBHs exist. After a galaxy merger, SMBHs from the component

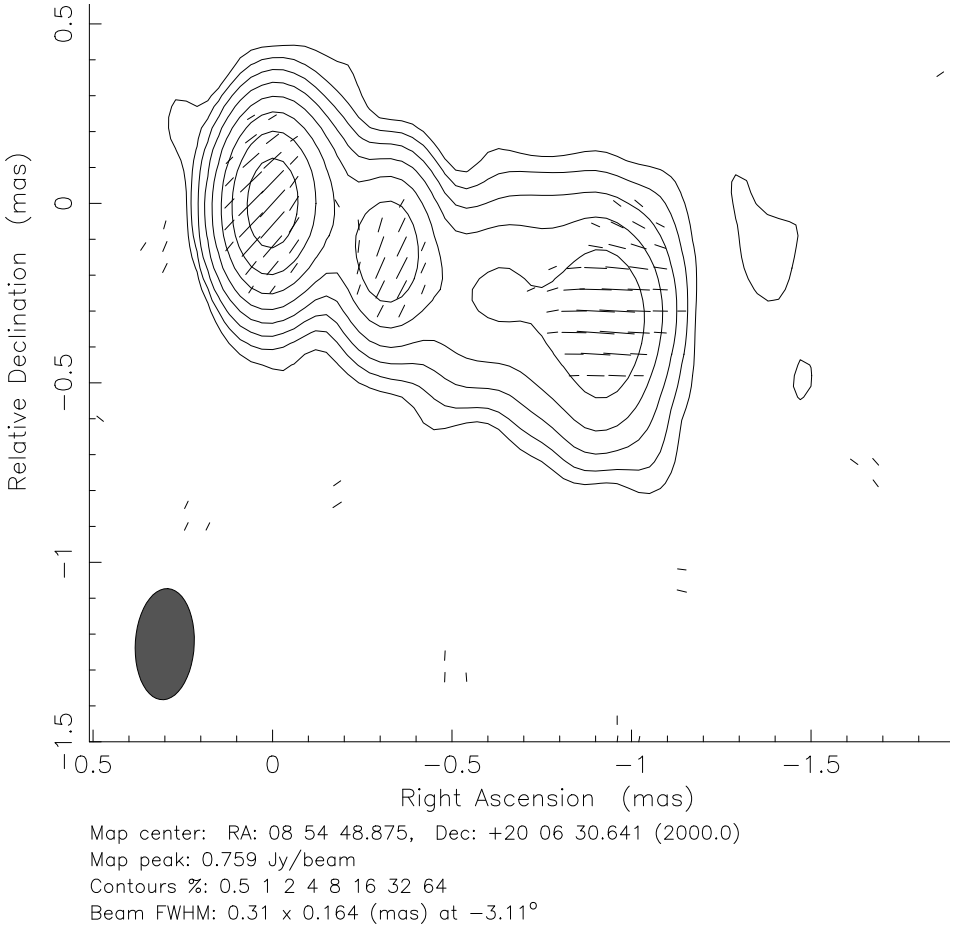

Figure 2.4: VLBA image of OJ287 at 43 GHz, with contour lines indicating total intensity and line segments indicating the direction of polarization electric vector. The core is seen on the left, with two knots to the right of it. Figure from Jorstad et al. (2005).

galaxies experience dynamical friction from interaction with the field stars, the dark matter halo and the gas contained in the merging galaxies (Chandrasekhar 1943; Volonteri et al. 2003; Mayer et al. 2007). These processes tend to cause the black holes to sink towards the center of the new galaxy, and form a loose binary. The average separation of this binary then grad-

ually diminishes, because of the effects mentioned above, but also due to close interactions with the fields stars. These close many body interactions tend to favor the ejection of the stars the hardening of the SMBH binary (Sigurdsson & Hernquist 1993; Makino & Ebisuzaki 1994; Iwasawa et al. 2011), Thus it seems that close binaries of SMBHs should exist. In actuality, it turns out that if the merger is not gas rich, it is not straightforward to see how field star interactions within the merging galaxy would reduce the orbital distance of the two SMBHs to a sub-parsec distance. Through ejections, the binary SMBHs deplete their neighbourhood of stars on close orbits, and the evolution stalls at a separation of around one parsec Khan et al. (2013). As such, this problem is sometimes called *the final parsec problem* (see e.g. Milosavljević & Merritt 2003). It is likely not a real physical effect, but an artifact of our incomplete understanding, and has been mostly resolved at least for high SMBH binary mass ratios (Iwasawa et al. 2011), and for galaxies that exhibit axisymmetry (Khan et al. 2013). In mergers that are moderately gas rich, this problem does not occur, since the dynamical friction from the gas interaction does not cease functioning at close binary separations (Mayer et al. 2007). In light of this evidence, the existence of close SMBH binaries seems very likely.

The theoretical case for the existence of close SMBH binaries and the contrasting lack of observational proof has then been grounds for much interest in OJ287 as a possible close SMBH binary after the seminal paper of Sillanpää et al. (1988). The initial model was based on a planar system of a black hole binary and circumbinary accretion disk wherein the tidal action of the secondary caused the accretion rate of the primary to fluctuate. These fluctuations in turn were seen as the cause of the observed optical outbursts. The model predicted a new outburst in 1994, which subsequently happened quite near the expected time in the fall of that year (Sillanpää et al. 1996a). This marked the *first time* a predicted event in an AGN was detected.

As more optical data was gathered, it seemed that this model was not sufficient. One reason was that the optical outbursts had not happened at exact periodic intervals—a state of affairs noted already in Sillanpää et al. (1988). A second new observation was that the optical flares were actually double peaked (Sillanpää et al. 1996b). This led to the development of a *precessing* binary black hole model in Lehto & Valtonen (1996). In this model, hereafter referred to as the LV96 model, the orbit of the secondary is inclined, and precesses, as is expected due to the relativistic

nature of the system. In the model, two outbursts per period occur when the secondary black hole impacts the accretion disk of the primary, causing shocked plasma to be blown off the disk. This radiatively dominated matter expands and cools, until it becomes optically thin and produces a prominent bremsstrahlung outburst. As the secondary crosses the disk near pericenter, these flares come in pairs; one during pericenter approach, the second after leaving pericenter. The interval between these flares is determined by the precession angle of the orbit. In addition to the bremsstrahlung flares, the model leads to similar tidally induced outbursts in the primary as the original model in Sillanpää et al. (1988). All of these features can be observed in the optical light curve of OJ287, giving the model great credence (Sillanpää et al. 1996a,b; Lehto & Valtonen 1996; Valtonen et al. 2009, 2012).

As emphasized in the introduction, the most significant aspect of the model is that OJ287 has never failed produce an expected outburst, barring the possibility of such an event occurring during a gap in the historical light curve. OJ287 does exhibit some additional variability and slow drifts in baseline brightness not accounted by the model, but this optical variability, likely originating from the relativistic jet, is common to all BL Lacs. More interesting are the short minor optical outbursts occurring before a major outburst. These precursor outbursts have been modelled in Paper III, and are discussed in detail in Chapter 4.

After the initial LV96 paper, the precessing binary black hole model has subsequently been tested and revised several times as more data have become available (Valtonen & Lehto 1997; Pietilä 1998; Valtonen et al. 2006b,a; Valtonen 2007; Valtonen et al. 2008a,b, 2009). With the most recent additions to the model (Valtonen et al. 2010b,a, 2011b), it now includes, as parameters of the model, the masses m_1 & m_2 of the black holes, the nondimensional magnitude of spin χ of the primary black hole, the eccentricity e of the orbit, the initial precession angle ϕ_0 and the rate of precession per orbit $\Delta\phi$, the dimensionless time delay parameter t_d, which scales the total delay between the disk crossings and the outbursts expected from the astrophysical model, and the relativistic quadrupole moment parameter q. The most current values of these are listed in Table 2.1.

Table 2.1: Current best fit values for the parameters of the binary black hole model (Valtonen et al. 2010a, 2011b).

Parameter	Value
$\Delta\phi$	$(39.1 \pm 0.1)^\circ$
m_1	$(1.84 \pm 0.01) \times 10^{10}\ M_\odot$
m_2	$(1.40 \pm 0.03) \times 10^{8}\ M_\odot$
χ	0.28 ± 0.03
ϕ_0	$(56.3 \pm 1.0)^\circ$
e	0.658 ± 0.001
q	1.0 ± 0.9
t_d	0.74 ± 0.04

2.4 Other proposed models for OJ287

Since the realization of the optical periodicity of OJ287, many models have been proposed to explain this observation. These are based on a plethora of different physical explanations, but to be considered as plausible as the LV96 model, all would need to explain the following observed phenomena:

(i) non-exact ~ 12 year periodicity of the twin flares (already noted in Sillanpää et al. 1988)

(ii) varying interval between the twin flares (Lehto & Valtonen 1996)

(iii) low polarization and bremsstrahlung excess observed in the twin flares (Valtonen et al. 2008b, 2009, 2012)

(iv) tidal flares (Valtonen et al. 2009)

(v) 60 year modulation of the flare brightnesses & jet wobble (Valtonen et al. 2006a; Valtonen & Wiik 2012)

The LV96 model is very successful in this regard, but for the sake of completeness we will list some other models, choosing ones with predictive qualities and leaving out purely qualitative ones. In each case, we will

point out where the model is lacking with respect to the required explanations of the phenomena above. A larger exposition of models can be found in the following references: Sillanpää et al. (1996b); Valtaoja et al. (2000); Valtonen et al. (2006a) and Valtonen & Sillanpää (2011).

2.4.1 Jet models

One idea is that the 12 year variability is a result of variation of the jet viewing angle. This was proposed in Katz (1997). In this model, the primary accretion disk precesses with nutation because of the gravitational influence of the secondary and changes the jet direction, and thus the viewing angle. The viewing angle changes the Doppler boosting factor

$$D = [\Gamma(1 - \beta \cos\theta)]^{-1}, \tag{2.1}$$

where $\Gamma = 1/\sqrt{1-\beta^2}$, $\beta = v/c$, θ is the viewing angle, v velocity and c the speed of light. The observed flux is proportional to $D^{a-\alpha}$, where $a = 2$ for a spatially continuous emitting feature, $a = 3$ for a discrete emitting blob, and α is the spectral index defined by $S_\nu \propto \nu^\alpha$, where S_ν is the observed spectral flux density at frequency ν. Thus, the proposition of the jet models is that the change in viewing angle results in the observed flares.

The problem with this model is that the radiation from from a jet is expected to come from a synchrotron process, which implies high polarization and radio counterparts, which have not been observed for all flares (Valtaoja et al. 2000). The change in Doppler factor also implies changing variability timescales since the ratio between observed and local timescales $\delta t/\delta t' = D^{-1}$, but again, this phenomenon has not been observed (Valtaoja et al. 2000).

A related idea is that both black holes in the binary have their own jets, and the changing viewing angles are due to binary orbital motion (Villata et al. 1998). This model suffers from the same problems as the previous one, and also results in timescales that are too long for the brief duration of the observed optical flares (Valtonen et al. 2006a).

2.4.2 Tidal models

The outbursts have also been proposed to originate from a tidally enhanced accretion rate of the primary, as in the original binary model of Sillanpää et al. (1988) or in Sundelius et al. (1997). These models have trouble

explaining the double peaked nature of the outbursts and produce outburst timescales that are too long (Valtaoja et al. 2000; Valtonen et al. 2006a).

2.4.3 Non-precessing model

In Valtaoja et al. (2000), a non-precessing binary black hole model was proposed. In this model, the black hole masses m_1 and m_2 are smaller and the binary semimajor axis a is larger in terms of the black hole Schwarzschild radii, since $a/r_{\rm Sch} \propto (m_1 + m_2)^{-2/3}$ for a constant binary period. Since the precession angle $\Delta\theta \propto (a/r_{\rm Sch})^{-1}$, this leads to a non-precessing model. The first of the twin outbursts in the model is a thermal flare caused by the secondary impacting the primary accretion disk, similarly to Lehto & Valtonen (1996). The second peak is caused by increased accretion and jet brightening caused by the tidal effects of the secondary pericenter passage. The second impact flare is proposed to happen near the secondary apocenter, which would lead to very dim impact flare lost under the inherent flux variations of the system.

A problem with the model is that it does not give a quantitative estimate for the delay between the first and the second outbursts, but merely claims that there is a variable delay from one orbit to the next. In this model there should not be a measurable second thermal flare, which is contrary to later observations (Valtonen & Sillanpää 2011). Another problem is that the model predicted the outburst that occurred in 2005 November to begin no earlier than 2006 September (Valtonen et al. 2006b).

2.4.4 Cavity flares

A model featuring fast accretion events in a cavity within a circumbinary accretion disk as the cause of the optical flares in OJ287 was recently proposed in Tanaka (2013). In this model, Lindblad resonance clears a radial range of $\sim 2a$ around the binary, where a is the binary semi-major axis, forming a low-density cavity. As the high-energy inner region of the accretion disk is now omitted, this results in a steep spectral energy density (SED) cutoff at a range from ultraviolet (UV) to infrared (IR), depending on the system parameters. Once per period, filaments of plasma can leak into the cavity on nearly radial orbits towards one or both of the black holes leading eventually to shock heating and circularization. This shock heated gas then radiates, causing the optical flares.

As demonstrated in Tanaka (2013), this model can produce twin peaked thermal outbursts with the required 12 year periodicity, but does not predict the inter-peak delay, which is taken as a fixed parameter. Furthermore, in the model there is no explanation for the tidal flares or the observed 60 year modulation of flare brightnesses.

Chapter 3

Binary black hole orbits

3.1 Relativistic orbits

When investigating the time dependent features of close SMBH binaries, accurate calculation of the binary orbit is naturally of paramount importance. This calculation is not straightforward, as the relativistic effects for close binaries can be large compared to Newtonian gravity. These effects affect the orientation and shape of the orbit, precessing both the orbit and the orbital plane, and decreasing the semi-major axis, as orbital energy is lost via gravitational radiation. The twofold problem statement is then as follows: First, what are the expected effects in the context of General Relativity (henceforth GR), expressed analytically. Second, how can correct relativistic orbits be numerically calculated so that the result is accurate to some specified order of c^{-k}, where c is speed of light.

3.2 Analytic estimates

3.2.1 Preliminary assumptions

A brief review of the very basics of general relativity follows. The contents follow a synthesis of such texts as Carroll (2004), Landau & Lifshitz (1975), Wald (1984), Schutz (1985) and others, as well as my own input. Here, we use the $-+++$ sign convention for the metric tensor g_{ab}, so the metric signature is $(1, 3)$. We set $c = 1$ and use abstract index notation throughout. For an in-depth discussion of this notation see e.g. Penrose & Rindler (1987) or Wald (1984). Here we present only a motivating example: If K is a field, V is a vector space over the field, V^* its dual, and $g : V \times V \times V^* \to K$ is a multilinear map (*tensor*), then we write $g_{ab}{}^c$, with a, b and c as

abstract placeholders of the 'slots' of g where arguments can be placed. No basis is set. Then ${g_{ab}}^{c} \in V^* \otimes V^* \otimes V$, where $\otimes$ is the tensor product. The notation is formally basis independent, but enables contractions and various tensor products to be written conveniently in a manner resembling Einstein's notation. For example, a contraction can be written as $h_a = {g_{ab}}^{b}$ and a tensor product as ${m_a}^{c} n_b = {k_a}^{c}{}_{b}$. We use the convention that all equations written with Latin indexes are understood to be tensor equations without any set basis, and Greek indexes correspond to equations with some chosen coordinate basis. Equations of the former type are tensor equations valid in any coordinates, while the latter relate tensor components in some specific coordinates. These equations are not necessarily valid in other coordinate systems.

The physics of GR is the physics of curved spacetimes. Our physical spacetime is the *pseudo–Riemannian manifold* (M, g), where M is a smooth 4-dimensional manifold and $g : T_x(M) \times T_x(M) \to \mathbb{R}$ is an inner product (i.e. pseudo–metric) at point $x \in M$ such that if $X, Y : M \to T(M)$ are vector fields on M, the map $x \mapsto g(X(x), Y(x))$ is smooth. $T_x(M)$ is the tangent space at point x, and $T(M) = \cup_{x \in M} T_x(M)$ is the tangent bundle. In the literature, the metric is often written with the help of an infinitesimal squared arc length $\mathrm{d}s$ and infinitesimal coordinate displacements $\mathrm{d}x^\mu$ in some local coordinates x^μ as

$$\mathrm{d}s^2 = g_{\mu\nu} \mathrm{d}x^\mu \mathrm{d}x^\nu. \tag{3.1}$$

Equation (3.1) is a notational shorthand. The right-hand side can be formally understood as an expansion of g_{ab} in terms of a basis $\{\mathrm{d}x^\mu \otimes \mathrm{d}x^\nu\}$ of two-forms $\mathrm{d}x^a \otimes \mathrm{d}x^b \in V^* \otimes V^*$.

The spacetime differs from Euclidean $\mathbb{R}^4$ already by the fact that the metric is a pseudo–metric; that is for some nonzero $X, Y \in T_x(M)$ the inner product $g(X, Y)$ can be zero or even negative. In addition, the space can be curved. This characteristic can be defined as the failure of a vector parallel transported in a closed loop to remain unchanged, or as the failure of derivative operators to commute. In quantitative terms, if a vector $Z \in T_x(M)$ is parallel transported along a loop defined by vectors $X, Y \in T_x(M)$ and lengths δx and δy, the deviation $\delta Z \in T_x(M)$ is given by a linear transformation R^a_{bcd} such that

$$\delta Z^a = \delta x \delta y X^c Y^d {R^a}_{bcd} Z^b, \tag{3.2}$$

where $R^a{}_{bcd}$ is the *Riemann tensor* (Carroll 2004), which completely characterizes the curvature of the spacetime at a point. It can be written in terms of a connection $\Gamma^a{}_{bc}$. In general, the connection can be specified separately, but in GR it is derived from the metric, and is known as the Levi–Civita connection (or Christoffel symbol), given by

$$\Gamma^a_{bc} = \frac{1}{2} g^{ad} \left(\partial_b g_{cd} + \partial_c g_{db} - \partial_d g_{bc} \right). \tag{3.3}$$

With the Levi–Civita connection, the Riemann tensor can be written as

$$R^a{}_{bcd} = \partial_c \Gamma^a_{db} - \partial_d \Gamma^a_{cb} + \Gamma^a_{ce} \Gamma^e_{db} - \Gamma^a_{de} \Gamma^e_{cb}. \tag{3.4}$$

The Riemann tensor, and its lower index form $R_{abcd} = g_{ae} R^e{}_{bcd}$, have various convenient symmetries, particularly

$$R^a{}_{bcd} = -R^a{}_{bdc} \tag{3.5}$$
$$R_{abcd} = -R_{bacd} \tag{3.6}$$
$$R_{abcd} = R_{cdab} \tag{3.7}$$
$$R_{a[bcd]} = 0 \tag{3.8}$$
$$\nabla_{[e} R_{ab]cd} = 0, \tag{3.9}$$

where ∇_e is the covariant derivative, and the angle brackets denote the antisymmetrization operation. For an arbitrary tensor $T^{i_1 \cdots i_l}{}_{i_{l+1} \cdots i_n}$ these are defined as

$$\begin{aligned} \nabla_a T^{i_1 \cdots i_l}{}_{i_{l+1} \cdots i_n} =& \partial_a T^{i_1 \cdots i_l}{}_{i_{l+1} \cdots i_n} \\ &+ \Gamma^{i_1}_{ab} T^{b i_2 \cdots i_l}{}_{i_{l+1} \cdots i_n} + \Gamma^{i_2}_{ab} T^{i_1 b i_2 \cdots i_l}{}_{i_{l+1} \cdots i_n} + \cdots \\ &- \Gamma^b_{a i_{l+1}} T^{i_1 \cdots i_l}{}_{b i_{l+2} \cdots i_n} - \Gamma^b_{a i_{l+2}} T^{i_1 \cdots i_l}{}_{i_{l+1} b i_{l+3} \cdots i_n} - \cdots \end{aligned} \tag{3.10}$$

and

$$T^{[i_1 \cdots i_l}{}_{i_{l+1} \cdots i_n]} = \frac{1}{n!} \sum_{\pi \in S_n} \operatorname{sgn}(\pi) T^{\pi(i_1, \ldots, i_l)}{}_{\pi(i_{l+1}, \ldots, i_n)}, \tag{3.11}$$

where S_n is the group of all permutations of the n indexes (the symmetric group of order $n!$), $\operatorname{sgn} : S_n \to \{1, -1\}$ is the sign of the permutation,

$+1$ for even and -1 for odd permutations, and we understand $\pi(i_1, \ldots, i_l)$ to stand for the first l symbols of the entire permuted symbol progression $\pi(i_1, \ldots, i_n)$, and likewise $\pi(i_{l+1}, \ldots, l_n)$ for the last $n - l$ symbols.

From the Riemann tensor, we get further objects via contractions, namely the Ricci tensor

$$R_{ab} = R^{e}{}_{aeb} \tag{3.12}$$

and the Ricci scalar

$$R = g^{ab} R_{ab}. \tag{3.13}$$

From these, we can form the *Einstein tensor*, or trace-reversed Ricci tensor

$$G_{ab} = R_{ab} - \frac{1}{2} R g_{ab}. \tag{3.14}$$

For the actual physics in a GR context we can form the Hilbert action

$$S = \int_M \sqrt{-g} R \mathrm{d}^4 x + S_M, \tag{3.15}$$

where S_M is the contribution from matter in the non-vacuum case. When equation (3.15) is varied with respect to the metric, the result is *Einstein's field equations*

$$G_{ab} = 8\pi G T_{ab}\,, \tag{3.16}$$

where G is the Newtonian gravitational constant, and the stress–energy tensor T_{ab} is defined by

$$T_{ab} = -\frac{1}{\sqrt{-g}} \frac{\delta S_M}{\delta g^{ab}}. \tag{3.17}$$

In principle, we can then solve the non-linear coupled equations (3.16), and obtain the metric. This turns out to be difficult in general. For the case of black holes, see e.g. the comprehensive work in Chandrasekhar (1983). Solutions are typically only possible for specific cases where symmetries can be exploited. Of these, the ones related to this work are described in the following paragraphs.

Vacuum solution. If $T_{ab} = 0$ everywhere (i.e. a vacuum), then $g_{ab} = \eta_{ab}$ is a solution of (3.16). η_{ab} is the *Minkowski metric* of a flat spacetime, with a constant diagonal of $(-1, 1, 1, 1)$. Thus, special relativity describes the physics of this system.

Schwarzschild solution. Looking at spacetimes that have a maximally symmetric[1] 2-dimensional submanifold leads to a unique solution of the field equations (3.16) called the *Schwarzschild metric*:

$$\mathrm{d}s^2 = -\left(1 - \frac{2GM}{r}\right)\mathrm{d}t^2 + \left(1 - \frac{2GM}{r}\right)^{-1}\mathrm{d}r^2 + r^2\left(\sin^2\theta\mathrm{d}\phi^2 + \mathrm{d}\theta^2\right), \tag{3.18}$$

where M is the mass of the spherical mass distribution inside r (Carroll 2004). The coordinates (r, θ, ϕ) correspond to the usual spherical coordinates. This reduces to the Minkowski metric if $M \to 0$ or if $r \to \infty$. The solution is also static (nothing changes with time), even if the enclosed mass distribution is not. The significance of the radial distance $r = r_{\mathrm{Sch}} = 2GM$, the *Schwarzschild radius* or the radius of the *event horizon*, is apparent.

Kerr–Newman solution. Forgoing spherical symmetry for axial symmetry leads to the Kerr–Newman metric, given in Boyer–Lindquist coordinates as

$$\begin{aligned}\mathrm{d}s^2 = -\mathrm{d}t^2 + \frac{\rho^2}{\Delta}\mathrm{d}r^2 + \rho^2\mathrm{d}\theta^2 + (r^2 + a^2)\sin^2\theta\mathrm{d}\phi^2 \\ + \frac{2GMr}{\rho^2}\left(a\sin^2\theta\mathrm{d}\phi - \mathrm{d}t\right)^2,\end{aligned} \tag{3.19}$$

where $\Delta = r^2 + a^2 - 2GMr + Q^2/G$, $\rho^2 = r^2 + a^2\cos^2\theta$, Q is the total charge (electric and magnetic) of the black hole and $a = J/M$ is the normalized spin angular momentum of the hole ($0 \le a \le M$) (Carroll 2004). Later in this work we will also use the non-dimensional spin parameter $\chi = a/M = J/M^2$, for which $0 \le \chi \le 1$. The metric is stationary; the geometry is not changing, but there is rotation.

When the metric is known, the infinitesimal arc lengths in (3.1) can be

[1] That is, possessing $d(d+1)/2$ Killing vector fields, which are infinitesimal generators of the isometries of the spacetime. See Carroll (2004) for discussion.

classified as timelike, null or spacelike according to whether $\mathrm{d}s^2$ is less, equal or greater than zero, respectively. Paths $\gamma(\sigma) \in M$, $\sigma \in I \subset \mathbb{R}$ in spacetime can then be classified likewise according to whether $g_{\mu\nu}(\gamma(\sigma))\dot{\gamma}^\mu\dot{\gamma}^\nu$ is negative, equal to or greater than zero. Here $\dot{\gamma}^a = \mathrm{d}\gamma^a/\mathrm{d}\sigma$, and $\gamma^\mu = x^\mu \circ \gamma$, where x^μ are some local coordinates. Since spacelike paths imply velocities that are greater than the speed of light, material particles and photons can only follow timelike or null paths, respectively.

The path followed by an unaccelerated particle is then a straight line in a curved space. This is described by the *geodesic equation*, which in analogy to flat space can be obtained by either finding the extremal curve γ of $\int_\gamma \sqrt{-(\mathrm{d}s/\mathrm{d}\sigma)^2}\mathrm{d}\sigma$ or demanding that the path parallel transports its own tangent vector $\dot{\gamma}^a$. The result is

$$\ddot{\gamma}^c + \Gamma^c{}_{ab}\gamma^a\gamma^b = 0. \tag{3.20}$$

3.2.2 Precession of the pericenter

Around both spinning ($\chi > 0$) and non-spinning ($\chi = 0$) black holes, the first order deviation from Newtonian dynamics is the precession of the pericenter ω of bound orbits. For a bound orbit with semi-major axis a and eccentricity e around a black hole of mass M, we first define, following Merritt (2013), the penetration parameter

$$P = \frac{(1-e^2)a}{GM} = \frac{2(1+e)r_p}{r_{\mathrm{Sch}}}, \tag{3.21}$$

where $r_p = (1-e)a$ is the Newtonian pericenter distance. Then by defining

$$A_1 = 6\pi P^{-1} \tag{3.22}$$

$$A_2 = 4\pi\chi P^{-3/2} \tag{3.23}$$

$$A_3 = -3\pi\chi^2 P^{-2} \tag{3.24}$$

the amount of pericenter precession $\Delta\omega$ during one orbit can be shown to be

$$\Delta\omega = A_1 - 3A_2\cos i - \frac{1}{2}A_3(1 - 5\cos^2 i), \tag{3.25}$$

where i is the inclination of the orbit from the equatorial plane of the black hole. We see that in terms of c, the speed of light, the corrections are

proportional to $A_1 \propto c^{-2}$, $A_2 \propto c^{-3}$ and $A_3 \propto c^{-4}$. For nonspinning black holes only the lowest order correction is nonzero. This result is valid only in the limit that the mass m of the orbiting particle is $m \ll M$, so that its effect on the metric is negligible.

For the case of OJ287, using the parameters from Table 2.1, we find that $M/m \sim 130$, so this condition is at least weakly satisfied. Using the inclination reported in Paper V, $i = 50°$, and $a = 11500$ AU, we find, for OJ287,

$$Pc^2 = 35.46 \tag{3.26}$$
$$A_1 = 0.5316 \tag{3.27}$$
$$A_2 = 0.01666 \tag{3.28}$$
$$A_3 = -5.877 \times 10^{-4} \tag{3.29}$$
$$\Delta\omega_{\mathrm{OJ287}} = 29° \text{ per orbit.} \tag{3.30}$$

This is less than the value in Table 2.1, partly due to the new value for the inclination, and partly because equation (3.25) is an analytic approximation valid only for a vanishing mass ratio. The value in Table 2.1 is the result from a full PN-accurate simulation.

3.2.3 Precession of the orbital plane

At higher orders, the orbital plane itself precesses. This can be quantified by the change $\Delta\Omega$ in the longitude of the ascending node Ω during one orbit. From Merritt (2013),

$$\Delta\Omega = A_2 - A_3 \cos i. \tag{3.31}$$

Thus we see that the lowest order term here is $\mathcal{O}\left(c^{-3}\right)$.

Again, for OJ287, we find

$$\Delta\Omega_{\mathrm{OJ287}} = 0.98° \text{ per orbit.} \tag{3.32}$$

3.2.4 Gravitational radiation

If there are no gravitational fields, spacetime is flat. We can then consider the limit of very weak gravitational fields. A spacetime can be said to be

nearly flat, if there exist coordinates on it for which

$$g_{\mu\nu} = \eta_{\mu\nu} + h_{\mu\nu}, \quad \text{where} \tag{3.33}$$

$$\left|h_{\mu\nu}\right| \ll 1, \tag{3.34}$$

at every point (Schutz 1985). These coordinates are called nearly Lorentzian coordinates. In these coordinates we can frame our physics as given by the tensor field $h_{\mu\nu}$ on a *flat* spacetime. The result resembles electrodynamics in SR. See Schutz (1985) for a lucid discussion. Using the trace-reversed $\bar{h}_{\mu\nu} = h_{\mu\nu} - \eta_{\mu\nu}h^{\alpha}{}_{\alpha}/2$, the harmonic gauge condition $\nabla_{\alpha}\nabla^{\alpha}x^{\mu}$ and keeping terms to first order in $\bar{h}_{\mu\nu}$, the linearized Einstein field equations (3.16) are

$$\Box\bar{h}_{\mu\nu} = \partial_{\alpha}\partial^{\alpha}\bar{h}_{\mu\nu} = -16\pi G T_{\mu\nu}\,, \tag{3.35}$$

where, in general, the operator $\Box = \nabla_{\alpha}\nabla^{\alpha}$, called the d'Alembertian (Carroll 2004). For a vacuum, the result is the homogeneous equation

$$\Box\bar{h}_{\mu\nu} = 0, \tag{3.36}$$

which is the wave equation in SR. It is thus seen that gravitational waves propagate at the speed of light (Landau & Lifshitz 1975).

Equation (3.36) admits superpositions of plane wave solutions

$$\bar{h}_{\mu\nu} = C_{\mu\nu}\exp\left(ik_{\alpha}x^{\alpha}\right), \tag{3.37}$$

where k^{μ} is a constant vector and $C_{\mu\nu}$ a constant symmetric tensor. After accounting for degrees of freedom, from the choice of gauge and coordinates, in these constants, two degrees of freedom remain (Schutz 1985). These are the polarization states h_{+} and $h_{\times}$ of gravitational radiation.

The full equation (3.36) can be solved for an isolated mass distribution with arbitrary motions with the limitation that the source is much smaller than the distance of the observation point to it and the motions happen at a speed much smaller than the speed of light. The result at a point $(t, \vec{x})$, when spatial origin is set at the center of the distribution, is

$$\bar{h}_{ij}(t,\vec{x}) = \frac{2G}{3R}\frac{\mathrm{d}^2 q_{ij}}{\mathrm{d}t^2}(t_r), \tag{3.38}$$

where Latin letters now refer to spatial indices, $R = \|\vec{x}\|$, $t_r = t - R$ is the

retarded time, and

$$q_{ij}(t) = 3\int y^i y^j T_{00}\,(t,\vec{y})\mathrm{d}^3y = 3\int y^i y^j \rho(t,\vec{y})\mathrm{d}^3y \tag{3.39}$$

is the *quadrupole moment tensor*, with $\rho(t,\vec{y})$ the mass density at $\vec{y}$ at time t (Landau & Lifshitz 1975). The rate of energy lost by the system via gravitational radiation, $P = \mathrm{d}E/\mathrm{d}t$, can be shown to be

$$P = \frac{G}{45}\,\frac{\mathrm{d}^3Q^{ij}}{\mathrm{d}t^3}\frac{\mathrm{d}^3Q_{ij}}{\mathrm{d}t^3}\bigg|_{t=t_r}, \tag{3.40}$$

where $Q_{ij} = q_{ij} - \frac{1}{3}\delta_{kl}q^{kl}$ is the traceless part of the quadrupole moment tensor (Peters & Mathews 1963; Landau & Lifshitz 1975). Similarly, angular momentum is lost at a rate of[2]

$$\frac{\mathrm{d}L_i}{\mathrm{d}t} = -\frac{18}{5}G\epsilon_{ij}{}^{k}\,\frac{\mathrm{d}^2Q^{jm}}{\mathrm{d}t^2}\frac{\mathrm{d}^3Q_{km}}{\mathrm{d}t^3}\bigg|_{t=t_r}, \tag{3.41}$$

where L_i is the component of the angular momentum and $\epsilon_{ij}{}^{k}$ is the completely antisymmetric unit pseudotensor (Peters & Mathews 1963). We note that equation (3.38) is of the order $\mathcal{O}\left(c^{-4}\right)$ and (3.40) is of the order $\mathcal{O}\left(c^{-5}\right)$. Gravitational radiation is thus a very small effect, and of higher order than the previous effects discussed.

Using equations (3.40) and (3.41) it is possible to derive the rates of change for the energy, the angular momentum, the semi-major axis and the eccentricity for a binary of point masses, averaged over one period. For a binary with masses m_1, m_2, a semi-major axis a and an eccentricity e, the

[2]The difference by a factor of 9 of equation (3.41) to the corresponding eq. in Peters & Mathews (1963) is due to the fact that Peters & Mathews (1963) use $q^{ij} = \sum_a m_a x_a{}^i x_a{}^j$, which is smaller than equation (3.39) by a factor of 3 .

result is (Peters & Mathews 1963; Peters 1964)

$$\left\langle \frac{\mathrm{d}E}{\mathrm{d}t} \right\rangle = -\frac{32}{5} \frac{G^4 m_1^2 m_2^2 (m_1 + m_2)}{a^5 (1 - e^2)^{7/2}} \left(1 + \frac{73}{24} e^2 + \frac{37}{96} e^4 \right) \tag{3.42}$$

$$\left\langle \frac{\mathrm{d}L}{\mathrm{d}t} \right\rangle = -\frac{32}{5} \frac{G^{7/2} m_1^2 m_2^2 (m_1 + m_2)^{1/2}}{a^{7/2} (1 - e^2)^2} \left(1 + \frac{7}{8} e^2 \right) \tag{3.43}$$

$$\left\langle \frac{\mathrm{d}a}{\mathrm{d}t} \right\rangle = -\frac{64}{5} \frac{G^2 m_1 m_2 (m_1 + m_2)}{a^3 (1 - e^2)^{7/2}} \left(1 + \frac{73}{24} e^2 + \frac{37}{96} e^4 \right) \tag{3.44}$$

$$\left\langle \frac{\mathrm{d}e}{\mathrm{d}t} \right\rangle = -\frac{304}{15} e \frac{G^3 m_1 m_2 (m_1 + m_2)}{a^4 (1 - e^2)^{5/2}} \left(1 + \frac{121}{304} e^2 \right). \tag{3.45}$$

From the last two equations, we find, for OJ287,

$$\left\langle \frac{\mathrm{d}a}{\mathrm{d}t} \right\rangle_{\mathrm{OJ287}} = -0.43 \text{ AU yr}^{-1} \tag{3.46}$$

$$\left\langle \frac{\mathrm{d}e}{\mathrm{d}t} \right\rangle_{\mathrm{OJ287}} = -1.1 \times 10^{-5} \text{ yr}^{-1}. \tag{3.47}$$

These lead to the merger t_m and circularization t_c timescales of

$$t_m = \frac{a}{-\left\langle \mathrm{d}a/\mathrm{d}t \right\rangle_{\mathrm{OJ287}}} = 26000 \text{ yr} \tag{3.48}$$

$$t_c = \frac{e}{-\left\langle \mathrm{d}e/\mathrm{d}t \right\rangle_{\mathrm{OJ287}}} = 61000 \text{ yr}. \tag{3.49}$$

From a cosmological perspective, these timescales are short. As an example, the time from a galaxy merger to the eventual merger of the central black holes is around 10^8 years (Iwasawa et al. 2011). We are thus observing OJ287 at a somewhat unlikely time, just moments before the merger of its supermassive black holes.

3.3 Numerical methods

After describing some expected relativistic effects for a close SMBH binary, we need to see how to numerically propagate the evolution of such a system so that these effects are closely modelled.

3.3.1 Numerical relativity

One possibility is to solve the coupled partial differential equations (PDEs) (3.16) numerically for the given initial conditions. This is a tricky business, since it requires specifying sufficient and permissible initial conditions, so that the problem is well posed, while simultaneously managing gauge ambiguities. The field has progressed rapidly in the recent years, with advances in methods and computing power, reaching the point where it starts to overlap with the Post–Newtonian methods described below (Lousto & Zlochower 2013). Methods in full numerical relativity are, however, still restricted by computation power and numerical divergences to a rather limited number of orbital periods for systems like OJ287.

3.3.2 Geodesics and self gravity

SMBB orbits can still be considered from a strictly relativistic point of view, if we make simplifying assumptions. A natural starting point is to consider the limit in which the smaller body has a negligible mass, and does not contribute to the metric of the space. In this case, the orbit of the smaller body is given by the geodesic equation of a massive test particle[3] in the spacetime solution dictated by the more massive black hole. Equation (3.20) can be integrated directly, but is of second order. A more effective method is to put the original variational problem into a Hamiltonian form, by first noting that equation (3.20) can be derived from a Lagrangian of the form

$$\mathcal{L}(x, \dot{x}) = \frac{1}{2} g_{ab}(x) \dot{x}^a \dot{x}^b. \tag{3.50}$$

The generalized momenta are then

$$p_a = \frac{\partial \mathcal{L}}{\partial \dot{x}^a} = \dot{x}_a, \tag{3.51}$$

and the Hamiltonian

$$H(x, p) = p_a \dot{x}^a - \mathcal{L}(x, \dot{x}) = \frac{1}{2} g^{ab} p_a p_b. \tag{3.52}$$

[3]It should be noted that the geodesic equation for a massive body, even a vanishing test mass, gives different solutions than the geodesic equation for zero mass particles, i.e. light rays.

From the Hamiltonian we get the Hamiltonian equations of motion

$$x^a = \frac{\partial H}{\partial p_a} = g^{ab} p_b \tag{3.53}$$

$$p_a = -\frac{\partial H}{\partial x^a} = -\frac{1}{2}\frac{\partial g^{cd}}{\partial x^a} p_c p_d. \tag{3.54}$$

Equations (3.53) are of first order, but are coupled and typically nonlinear. Their propagation is, however, simple using for example middle-point iteration (see e.g. Mikkola & Aarseth 2002), a combination of iteration and the Auxiliary Velocity Algorithm (AVA) (Hellström & Mikkola 2010), or the Auxiliary Velocity and Position (AVP) algorithm (see Section 3.4.3) within an extrapolation scheme such as the Gragg–Bulirsch–Stoer scheme (Gragg 1965; Bulirsch & Stoer 1966).

However, geodesic motion only gives the correct orbit to the zeroth order of the particle mass m. To improve upon this, we can consider a perturbation, h_{ab}, to the metric caused by the mass of the particle. This causes a situation where the particle affects the gravitational field, and is in turn affected by it, a concept known as *self-force*. This is much akin to the problem of self-force of a charged particle in electrodynamics, a problem also known as *radiation reaction force*, which interestingly is still a fundamentally unsolved problem after roughly a century of research (see e.g. Feynman (1964) or Medina (2006) for an introduction).

This perturbation can be handled in two complementary fashions: either as a self-accelerated motion with a background metric g_{ab}, or as a geodesic motion with a perturbed metric $g_{ab} + h_{ab}$. For comprehensive reviews on this subject, see Poisson (2004), Detweiler (2005) and Barack (2009). In the latter case, quickly recapping Detweiler (2005), we see that for a massive point particle, h_{ab} diverges at the location of the particle, due to contributions from terms of form m/r, where r is the coordinate distance from the particle position. This singular part ${h^S}_{ab}$ can be subtracted from h_{ab}, leaving a regular contribution ${h^R}_{ab}$. The motion of the particle can then be shown to be a geodesic in a perturbed spacetime $g_{ab} + {h^R}_{ab}$, to order $\mathcal{O}(m)$. The result is that the 4-velocity u^a of the geodesic is determined from

$$u^b \nabla_b u^a = -(g^{ab} + u^a u^b) u^c u^d \left(\nabla_c {h^R}_{db} - \frac{1}{2} \nabla_b {h^R}_{cd} \right), \tag{3.55}$$

where the covariant derivative and normalization of u^a are now compatible with respect to the background metric g_{ab} (Detweiler 2005). The left side of equation (3.55) is equivalent to the left side of (3.20), and the right side is the contribution from the gravitational self-force.

3.3.3 Post–Newtonian expansion

Conceptually, the simplest approach is to consider the system as a Newtonian one, but with a perturbation that is dependent on the values of v/c, the ratio of orbital velocity to the speed of light, and the strength of the local gravitational field, ϕ. In quantitative terms, we require that

$$\epsilon = \max\left\{\left|\frac{T^{0i}}{T^{00}}\right|, \left|\frac{T^{ij}}{T^{00}}\right|^{1/2}, \left|\frac{\phi}{c^2}\right|^{1/2}\right\} \sim \frac{v}{c} \ll 1, \tag{3.56}$$

where i and j now refer to spatial indices (Blanchet 2006). We can now consider a perturbative solution given to some order in ϵ.

This can be achieved in somewhat similar manner as in the Sections 3.2.4 and 3.3.2. In harmonic coordinates (also called de Donder coordinates), the gravitational field amplitude is defined as

$$h^{\mu\nu} = \sqrt{-g}g^{\mu\nu} - \eta^{\mu\nu}, \tag{3.57}$$

where $g = \det(g_{ab})$ (Blanchet 2006), with which the coordinate condition reads

$$\partial_\mu h^{\alpha\mu} = 0. \tag{3.58}$$

Like previously, h^{ab} can be viewed as a tensor field of perturbations propagating on a Minkowskian spacetime, with the metric η_{ab}. With these coordinates, the field equations read

$$\Box h^{\mu\nu} = 16\pi G\tau^{\mu\nu}, \tag{3.59}$$

where now $\Box = \eta^{\mu\nu}\partial_\mu\partial_\nu$, and $\tau^{\mu\nu}$ is the stress–energy *pseudotensor* (Blanchet 2006). It reads

$$\tau^{\mu\nu} = |g|\, T^{\mu\nu} + \frac{1}{16\pi G}\Lambda^{\mu\nu}, \tag{3.60}$$

where now, in addition to matter and energy contribution from $T^{\mu\nu}$, we have a contribution from the field $h^{\mu\nu}$ in the form of $\Lambda^{\mu\nu}$ (Blanchet 2006). The stress–energy pseudotensor is nonlinear in $h^{\mu\nu}$, as the system of equations (3.59) is still exact, but it can be linearized to desired order to obtain Post–Newtonian expansions.

The system of equations (3.59) admits a formal (retarded) solution of the form

$$\eta_{\mu\nu}(t,\vec{x}) = \int_{\mathcal{C}} \frac{\tau^{\mu\nu}(t - \|\vec{x}-\vec{x}'\|\,,\vec{x}')}{\|\vec{x}-\vec{x}'\|}\mathrm{d}\vec{x}', \tag{3.61}$$

where $\mathcal{C}$ is the past null-cone (points on paths x^a with $g_{ab}\dot{x}^a\dot{x}^b \equiv 0$, extending to $x^0 \leq t$) (Will 2011). This equation can be solved starting from the weak field limit, equation (3.34), and then iteratively back-substituting (Will 2011). Further imposing the PN-condition, equation (3.56), a final result can, in principle, be obtained to some desired order in v/c. In practice, severe difficulties arise, which can be surmounted in different orthogonal ways, see Blanchet (2006) and Will (2011) for in-depth and short reviews, respectively. Current state of the art is at the 3.5PN level, that is to $\mathcal{O}\left(\epsilon^7\right)$, with the 4PN order a subject of active research, with current progress demonstrated in e.g. Foffa & Sturani (2013) and Bini & Damour (2013).

The final result are the Post–Newtonian formulae for the equations of motion of a Newtonian binary with a perturbation. These can be written in a fiducial form as

$$\begin{aligned}\frac{\mathrm{d}^2\vec{r}}{\mathrm{d}t^2} = \frac{G(m_1+m_2)}{r^2}\Big[&-\vec{n} + c^{-2}\vec{A}_{1\mathrm{PN}} + c^{-4}\vec{A}_{2\mathrm{PN}} + c^{-5}\vec{A}_{2.5\mathrm{PN}} \\ &+ c^{-6}\vec{A}_{3\mathrm{PN}} + c^{-7}\vec{A}_{3.5\mathrm{PN}} + \mathcal{O}\left(c^{-8}\right)\Big],\end{aligned} \tag{3.62}$$

where m_i are the masses of the components, $\vec{r} = \vec{x}_1 - \vec{x}_2$ is their relative separation, $r = \|\vec{r}\|$, $\vec{n} = \vec{r}/r$ and the Post–Newtonian terms $\vec{A}_{\mathrm{kPN}}$ depend on $\vec{x}$ and $\mathrm{d}\vec{x}/\mathrm{d}t$, and grow rapidly in algebraic complexity with increasing order (Will 2011).

A further complication is spinning bodies, for which the spin angular momentum of the orbiting bodies must be considered. This leads to an equation of motion for the components of spin, as well as spin–orbit and spin–spin contributions to the equations of motion of the orbit. Finally, a

quadrupole–monopole interaction term, arising from considering one body as a monopole in the quadrupolar field of the other, must also be taken into account. This finally leads to equations of the form

$$\begin{aligned}\frac{\mathrm{d}^2\vec{r}}{\mathrm{d}t^2} = \frac{G(m_1+m_2)}{r^2}\Big[&-\vec{n} + c^{-2}\vec{A}_{\mathrm{1PN}} + c^{-3}\vec{A}_{\mathrm{SO}} \\ &+ c^{-4}\left(\vec{A}_{\mathrm{2PN}} + \vec{A}_{\mathrm{Q}} + \vec{A}_{\mathrm{SS}}\right) + c^{-5}\vec{A}_{\mathrm{2.5PN}} \\ &+ c^{-6}\vec{A}_{\mathrm{3PN}} + c^{-7}\vec{A}_{\mathrm{3.5PN}} + \mathcal{O}\left(c^{-8}\right)\Big] \end{aligned} \tag{3.63}$$

$$\frac{\mathrm{d}\vec{s}_1}{\mathrm{d}t} = \left[c^{-2}\vec{\Omega}_{\mathrm{SO}} + c^{-3}\left(\vec{\Omega}_{\mathrm{SS}} + \vec{\Omega}_{\mathrm{Q}}\right)\right] \times \vec{s}_1, \tag{3.64}$$

where SO, SS and Q refer to the spin–orbit spin–spin and quadrupole–monopole contributions respectively, $\vec{s}_1$ is the unit spin vector of the first body, and the equations for the second body are obtained by relabeling $1 \leftrightarrow 2$ and changing signs of vectorial quantities appropriately. The forms of the coefficients are lengthy, and can be found in Appendix A.1.

3.4 Application of the numerical results to OJ287

The applications of these numerical methods to the case of OJ287 are instantly obvious. An accurate calculation of the relativistic orbit is necessary for timing accretion disk impacts. An accurate timing allows both for stricter confidence limits on the model parameters as well as more accurate predictions of future outbursts. The binary model in Lehto & Valtonen (1996) used terms accurate to 2.5PN, while Valtonen et al. (2010b) brought this up to 3.5PN. In Valtonen et al. (2011b) the previously omitted $\vec{A}_{\mathrm{SS}}$, $\vec{\Omega}_{\mathrm{SS}}$ and $\vec{\Omega}_{\mathrm{Q}}$ were also incorporated. In addition to the PN effects on the binary orbits, the effects on the circumprimary accretion disk can also be considered. A new numerical code was developed for this purpose, and used in Papers I and III. The code is described in the following section.

The results for geodesics, particularly equation (3.53), can also be used to numerically propagate a series of light rays, in a technique commonly known as ray-tracing, to render physically correct images of the system. This is the most direct way of simulating how the resolved OJ287 system would look like in various spectral bands. This is discussed in Section 3.4.2.

3.4.1 Binary and disk orbit simulation

In Papers I and III a new numerical code developed by the author was used, using PN-perturbations up to and including the 3.5PN order, however leaving out the terms $\vec{A}_{\rm SS}$, $\vec{\Omega}_{\rm SS}$ and $\vec{\Omega}_{\rm Q}$, since these depend on the secondary spin, which was not used in the model at the time, and by their omission computational effort was saved. Furthermore, the results in Valtonen et al. (2011b) show that the inclusion of the omitted terms does not have a significant effect on the model parameters. These perturbations were applied to the binary dynamics, as well as the n-body dynamics of the circumbinary accretion disk, simulated with massless particles. This was done to ensure that effects such as the Bardeen–Petterson effect (Bardeen & Petterson 1975) of accretion disk alignment with black hole spin were properly accounted for. In practice, this was done by calculating the PN corrections assuming a binary formed of the black hole (primary or secondary) and the disk particle. Combined with a viscosity prescription, this gives the correct PN-accurate description of the disk dynamics, when self-gravity, magnetic fields and radiative effects of non-viscous nature are neglected.

The omission of self-gravity is not a significant defect, since it is important only in the outer part of a thin accretion disk, where the disk is no longer radiation dominated. The black hole binary OJ287, on the other hand, is entirely contained within the inner radiation dominated part of the disk. Leaving out magnetic effects of non-viscous nature is in line with standard α-disk theory, in which the magnetic field contribution to pressure and through it to viscosity is the most important magnetic effect. Magnetic pressure and the main cause of viscosity, the magnetorotational instability (Balbus & Hawley 1991), are both captured in the α viscosity prescription, explained below. Additional magnetic effects, such as magnetic buoyancy, which causes an accretion disk corona to form, are of lesser magnitude (Stella & Rosner 1984). Ignoring radiative effects may not always be a good assumption, since the inner parts of the accretion disk may not be radiatively efficient, and thus may fail to cool fast enough to remain geometrically thin. Radiation pressure may then expand the disk to an slim disk (Abramowicz et al. 1988) or an advection dominated disk (Narayan & Yi 1994; Narayan 2005). This geometrical thickening would have the effect of that the true accretion rates by the secondary would be flattened compared to the results obtained from the simulation, but would otherwise likely not be significant.

To simulate an accretion disk with particles, an artificial viscosity has to be implemented so that angular momentum can be transported within the disk. The physical reality of this mechanism in various disk configurations has been the subject of much research, with one currently favored mechanism being the magnetorotational instability (MRI) (Balbus & Hawley 1991; Kirillov & Stefani 2013). We opted to use a prescription ignorant of the physical mechanism, and parametrized by one interaction constant, α, in the vein of the original α-disk prescription in Shakura & Sunyaev (1973). In our method, we first divide the disk into 2-dimensional cells in a logarithmic polar grid adapted from Miller (1976). The cells are indexed by $u, v \in \mathbb{Z}$, with $0 \leq u \leq N_R$ and $0 \leq v \leq N_\theta$, where N_R and N_θ are the number of subdivisions in radial and angular directions, respectively. The cell boundaries are obtained from

$$r(u) = R_c \exp(\Delta\theta u) \tag{3.65}$$

$$\theta(v) = \Delta\theta v \tag{3.66}$$

$$\Delta\theta = \frac{2\pi}{N_\theta} \tag{3.67}$$

$$R_c = R_m \exp\left(-\frac{2\pi N_r}{N_\theta}\right), \tag{3.68}$$

where the parameters R_m and R_c define the maximum and minimum radial extent of the grid. Only one of these is a free parameter, with the other following from equation (3.68). This definition of the grid has the desirable property that the gridcells are nearly square.

We then calculate the kinematic viscosity, $\nu = \mu/\rho$, in the disk as a function of radial distance, r, from the primary black hole. Here μ is the dynamical viscosity and ρ is the density of the disk matter. We are considering the inner disk, which we assume to be radiatively dominated such that the total pressure, p, is well approximated by the radiative pressure, $p_r = bT^4/3$. We then use the α-parametrization of Shakura & Sunyaev (1973) and write for the shear component $\sigma_{r\phi}$ of the stress tensor

$$\sigma_{r\phi} = \alpha p = \alpha \frac{b}{3} T^4 = \alpha \frac{4\sigma}{3c} T^4, \tag{3.69}$$

where $b = 4\sigma/(3c)$ is the radiation constant and σ is the Stefan–Boltzmann

constant. On the other hand,

$$\sigma_{r\phi} = -\mu \frac{\partial v}{\partial r} = \frac{\mu}{2}\sqrt{\frac{GM}{r^3}}, \tag{3.70}$$

if we assume that the disk particles move on approximately Keplerian orbits. If we further assume that the density is $\rho \approx n m_p$, where n is the number density of protons and m_p is the proton mass, we find, eventually,

$$\nu = \alpha \frac{8\sigma T^4}{3c\rho}\sqrt{\frac{r^3}{GM}} = \alpha A \left(\frac{r}{1\text{ pc}}\right)^{3/2} \left(\frac{M}{1\ M_\odot}\right)^{-1/2} \left(\frac{n}{1\text{ cm}^3}\right)^{-1} \left(\frac{T}{1\text{ K}}\right)^4, \tag{3.71}$$

with $A \approx 4.7 \times 10^{-6}$ pc^2/yr.

Then, for each gridcell, we use equation (3.71) to find the kinematic viscosity at the cell center, and calculate the mean velocity $\langle \vec{v} \rangle$ of the particles, in a local Cartesian frame. The viscosity force is then calculated as

$$\vec{f_i} = -\nu \left(\vec{v}_i - \langle \vec{v} \rangle \right), \tag{3.72}$$

from which the desired components (radial, azimuthal or vertical) are then used. Since the particles are massless, equation (3.72) represents force per unit mass. This method was used in the calculations of Paper I and III.

3.4.2 Imaging

Numerically propagating photon geodesics through a spacetime from or to an image plane is a direct way of constructing a simulated, physically correct image of the system. Other dynamical quantities can be propagated along the geodesic as well, enabling the calculation of e.g. the gravitational redshift or radiative transfer (Vincent et al. 2012; Younsi et al. 2012). Applying these methods to a multiple black hole system is of scientific interest, since it is a direct way of calculating the observed dynamical electromagnetic signature from the innermost parts of such a system.

However, trying to image even a binary black hole system such as OJ287 in this way runs into the problem that we do not have an analytic solution for the metric of a binary black hole. Approximate solutions have been found, such as in Gallouin et al. (2012). These can be in principle used

with equations (3.53) and the AVP algorithm described below to directly image systems such as OJ287. The problem can also be circumvented by the use of numerical relativity to calculate the metric, and then propagating the geodesics using this result, as in Vincent et al. (2012). This approach is, however, much more computationally intensive than using the approximate analytic solution, since obtaining the metric with full numerical relativity for any significant amount of time requires massive computation.

A third possible solution, proposed here, is to propagate the binary dynamics using the Post–Newtonian perturbations and then propagate the geodesic using the Kerr–Newman metrics of the two black holes alternatively, in a time–symmetric way. This process is likely to produce incorrect results when the two black holes are very near each other, and so is likely applicable only for comparatively large binary separations. A crude estimate for a sufficiently large separation r can be obtained by demanding that the binary orbital velocity v be much less than the speed of light c, so that

$$\frac{v}{c} = \frac{1}{c}\sqrt{GM\left(\frac{2}{r} - \frac{1}{a}\right)} \ll 1, \tag{3.73}$$

where $M = m_1 + m_2$ is the total mass of the binary and a is the binary semi-major axis.

3.4.3 AVP algorithm

The AVA algorithm in Hellström & Mikkola (2010) was proposed as a solution to the numerical propagation of coupled differential equations of the form

$$\dot{x} = v \tag{3.74}$$
$$\dot{v} = g(x, v). \tag{3.75}$$

As seen in Section 3.3.3, the Post–Newtonian perturbation is of this type. However, equations (3.53) are of the form

$$\dot{x} = f(x, v) \tag{3.76}$$
$$\dot{v} = g(x, v), \tag{3.77}$$

and the AVA algorithm is not directly applicable. This can be remedied by introducing both an auxiliary velocity w and an auxiliary position y, such that their initial values coincide with those of the original position and velocity. We dub this algorithm Auxiliary Velocity and Position algorithm, or AVP. The algorithm can then be written over one timestep, h, as

$$\begin{aligned} y_{1/2} &= y_0 + \frac{h}{2} f(x_0, w_0) \\ v_{1/2} &= v_0 + \frac{h}{2} g(x_0, w_0) \\ x_1 &= x_0 + h f(y_{1/2}, v_{1/2}) \\ w_1 &= w_0 + h g(y_{1/2}, v_{1/2}) \\ y_1 &= y_{1/2} + \frac{h}{2} f(x_1, w_1) \\ v_1 &= v_{1/2} + \frac{h}{2} g(x_1, w_1) \end{aligned} \tag{3.78}$$

where x, y, v and w are understood to be vector-valued as necessary. The equations (3.78) are equivalent to a second order symplectic leapfrog step in the extended phase space (x, y, v, w), and can be combined to obtain higher order symplectic propagators (Yoshida 1990). Furthermore, after one step, it is possible to combine the auxiliary and original variables, e.g. with a linear combination, to gain a more accurate solution for the original problem. Used within a Bulirsch–Stoer extrapolation scheme, as described in Mikkola & Aarseth (2002), the AVP method is fast and accurate.

3.4.4 Testing gravitational theories

The Post–Newtonian formulation discussed in Section 3.3.3 and the coefficients listed in Appendix A.1 are derived assuming that GR is the correct theory of gravity. A large number of competing gravitational theories have also been proposed, such as scalar–tensor theories (e.g. Wagoner 1970) and $f(R)$ theories (Felice & Tsujikawa 2010), which all agree with GR at the lowest order.

Attempting to constrain the number of possible theories, and thus pinpoint the most likely correct one, is a matter of great scientific interest. Some headway into this problem has been made with different independent methods at very different scales: results from the cosmological microwave

background surveys (COBE, WMAP, Planck) and observing close binaries or multiplets of singular objects such as stars, neutron stars and black holes. In the latter case, the comparison of observed orbits to predictions obtained using PN results can be used to constrain different gravitational theories.

For a binary system, where at least one of the components is a neutron star observable as a pulsar, the time-varying delays in pulse arrival times can be used to fit an orbital model that yields the eccentricity e, orbital period P, longitude of pericentre ω at epoch T_0, and the semi-major axis projected along the line of sight $a \sin i$ (Will 1993, 2014). In addition, several so-called Post–Keplerian parameters can be derived from the measured timing data. These are the average rate of periastron advance $\langle \dot{\omega} \rangle$, the amplitude γ in the pulse delays from gravitational redshift and time dilation from orbital effects, the rate of change of the orbital period $\dot{P}$ and two parameters r and s related to the so-called Shapiro time delay (Shapiro 1964) caused by spacetime curvature of the pulsar companion (Will 1993). These can be related to the observed orbital parameters by

$$\langle \dot{\omega} \rangle = 3 \left(\frac{2\pi}{P} \right)^{5/3} m^{2/3} (1 - e^2)^{-1} \tag{3.79}$$

$$\gamma = \left(\frac{P}{2\pi} \right)^{1/3} e m_2 m^{-1/3} \left(1 + \frac{m_2}{m} \right) \tag{3.80}$$

$$\dot{P} = -\frac{192\pi}{5} \left(\frac{2\pi m}{P} \right)^{5/3} \frac{\mu}{m} \left(1 + \frac{73}{24} e^2 + \frac{37}{96} e^4 \right) (1 - e^2)^{-7/2} \tag{3.81}$$

$$s = \sin i \tag{3.82}$$

$$r = m_2, \tag{3.83}$$

where m_1 and m_2 are the pulsar and companion masses, respectively, $m = m_1 + m_2$ is the total mass of the system, and $\mu = m_1 m_2 / m$ is the reduced mass(Will 1993). Since the Post–Keplerian parameters are different functions of the masses of the components, when three or more of them can be measured, they provide a consistency check for GR. The limits imposed by the parameters in (m_1, m_2) plane should all overlap in one region, which is then the GR compatible solution for the masses. To actively fit gravitational theories other than GR to the data, the Parametrized Post–Newtonian (PPN) system can be used. In this formulation, the metric is expanded in the weak field limit to order $\mathcal{O}(\epsilon^4)$ (2PN) in g_{00}, $\mathcal{O}(\epsilon^3)$ (1.5PN) in g_{0j} and $\mathcal{O}(\epsilon^2)$ (1PN) in g_{ij}, with the numerical expansion coefficients

produced by different gravitational theories replaced by parameters γ, β, ξ, α_{1-3} and ζ_{1-4}, ten in total. For the derivation and physical meaning of these parameters, see Will (1993). Using accurate orbital solutions, bounds on the differences of these parameters from those predicted by GR can then be obtained. From the nine current best bounds on these parameters, five have been obtained by pulsar measurements (Will 2014).

While the Post–Keplerian or Parametrized Post–Newtonian formalism could in principle be used with OJ287, in practice this is constrained by the orbit timing. Pulsars can have pulse repetition periods down to milliseconds, so that extensive pulse delay statistics can be obtained, and an orbital model can be fit with large number of degrees of freedom. In the case of OJ287, we are limited to two outbursts per orbit that can be used for fitting an orbital solution. Currently there are nine timed outbursts (Valtonen et al. 2011b), and an orbital model neglecting the spin of the secondary requires eight parameters (Valtonen et al. 2010b), so that only one degree of freedom remains. As such, the problem must be approached differently.

In practice, the so-called 'no-hair' or uniqueness theorems concerning black holes (Israel 1967, 1968; Hawking 1972a) can be utilized. According to these theorems, in GR, a charge neutral black hole is completely characterized by the values of its mass M and spin angular momentum J. As such, all multipole moments of the black hole must be functions of only M and J as well. In particular, the scalar quadrupole moment must be $Q_2 = -J^2/M$. In other theories of gravity, the black hole can develop 'hair', violating the theorem. This is dependent on the type of theorem, and possibly also the surrounding matter distribution (Hawking 1972b; Sotiriou & Faraoni 2012; Jacobson 1999; Horbatsch & Burgess 2012). We can use the quadrupole moment to parametrize the deviation from GR prediction by writing $Q_2 = -qJ^2/M$, with $q \in \mathbb{R}$ and $q = 1$ in GR. Through the quadrupole moment, the parameter q is then introduced to the PN terms (see Appendix A.1), and can be determined by fitting the orbit to observations. The quadrupole moment is sensitive to deviations from GR in the 2PN order, compared to the PPN formalism, which principally characterizes deviations of 1PN order. Recently, tests based on the quadrupole moment have been proposed for stars orbiting the central black hole Sagittarius A* (Sgr A*) in the Milky Way (Will 2008; Merritt et al. 2010) and direct imaging of Sgr A* (Broderick et al. 2013). However, OJ287 offers an even better probe for testing GR using the quadrupole moment, since the

Table 3.1: A comparison of maximal orbital velocity, gravitational field strength at minimum separation, and coalescence time for OJ287 and three pulsar systems recently used for high accuracy GR tests.

Name	$v_{\max}/c$	$Gm/(c^2 r_{\min})$	$P/\lvert\dot{P}\rvert$ (yr)	Ref.
PSR J0348+0432	1.97×10^{-3}	3.87×10^{-10}	1.03×10^{9}	[1]
PSR J0737-3039A	3.28×10^{-3}	9.87×10^{-10}	2.24×10^{8}	[2]
PSR J1738+0333	4.86×10^{-3}	2.37×10^{-9}	3.75×10^{10}	[3]
OJ287	2.82×10^{-1}	4.78×10^{-6}	1.64×10^{4}	[4]

[1] Antoniadis et al. (2013) [2] Kramer et al. (2006) [3] Freire et al. (2012) [4] Valtonen et al. (2010b,a)

binary in the system is more relativistic than Sgr A* and its surrounding stars. First tests were done in Valtonen et al. (2010b) and Valtonen et al. (2011b), supporting a value $q = 1.0 \pm 0.3$ (1-σ error). It is expected that the error bound can be constrained to below 10% before 2020 (Valtonen et al. 2011b).

From a physical point of view, OJ287 offers a more dramatic test of GR than the binary pulsars, since the mean value of the perturbation $\epsilon \sim v/c$ is considerably higher. Table 3.1 lists examples of pulsar systems used for recent GR tests, and the values of $v_{\max}/c \propto \epsilon$, the maximum orbital velocity as a fraction of the speed of light, $Gm/(c^2 r_{\min}) \propto \epsilon$, where $m = m_1 + m_2$, the gravitational radius of the system divided by the minimum orbital distance, which is a measure of the maximum gravitational field strength experienced by the system, and $P/|\dot{P}|$, the coalescence timescale. The figures in Table 3.1 show that in principle, OJ287 could be a more stringent test for GR than the best known pulsar systems. However, this conclusion doesn't take into account the vastly greater amount of data available for the pulsars. In addition, since both components in OJ287 are black holes with no internal structure, some scalar–tensor theories such as the Brans–Dicke theory give the same predictions as GR up to at least 2PN order, which is at the level of the quadrupole moment contribution (Will 2014). Despite these caveats, tests for theories of gravitation is likely the

most scientifically significant single application of the OJ287 binary SMBH model.

Chapter 4

Optical outbursts

The most remarkable feature of OJ287, and the one that led to the supermassive binary black hole model in the first place, is the periodic flaring at optical wavelengths. After the latest discoveries in astronomical plate archives (Paper I), the OJ287 historical V-band light curve now extends to late 19th century. Despite gaps in the light curve, the persistent nature of the 12 year periodicity leaves little doubt (Valtonen et al. 2011a).

As discussed in Chapter 2, in the LV96 model, the optical flares are caused by secondary impacts on the primary accretion disk. These impacts, and the subsequent outbursts, must be understood in order to obtain estimates of the expected outburst light curve and maximum brightness, so that the outbursts can be timed and the binary orbit can be constrained.

Long term radio observations have confirmed that OJ287 also exhibits radio flares (Nieppola et al. 2009). These may be a result of the impacts causing the optical flares, or, at the very least, related to the secondary by the way of jet helicity (Rieger 2004; Marscher et al. 2008). In this chapter, we will, however, restrict the discussion to the effects observable in the optical regime. The reasoning is two-fold: First, the optical light curve extends over a period of time long enough to argue for the existence of long term periodicities in the first place. Second, due to the amount and temporal extent of the data, the optical light curve also presents the most stringent test for any model of OJ287, binary or not.

4.1 Accretion disk impacts

The nature of the outbursts resulting from accretion disk impacts are necessarily controlled by three things: the physical nature of the primary ac-

cretion disk, the binary orbit, and the masses of the component black holes. The outbursts depend on these in the following way: the pressure, density and temperature of the gas at the impact site depend on the accretion disk. The impact velocity of the secondary, and thus the impact shock parameters, depend on the binary orbit. The secondary mass affects the outburst brightness and duration, and also the delay between the impact and the subsequent outburst. Finally, in an interlinked fashion, the mass of the primary black hole has an effect on the binary orbit and the accretion disk.

4.1.1 The model of Lehto & Valtonen

The original LV96 model (Lehto & Valtonen 1996) considered the secondary black hole impacting an accretion disk of a semi-height h, at a relative velocity of $v_{\rm rel}$, using results from Bondi–Hoyle accretion theory (Bondi & Hoyle 1944; Bondi 1952; Hunt 1971) as the theoretical basis. In this scenario, the strength of the interaction is characterized by the interaction parameter

$$\eta = \frac{c^2}{v_{\rm rel}^2}. \tag{4.1}$$

The initial shock heats the accretion disk gas to a virial temperature, $T \sim m_p v_{\rm rel}^2/k \sim 10^{10}$ K. This gas is optically thick, and the hot electrons radiate away their excess energy by bremsstrahlung in a timescale much less than the radiation diffusion timescale. The matter and radiation thus reach an equilibrium temperature given by (Bai 1966)

$$T_0 \sim \left(\frac{18 n_d m_p v_{\rm rel}^2}{7a} \right)^{1/4}, \tag{4.2}$$

where n_d is the number density of the unshocked accretion disk gas, a is the radiation constant and m_p is the mass of the proton. The gas is dominated by radiation pressure, so that the adiabatic index $\gamma = 4/3$, and the post-shock number density of the plasma is obtained from the Rankine–Hugoniot equations (Rankine 1870; Hugoniot 1889)

$$n_0 = \frac{\gamma + 1}{\gamma - 1} n_d = 7 n_d, \tag{4.3}$$

so that the compression ratio for the shock is $x = 7$. The shock front is moving at the velocity $v_{\rm rel}$, and the gas velocities before (v_1) and after shock (v_2) are related by $v_2/v_1 = n_1/n_2 = x^{-1}$, so the velocity of the post-shock gas relative to the shock is

$$v_0 = v_{\rm rel} - v_2 = \left(1 - \frac{1}{7}\right) v_{\rm rel} = \frac{6}{7} v_{\rm rel}. \tag{4.4}$$

After a time $t_{\rm dyn} = h/v_0$ from the impact, this shocked column of plasma is expected to flow out of the disk. In the LV96 model, radiative heat conduction back to the disk is dismissed, and the plasma is modelled as an uniform spherical blob, with the initial volume estimated from a cylinder formed from the Bondi–Hoyle radius of the secondary and the disk semi-height. Accounting for the compression ratio, this leads to the estimate

$$V_0 = \pi \eta^2 r_{\rm sec}^2 (h/7). \tag{4.5}$$

where $r_{\rm sec}$ is Schwarzschild radius of the secondary.

The homogeneous blob is then assumed to expand with the speed of sound c_s in the plasma, given by

$$c_s^2 = \gamma \frac{P}{\rho} = \frac{4}{3} \frac{P_{\rm rad}}{n m_p}, \tag{4.6}$$

where $P = P_{\rm rad} = aT^4/3$ is the pressure, given by the radiation pressure, and $\rho = n m_p$ is the matter density. Initially, the blob is optically thick, and cools adiabatically while it expands. Eventually, after expanding by a factor of $\tau^{4/7}$, where $\tau \sim n_0 \sigma_T R_0$ is the initial optical depth, the sphere turns optically thin and the thermal flare can be seen.

From the previous results, relations between the system parameters and maximum outburst flux density, S, outburst length, t_b, and the delay, t_0, between the shocked gas emerging from the disk and turning optically thin can estimated. The delay t_0 is found by solving $R(t_0)/R_0 = \tau^{4/7} = C$ for t_0, while the initial optical flux density can be estimated from $S \propto n(t_0)^2 T(t_0)^{-1/2} R(t_0)^3$, with $n(t_0) = C^{-3} n_0$, $T(t_0) = C^{-1} T_0$ and $R(t_0) = C R_0$, obtained by requiring adiabatic expansion. LV96 find total emissivity to scale as $(t/t_0)^{-7/2}$, and outburst duration is then obtained by solving for the time when the peak brightness has diminished by an arbitrary factor.

The results calculated in LV96 are

$$S \propto m_{\rm sec}^{22/21} v_{\rm rel}^{-23/21} h^{11/21} n^{5/14} \tag{4.7}$$

$$t_b \propto m_{\rm sec}^{20/21} v_{\rm rel}^{-59/42} h^{10/21} n^{11/28} \tag{4.8}$$

$$t_0 \propto m_{\rm sec}^{26/21} v_{\rm rel}^{-355/84} h^{13/21} n^{102/112}, \tag{4.9}$$

where $m_{\rm sec}$ is the secondary mass, $v_{\rm rel}$ the impact velocity (relative velocity between the secondary and the primary accretion disk), h the accretion disk semi-height and n the accretion disk number density.

To complete the model, an accretion disk model is required. The original LV96 model considers a thin α-disk of the Sakimoto–Coroniti type (Sakimoto & Coroniti 1981), wherein the magnetic pressure $B^2/(8\pi)$ and gas pressure P_g in the disk are assumed to be in equilibrium, so that the shearing component, $\sigma_{r\phi}$, of the stress tensor is set to $\sigma_{r\phi} = \alpha B^2/(8\pi) \sim \alpha P_g$. Applying this model to the results above then leads to estimates of outburst brightness and timings. The resulting timings are shown in Figure 4.1.

The estimates for outburst timings in Figure 4.1 differ slightly from those in the original LV96 paper. The reason is, firstly, that the orbital parameters used in the original paper differed from the ones in Table 2.1, which are based on newer data. Also, the accretion rate used for the primary, $\dot{m} = \dot{m}_{\rm Edd}$, where $\dot{m}_{\rm Edd}$ is the Eddington accretion rate, was likely overestimated. In Paper III, a newer estimate was made placing the accretion rate at $\dot{m} \sim 0.8 \times 10^{-3} \dot{m}_{\rm Edd}$. These changes affect the timing also through the accretion disk model. In addition to timing, the outburst brightness estimates in the original LV96 paper are also affected.

The shape of the outburst light curve in the LV96 model is obtained by assuming that the gas emerging from the disk is optically thick at first, and emits negligible radiation. Then, after expanding by a factor of $\tau^{4/7}$ it becomes optically thin. At this point, the emissivity rises linearly to maximum in the light crossing time of the bubble. After the maximum, the emissivity decreases as $\epsilon \propto (t/t0)^{-7/2}$ and the radius increases as $R \propto t^{2/3}$, so that the luminosity of the entire bubble decreases as $R^3\epsilon \propto t^{-3/2}$.

The September 2007 outburst was for the first time observed with polarization measurements (Valtonen et al. 2008b), and subsequently an outburst curve for the unpolarized bremsstrahlung component could be derived. In

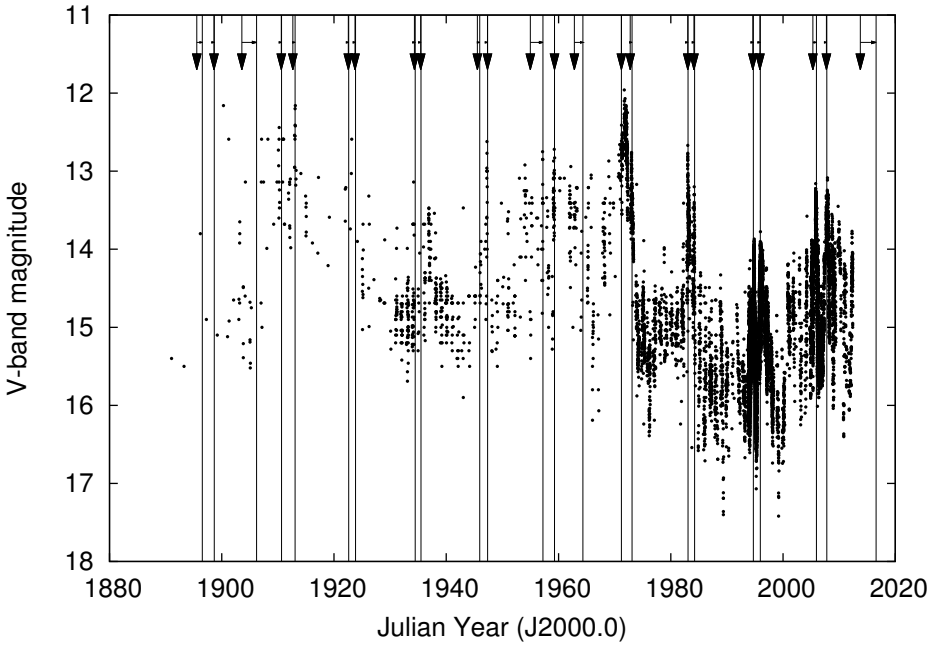

Figure 4.1: The historical OJ287 light curve (points, see Figure 2.1 for details), with disk crossing times for the model in Table 2.1 (arrows) and LV96 model estimates of outburst times (vertical lines). Time delays from disk crossing to outburst from (Valtonen 2007) (Table I) are shown by horizontal lines.

Valtonen et al. (2011b), the light curve based on measurements is given as

$$F_V(t) = \begin{cases} 2.9\left(\frac{t}{3}\right)^{1.5} f^{-1.5} & 0 \le t < 2.59 \\ 2.33 + 4.7(t - 2.59f)f^{-1} & 2.59 \le t < 3.35\,, \\ 5.6\left(\frac{t+1.5f}{5f}\right)^{-1.5} & 3.35 \le t \end{cases} \tag{4.10}$$

where F_V is the V-band spectral flux density in mJy, t is time in days, measured from the beginning of the outburst, and f is a free parameter that allows scaling of the burst duration.

4.1.2 The model of Ivanov et al.

In addition to the analytic work in LV96, Ivanov et al. (1998) also estimated the outbursts from an accretion disk impact, both analytically and numerically. The model, hereafter referred to as the I98 model, considers a standard Shakura–Sunyayev (Shakura & Sunyaev 1973) accretion disk around a primary black hole of mass $m_{\rm pri} = 10^8 M_\odot$, with a secondary of mass $m_{\rm sec} = 10^4$–$10^6\ M_\odot$ impacting the disk. The impacts are taken to happen at a distance of 10^3 Schwarzschild radii of the primary.

The assumptions in the model are thus somewhat different from the LV96 model, but one would not expect the qualitative aspects of the accretion disk collision to be much different. Further, as the results in I98 model are given as scaling laws, a direct comparison with the LV96 model can be made.

The principal results in the I98 model are the analytic estimate for the luminosity of the gas ejected in the impact and the shape and physical parameters of the ejecta. The luminosity is estimated as

$$L(t) = \frac{\pi^2}{9} L_{\rm Edd} \phi(t) = 1.4 \times 10^{43}\, m_5\, \phi(t) \text{ ergs s}^{-1}, \tag{4.11}$$

with $L_{\rm Edd} = 4\pi G m_{\rm sec} m_p c/\sigma_T$ the secondary Eddington luminosity, and

$$\phi(t) = \exp\left[-\left(1 + \frac{t}{2t_c}\right)\frac{t}{t_0}\right]. \tag{4.12}$$

This solution is the model from Arnett (1980), which is based on an adiabatically expanding optically thick sphere of radiation dominated gas, with luminosity given entirely by radiation diffusion. Here

$$t_c = 2h/v_{\rm rel} = 3 \times 10^4 \alpha_*^{-1/10} M_8^{9/10} \dot{M}_*^{1/5} r_3^{3/2} \text{ s} \tag{4.13}$$

is the dynamical timescale, given by the crossing time of the disk layer by the secondary. The second important timescale of the solution is the radiation diffusion timescale, given by

$$t_0 = \frac{3}{\pi^2 c} r_a^2 \rho_d \kappa = 2 \times 10^7 \alpha_*^{-7/10} m_5^2 M_8^{-7/10} r_3^2 \text{ s}, \tag{4.14}$$

with $r_a = 2Gm/v_{\rm rel}$ the Bondi–Hoyle accretion radius (Bondi & Hoyle 1944), ρ_d the density of the accretion disk, $\kappa = 0.4$ cm^2 g^{-1} the Thom-

son electron scattering opacity, $\alpha_* = \alpha/10^2$, $\dot{M}_* = \dot{M}/(10^{-2}\dot{m}_{\rm Edd})$, $r_3 = r/(10^3 r_{\rm pri})$ the scaled impact distance and $m_5 = m_{\rm sec}/(10^5 M_\odot)$ and $M_8 = m_{\rm pri}/(10^8 M_\odot)$ the scaled secondary and primary masses, respectively. A plot of the V-band flux density derived from equation (4.11) with the parameters from Table 2.1 is shown in Figure 4.2, compared with the original prediction from LV96.

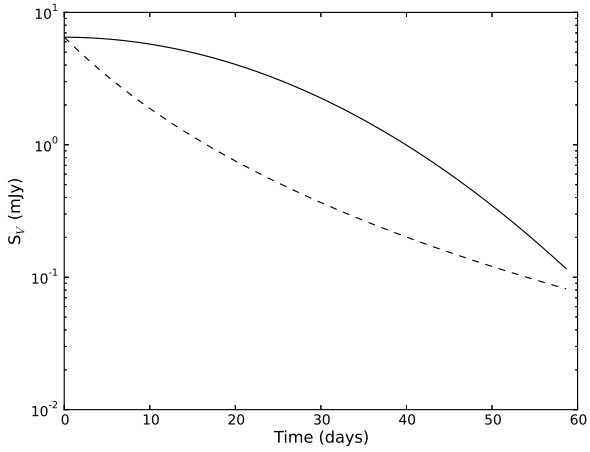

Figure 4.2: The evolution of V-band flux density of the disk impact plasma bubble after peak value of 6.5 mJy. Solid line is the I98 model, with parameters from Table 2.1. Dashed line is the original LV96 model prediction, with $t_0 \sim 23$ days.

As can be seen in Figure 4.2, the exponential decrease proposed in the I98 model is qualitatively rather different than the power law predicted by the LV96 model. The I98 model is backed up by the numerical simulations in the paper, but the power law decrease in LV96 is, however, consistent with observations. The actual situation after the black hole impact in the expanding plasma blobs is more complex than either of these models can fully encompass. Both models completely neglect magnetic fields in the system for example. Also, research on the qualities of radiation (e.g. spectral properties) from the evolving plasma after a black hole impact is still lacking. This is discussed further in Chapter 7.

Numerical simulations, the second major part in Ivanov et al. (1998),

show several important features near the impact region. First, the disk is bent towards the incoming secondary. This affects the impact timing, as noted and accounted for in Valtonen (2007). Second, after the impact there are dual approximately spherical outbursts of gas from each side of the disk, with similar physical characteristics. This explains why we can observe the outbursts regardless of the direction the secondary moves through the disk with respect to us. Third, a conical shock forms in front of the secondary, in a reversal of the typical Bondi–Hoyle accretion pattern. Most of the mass accreted by the secondary is accreted in this way. This effect is also discussed in Paper III.

4.2 Tidal flares

In addition to producing outbursts directly from the accretion disk impacts, the perturbing effect of the secondary works to increase the accretion rate of the primary (Byrd et al. 1986, 1987; Lin et al. 1988; Goodman 1993). This leads to increased brightness of the primary and to the observation of a so called tidal flare in the optical region (Valtonen et al. 2006a).

The rise in the accretion rate of the primary can be accompanied by jet brightening (Valtonen et al. 2006a), which means that a tidal flare is a combination of increased accretion disk brightness as well as jet brightness, with the jet dominating. The brightness increase is dependent on matter transfer to the jet. This relation has been theoretically estimated in Heinz & Sunyaev (2003) to be approximately

$$F_\nu \propto \dot{M}^{1.42+0.67\alpha}, \tag{4.15}$$

where F_ν is the spectral flux density, $\dot{M}$ is the accretion rate and α is the spectral index (with the convention $F_\nu \propto \nu^{-\alpha}$).

The mechanism behind the matter transfer from the disk to the jet is not entirely understood. A possible theory is based on a magnetic field threading the accretion disk and the black hole that is twisted by the rotation of both components. This twisted field can then funnel accreting matter into the jet (Ferreira & Pelletier 1995).

As the secondary is on an eccentric orbit, and impacts the accretion disk of the primary twice in quick succession, the precursor flares, described in the next section, impact flares and tidal flares form a continuous season of flaring activity. Discerning the nature of the flares requires the measure-

ment of timing, polarization or light curve shape, or a combination of them all.

4.3 Precursor outbursts

The third type of outburst exhibited by OJ287 is the so-called precursor outburst or precursor flare, as named in Kidger et al. (1993). These quick outbursts seem to happen before the start of a flaring season, that is *before* the secondary has reached the accretion disk after passing apocentre. So far, only three cases have been observed, in 1993 (Kidger & Takalo 1994; Kidger et al. 1995), 2004 (Valtonen et al. 2006a) and 2012 (Paper III).

In Paper III, we proposed a theory where the precursor flares are caused by the secondary impacting and accreting a part of a plasma cloud as it travels through the corona of the accretion disk of the primary. The intuitive basis of the theory rests first on the fact that accretion disks are likely to have coronas (Svensson & Zdziarski 1994; Wang et al. 2004). Second, as the secondary periodically impacts the primary and tears off plasma from the accretion disk of the primary, the primary corona will end up hosting numerous plasma clouds at any one time, in pressure equilibrium with the corona. Third, the secondary can reasonably be expected to have a high spin that is aligned with the spin of the primary so that the Doppler boosting factors are similar (Paper II, see also Section 5.3.2). Higher spin in turn has been shown to result in markedly greater jet luminosity (MacDonald & Thorne 1982; McKinney 2005, see also Section 5.3.2), which allows the much less massive secondary to temporarily exceed the primary in brightness.

During the impact, the mass of the column of the plasma cloud matter interacting with the secondary is

$$\delta m = \Sigma_0 r_{\rm sec}^2 \eta^2 k^{-2}, \tag{4.16}$$

where $\Sigma_0 = 10^5$ g cm^{-2} is the initial surface mass density of the primary accretion disk at the impact site, $r_{\rm sec}$ is the secondary Schwarzschild radius, $\eta = c^2/v_{\rm rel}^2$ is the interaction parameter and $k \sim 20$ is the subsequent expansion factor of the cloud after separating from the disk. The luminosity of the outburst can be estimated from the accretion rate of the secondary during the collision. To this end, we estimate the fraction of the mass δm of the cloud accreted by the colliding secondary, which

is approximately $\delta m = \Sigma_0 r_{\rm sec}^2 \eta^2 k^{-2} \sim 0.25(k/20)^{-2}\ M_\odot$. The crossing time t_c is approximately $t_c \sim 0.03(k/20)$ yr, and the accretion rate is $\delta m/t_c \sim 8(k/20)^{-3}\ \dot{m}_{\rm Edd}$ in units of the Eddington accretion rate of the secondary. Of this accreted matter, only material ending up near the secondary can power an outburst immediately. In Paper III, this fraction is estimated to be $1/\eta$ of the total accreted mass, so that the maximal luminosity of the outburst is approximately $L \sim 0.25(k/20)^{-3}\ L_{\rm Edd}$, where $L_{\rm Edd} = 2 \times 10^{46}\ {\rm erg\,s^{-1}}$ is the Eddington luminosity of the secondary, assuming an accretion efficiency of $\epsilon = 0.3$. The timescale of the outburst can then be estimated to be no more than approximately 10 days.

As found in Paper III, these results are in good agreement with the observations in the optical regime. To confirm whether the origin of these outbursts is really the secondary, observations of a precursor outburst with a high time resolution of $\lesssim 1\,{\rm h}$ are needed, to resolve timescales at the innermost stable circular orbit (ISCO) of the secondary. Alternatively, as the OJ287 binary subtends approximately 0.01 mas on the sky, with the possibility of future instruments operating at sub-milliarcsecond resolution (Eisenhauer et al. 2011), the source of the outbursts could be resolved directly.

Chapter 5

Jet structure

In this chapter, the basic physics of relativistics jets will be briefly reviewed. These jets are a prominent component of a high-powered AGN, and understanding them is a requirement for understanding the observations we have. In the case of OJ287, relativistic jets are even more important than for most AGNs, since OJ287 is a blazar, which means that its jet is pointing almost directly towards us. This in turn means that the observed radiation from OJ287 is usually dominated by the radiation from the jet.

After reviewing the basics, the relativistic jets of OJ287 are discussed in more detail. A helical model for the jet of the primary black hole in OJ287, constructed in Paper V, is presented. Finally, results for the jet of the secondary black hole derived in Paper III and Paper IV are also presented.

5.1 Relativistic jets

A variety of astrophysical objects exhibit *jets*, collimated outflows of matter and/or radiation. These include newly forming protostars, white dwarfs, neutron stars, stellar mass black holes, gamma ray bursts (GRBs) and active galactic nuclei (AGN) (Livio 1999).

The definition of what exactly constitutes a jet is vague and can vary. Often simple geometrical limits, such as four to one ratio in length over width (Bridle 1982), are employed. Nevertheless, the asymmetric nature of the outflow is a necessary component for all these objects. By definition, a collimated outflow means a parallel, or straight outflow. Thus, unlike in a spherical expansion, the jet has a preferred direction. Most often, in the case of a rotating astrophysical object, there are two jets due to symmetry and conservation of momentum. These are directed along or nearly along

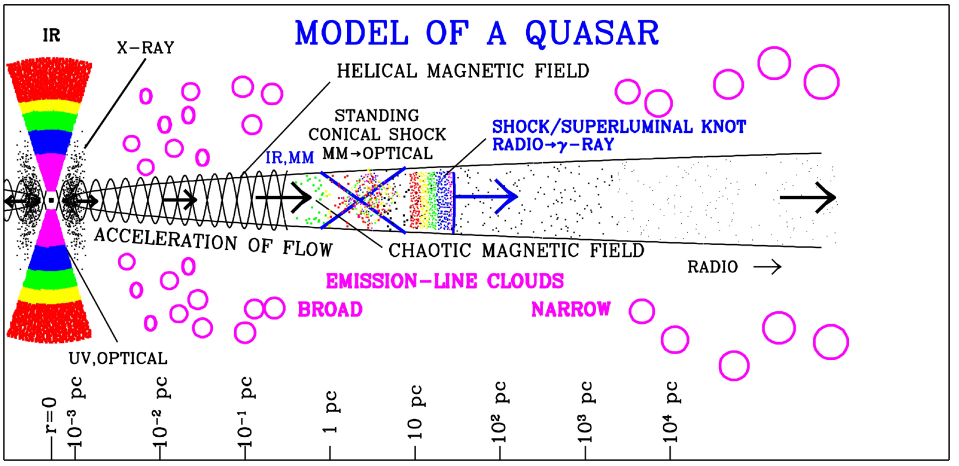

Figure 5.1: A draft of the structure of an AGN with a relativistic jet by Dr. Alan Marscher. Source: http://www.bu.edu/blazars/research.html

the rotational axis of the object. A jet of this nature is most correctly called a *polar jet*.

A subset of jets, polar or otherwise, is *relativistic jets*, by which is meant jets that exhibit bulk motion at a substantial fraction of the speed of light. The jets that emanate from AGNs are relativistic jets, with the fact now well established that the source of these jets is most likely a supermassive black hole in the core of the AGN. To be exact, the jets do not directly originate from the black hole itself, but from its immediate vicinity, around the inner edges of its accretion disk. The exact details of the jet formation is still an open problem. The relativistic jets range in power from poorly collimated weak outflows in Seyfert galaxies to the extremely tightly collimated and strong jets in Fanaroff–Riley type II (FRII) galaxies (Fanaroff & Riley 1974). The strongest jets have estimated luminosities in the 10^{48} erg s^{-1} range (Ghisellini et al. 2009), with total energies integrated over estimated active lifetimes of up to 10^{62} erg (McNamara et al. 2009). Figure 5.1 depicts a famous cartoon by A. Marscher of the general structure of a relativistic jet and the assumed origins of different radiation wavebands.

The most prominent features of a typical relativistic jet on parsec scales are the stationary *core* and the moving *knots* resolvable with VLBI observations (see Figure 2.4). The core is stationary, but its position is frequency

dependent. It is likely either a standing recollimation shock at a fixed position in the jet, or the fixed point at which the jet emission first becomes optically thin.

The knots are likely to be strong shocks in the jet. These shocks compress the transverse component of the magnetic field in the jet, as well as the jet plasma. The increase of electron density and magnetic field strength both greatly increase the emitted synchrotron radiation, as shown in Section 5.1.1. The velocity of the knots is sometimes observed to increase, suggesting that the jet acceleration mechanism is still operating at these distances (Homan et al. 2009).

On scales of 100 to 1000 parsecs the jets are observed to be more stable, with straighter trajectories and less violent changes in other physical parameters (flux density, magnetic field). Finally, the jet interacts with the ambient medium. For FRII galaxies the jet is very straight and terminates in hotspots surrounded by giant radio lobes. For FRI galaxies, suspected to be the parent population of BL Lac objects (Urry & Padovani 1995), the jet is observed to be brighter towards the core, and exhibits meandering about its general axis of progression. This difference is either intrinsic to the AGN, or extrinsic, a consequence of the surrounding environment, with the question still largely unresolved (Gendre et al. 2013).

5.1.1 Radiative characteristics

Synchrotron radiation

In addition to great luminosity, relativistic jets also radiate in a very wide spectral band, from radio to even TeV (teraelectronvolt) gamma rays. The main radiation mechanism in relativistic jets, at lower frequencies from radio to X-rays, is *synchrotron radiation*. This is the radiation emitted by electrons moving at relativistic velocities in a magnetic field. The characteristics of the radiation produced by an ensemble of electrons can then be dependent only on the magnetic field strength B, and the velocity distribution $n(\Gamma)\mathrm{d}\Gamma$ of the electrons, where n has the unit of number density, and Γ is the Lorentz gamma, directly related to electron velocity v and energy E through

$$E = \Gamma mc^2 = \frac{mc^2}{\sqrt{1 - v^2/c^2}}, \tag{5.1}$$

where m is the electron mass. For relativistic jets and astrophysical problems in general, a power law distribution is often assumed, so that

$$n(\Gamma)\mathrm{d}\Gamma = n_0\Gamma^{-p}\mathrm{d}\Gamma, \tag{5.2}$$

where n_0 is a normalization constant. Obviously, a distribution like in equation (5.2) is only valid within some range of energies given by $\Gamma \in [\Gamma_0, \Gamma_1]$.

The derivation of the characteristics of synchrotron radiation for a power law distribution of electrons is straightforward, but lengthy (see e.g. Ginzburg & Syrovatskii (1965), Blumenthal & Gould (1970) or Rybicki & Lightman (1979) for a detailed review). Omitting these details, the total power emitted per unit volume and unit frequency, or *(spectral radiant) emittance*, for an electron distribution in equation (5.2) is

$$P(\nu) = \frac{4\pi k e^3 B^{(p+1)/2}}{mc^2}\left(\frac{3e}{4\pi mc}\right)^{(p-1)/2} a(p)\nu^{-(p-1)/2}, \tag{5.3}$$

where

$$a(p) = \frac{2^{(p-1)/2}\sqrt{3}\,\Gamma_f[(3p-1)/12]\,\Gamma_f[(3p+19)/12]\,\Gamma_f[(p+5)/4]}{8\pi^{1/2}(p+1)\,\Gamma_f[(p+7)/4]}, \tag{5.4}$$

e is the electron charge, m is the electron mass, Γ_f is the Gamma function and k is a normalization constant so that $n_0 = k/(4\pi)$ (Blumenthal & Gould 1970). The function $a(p)$ varies slowly and for the range $p \in [3/2, 5]$, containing typical astrophysical values, is approximately equal to 0.1. The degree of linear polarization is (Rybicki & Lightman 1979)

$$\Pi = \frac{p+1}{p+7/3}. \tag{5.5}$$

Equation (5.5) shows that, in general, synchrotron emission is highly linearly polarized, with $\Pi \in [0.65, 0.82]$ when $p \in [3/2, 5]$. The direction of the linear polarization is perpendicular to the local direction of magnetic field (Rybicki & Lightman 1979). From equation (5.3) it can be seen that a power law distribution of electrons, equation (5.2), produces a power law in resulting spectral energy density, with an exponent $\alpha = -(p-1)/2$.

At low and high energies, however, the spectrum differs from a simple power law. Towards low energies, the absorption process correspond-

ing to synchrotron emission, *synchrotron self-absorption*, becomes important. It can be shown that the synchrotron self-absorption coefficient is related to the magnetic field strength and frequency of radiation like $\alpha_\nu \propto B^{(p+1)/2}\nu^{-(p+4)/2}$ (Rybicki & Lightman 1979). As such, self-absorption will dominate towards lower frequencies. The corresponding source function of radiative transfer is

$$S_\nu = \frac{P(\nu)}{4\pi\alpha_\nu} \propto B^{-1/2}\nu^{5/2}, \tag{5.6}$$

and, thus, in the optically thick case, the observed spectral flux density is proportional to $\nu^{5/2}$, significantly independent of p. The exponent is also different from the Rayleigh–Jeans blackbody ($\alpha = 2$), a consequence of the electron energy distribution, equation (5.2), not being a thermal distribution, i.e. a (relativistic) Maxwellian distribution.

The observed turnover frequency, ν_t, between the optically thick and optically thin cases can be analytically solved for, in some special cases. For a uniform source with an angular size θ in milliarcseconds, redshift z, magnetic field strength B in Gauss, a power law electron energy distribution $N(E)\mathrm{d}E = N_0 E^{-p}\mathrm{d}E$, and maximum spectral flux intensity S_m in Janskys, the turnover frequency ν_t is

$$\nu_t \approx f(p) B^{1/5} S_t^{2/5} \theta^{-4/5} (1+z)^{1/5} \text{ GHz}, \tag{5.7}$$

where $f(p)$ is a slowly varying function of p, with $f(2) \approx 8$ (Kellermann & Pauliny-Toth 1981). Since the spectral index for a self-absorbed source is 5/2 for $\nu < \nu_t$ and negative for $\nu > \nu_t$, the frequency of the maximal spectral flux intensity coincides with the turnover frequency. A solution also exists for a radially inhomogeneous spherical source. If the source is a spherical shell with a radial extent from r_1 to $r_2 = r_1/x$, with magnetic field strength B and electron energy distribution N given by

$$B(r) = B_1 \left(\frac{r_1}{r}\right)^m \tag{5.8}$$

$$N(E, r) = N_1 \left(\frac{r_1}{r}\right)^n E^{-p}, \tag{5.9}$$

where B_1, N_1, r_1, m and n are constants, the turnover frequency ν_t is

$$\nu_t = \left[\frac{2k_1(1-x^{1/k_1})c_2(p)N_1B_1^{(p+2)/2}r_1}{\tau_m(p)}\right]^{2/(p+4)}(1+z)^{-1}, \qquad (5.10)$$

where $k_1 = 2/[2n+m(p+2)-2]$, z is source redshift, and $c_2(p)$ is tabulated in Marscher (1977). Here the optical depth $\tau_m(p) \lesssim 1$.

At higher energies, the radiating high-energy electrons lose their kinetic energy faster via synchrotron radiation. The energy loss by synchrotron radiation for one electron averaged over the pitch angle is (Rybicki & Lightman 1979)

$$\frac{\mathrm{d}E}{\mathrm{d}t} = -P_{\mathrm{tot}} = -\frac{4}{3}\sigma_T c\beta^2\Gamma^2 U_B, \qquad (5.11)$$

where Γ is the Lorentz gamma, $\sigma_T = \frac{8\pi}{3}\left(\frac{e^2}{mc^2}\right)^2$ is the Thomson electron scattering cross-section, and $U_B = B^2/(8\pi)$ is the magnetic field energy density. For highly relativistic electrons $\beta^2\Gamma^2 \sim \Gamma^2$ and we find

$$\frac{\mathrm{d}E}{\mathrm{d}t} = -\frac{4}{9}\frac{e^4B^2E^2}{m^4c^7}. \qquad (5.12)$$

Starting with these results, it can be shown (see Blumenthal & Gould (1970) for details) that eventually, in a steady state, the electron energy distribution is proportional to $\Gamma^{-(p+1)}$, steeper by one than the initial distribution. The same result applies if the high energy losses are dominated by Thomson scattering. If the high energy losses are dominated by the Compton process, the result is proportional to $\Gamma^{-(p-1)}$, flatter by one. Finally, if bremsstrahlung is the only energy loss process, the final electron energy spectrum will be proportional to Γ^{-p}, with no change in the index.

Thus, a complete synchrotron spectrum exhibits a power law rise with an exponent 5/2 at low frequencies, a peak and subsequent decline with an exponent $-(p-1)/2$, and finally a high energy break and (typically) a steeper decline with exponent $-p/2$. These characteristics have been observationally confirmed in various synchrotron sources including radio–loud AGN with jets (Williams 1963; Zdziarski 1986), and OJ287 in particular (Worrall et al. 1982).

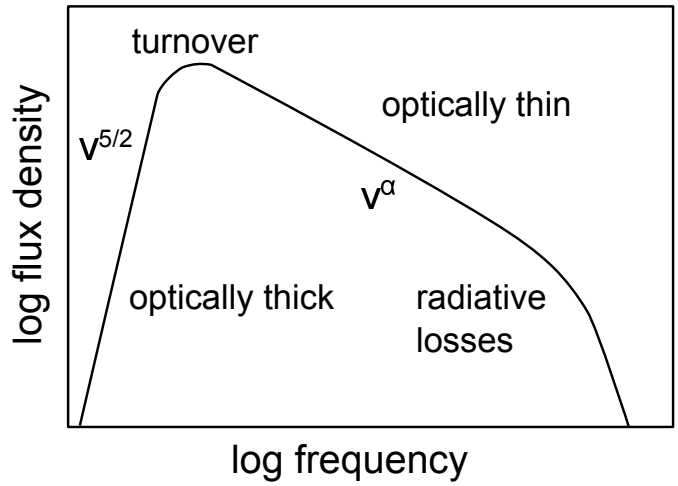

Figure 5.2: A cartoon depicting the qualitative characteristics of a synchrotron spectrum. Modelled after original image found at https://www.sao.ru/hq/giag/gps-en.html.

Synchrotron self–Compton radiation

A synchrotron radiation photon field produced by relativistic electrons in the jet can further interact with the same electron population via inverse Compton scattering. In this process, known as synchrotron self–Compton (SSC) radiation, the low energy photons are scattered by the relativistic electrons to gamma-ray energies. The SSC mechanism is likely responsible for most of the high energy radiation from a relativistic jet of a HBL source (Ghisellini et al. 1985), which means that the synchrotron process is the underlying cause for nearly all of the radiation from the relativistic jets of these sources. For LBL and flat spectrum radio quasar (FSRQ) sources, the high energy spectrum is likely produced by the external Compton mechanism, where the photon field is produced by a source outside the jet, such as the dusty torus, broad line region or the accretion disk (Böttcher & Dermer 2002; Abdo et al. 2010). However, in the case of OJ287, even though it is a LBL source, a single component SSC model still gives a reasonable fit, as seen in Figure 2.3.

The SSC process is a more complex phenomenon than pure synchrotron radiation since all interaction pairings are possible between electrons and

synchrotron photons from low to high energies. The situation is further complicated by the feedback connection: SSC energy losses cool the electron population, affecting the synchrotron radiation, which affects the SSC seed photon field and this ends up affecting the efficiency of the SSC process. Despite these difficulties, some analytic results can be derived. The total inverse Compton emittance $P_{\rm IC}$ for an isotropic photon energy density U_P is (Blumenthal & Gould 1970)

$$P_{\rm IC} = \frac{4}{3}\sigma_T c \Gamma^2 U_P. \tag{5.13}$$

When compared to equation (5.11) we find $P_{\rm tot}/P_{\rm IC} = U_B/U_P$, so the dominating radiation mechanism depends on the ratio of magnetic to radiation energy densities. However, since the Compton scattered radiation also contributes to U_P, there is a positive feedback. This causes the SSC component to increase very fast when its contribution to U_P begins to be comparable to the underlying synchrotron radiation field. This leads to very fast cooling, limiting the maximum observable rest frame brightness temperatures to $\sim 10^{12}$ K, the so-called inverse Compton limit (Kellermann & Pauliny-Toth 1969).

The spectrum for a spherical SSC source with a power law electron distribution can be shown to be approximately (Band & Grindlay 1985, 1986)

$$S_\nu = \frac{3}{4}hc\sigma_T\nu^{-(p-1)/2}\left\{2^{p+1}\left[\frac{1}{p+3}+\frac{1}{p+1}-\frac{2}{p+5}-\frac{4}{(p+3)^2}\right]\right\} \times \int {\rm d}V \int_{\nu_1}^{\nu_2} {\rm d}\nu' n(\nu', r) n_e(r) \nu'^{(p-1)/2}, \tag{5.14}$$

where p is the index of the electron distribution power law, $n(\nu, r)$ is the source photon distribution, $n_e(r)$ is the electron number density and the integrals are over the source volume and input spectrum, respectively. Significantly, equation (5.14) shows that the SSC spectrum is proportional to $\nu^{-(p-1)/2}$, so it is a power law with the same spectral index as the original synchrotron spectrum. Figure 2.3 depicts a complete SSC spectrum of OJ287, with both the synchrotron and inverse Compton peaks clearly visible.

5.1.2 Relativistic effects

The high bulk velocities and particle velocities in the relativistic jets naturally imply that (special) relativistic effects need to be accounted for to understand them. Specifically, for relativistic bulk motion of a radiating jet component, we can expect to observe *time dilation*, *Doppler shift* in frequency ν, *Doppler boosting* of spectral radiance (often called specific intensity) I_ν and, consequently, spectral flux density S_ν, *Doppler beaming* of radiation in a cone of opening angle θ, *increase in brightness temperature* T_b and *apparent superluminal velocities* β_{app} for motion closely aligned with the direction of observation. These observational effects are a result of transforming from a coordinate system of the rest frame of the radiating feature to the coordinate system of the observer. They can be thus quantified with the help of Lorentz transformations. For a jet feature radiating with a power law spectrum $S_\nu \propto \nu^\alpha$ in relativistic motion with velocity v along a line creating an angle θ with the direction of observation, we can define

$$\beta = \frac{v}{c} \tag{5.15}$$

$$\Gamma = \frac{1}{\sqrt{1-\beta^2}} \tag{5.16}$$

$$D = \frac{1}{\Gamma(1-\beta\cos\theta)}, \tag{5.17}$$

where β is the Lorentz beta, Γ is the Lorentz factor, or Lorentz gamma, and D is the Doppler factor. With these definitions, the quantified relativistic effects read:

$$\delta t = D^{-1}\delta t' \qquad \text{time dilation} \tag{5.18}$$

$$\nu = D\nu' \qquad \text{Doppler shift} \tag{5.19}$$

$$I_\nu = D^3 I'_{\nu'} \qquad \text{Doppler boosting} \tag{5.20}$$

$$S_\nu = D^{2-\alpha} S'_\nu \qquad \text{(continuous feature)} \tag{5.21}$$

$$S_\nu = D^{3-\alpha} S'_\nu \qquad \text{(discrete feature)} \tag{5.22}$$

$$\sin\theta = \Gamma^{-1} \qquad \text{Doppler beaming} \tag{5.23}$$

$$T_b = DT'_b \qquad \text{increase in } T_b \text{ (source size known)} \tag{5.24}$$

$$T_b = D^3 T_b' \qquad \text{(size estimated from variability)} \tag{5.25}$$

$$\beta_{\text{app}} = \frac{\beta \sin\theta}{1 - \beta \cos\theta} \qquad \text{apparent superluminal velocity.} \tag{5.26}$$

Here, the primed quantities refer to the physical variables as measured by an observer in the rest frame of the radiating feature. Importantly, from equations (5.20)—(5.23) it is evident that highly relativistic motion of a radiating source towards the observer will cause the source to appear much more luminous. Thus, AGN with their jets pointed nearly towards us can be observed even from high redshifts as *blazars*.

The existence of jets with relativistic motion in nature has been confirmed by numerous observations of the above phenomena, including superluminal motion (Cohen & Unwin 1982; Zensus et al. 1987; Pearson & Readhead 1988), one-sided jets (Pearson & Readhead 1988; Bietenholz et al. 2000) (due to differential Doppler boosting/fading of the approaching/receding jet) and high brightness temperatures over the inverse Compton limit (Linfield et al. 1989).

Despite these well established basic facts, relativistic jets are not nearly fully understood. Some existing points of contention include jet launching (Meier 2003; Nemmen et al. 2007; Nagakura et al. 2011), acceleration and collimation mechanisms (Meier 2003), jet composition (Kino et al. 2012), and jet stability over kiloparsec distances (McKinney & Blandford 2009).

5.2 Helical jets

Current understanding of the launching and acceleration mechanisms of a relativistic jet involves magnetic fields that are twisted due to differential rotation in the accretion disk of the black hole or the frame-dragging in the ergosphere of a rotating black hole (Blandford & Znajek 1977; Blandford & Payne 1982), a notion supported by observations (Marscher et al. 2008). This begets the question whether the jet would follow a path twisted into a helix as well. In the late 1980s, a bimodal distribution in the misalignment angles[1] of jets in core-dominated radio sources was discovered (Pearson & Readhead 1988). The misalignments were preferentially small (near 0

[1]The difference between position angles of small scale jet structure measured with VLBI (Very Long Baseline Interferometry) and large scale jet structure measured with the VLA (Very Large Array).

degrees) or nearly perpendicular (near 90 degrees). This observation was further confirmed as more data became available (Wehrle et al. 1992).

The distribution could not be satisfactorily explained with the simplest possible model: a single kink in the jet. However, around the same time, it was shown that relativistic jets could naturally develop either bulk helical motion or helical features around the jet cone by the action of Kelvin–Helmholtz instability, which is caused by velocity gradients between the jet and the surrounding matter (Hardee 1987). In Conway & Murphy (1993), a gently curving helical jet model was proposed that could reproduce the observed statistical bimodality. Later, in Villata & Raiteri (1999), the helical jet model was refined so that physical parameters could vary along the curved jet, and subsequently applied to the blazar Mkn 501, successfully explaining its different X-ray brightness states. Since then, different helical jet models, both analytic and numerical, have been constructed and compared to observations of relativistic jets from objects such as 3C 120 (Hardee 2003; Hardee et al. 2005), M87 (Hardee & Eilek 2011) and S5 0836+710 (Perucho et al. 2012).

5.3 The case of OJ287

As OJ287 is a blazar, the current understanding is that we are looking almost directly down one of the jets in the system. Thus, the emission from OJ287 is very much dominated by the jet and the emission mechanisms discussed above. The exception to this are the giant impact flares discussed in Chapter 4.

The existence of a binary black hole in OJ287 immediately suggests the possibility that the periodic perturbation of the companion could cause the jet to deform helically. Both the 12 year cycle of the binary orbit and the first harmonic of the Kozai resonance[2] at the inner edge of the primary accretion disk at a period of 60 years are evident in the optical data. One

[2]The Kozai resonance (Kozai 1962) occurs in a situation where in a binary of massive bodies on a circular orbit, there is a test mass on a stable orbit around one of the bodies, with orbital separation much less than that of the massive bodies. This test mass is then periodically perturbed by the other massive body of the binary. When the orbit of the test mass has a sufficiently high inclination, its eccentricity can increase to a high value even if the initial eccentricity is arbitrarily small. In the case of OJ287, the test mass is a parcel of gas at the inner edge of the accretion disk, and the binary is comprised of the two supermassive black holes.

would thus expect them to make an appearance in the radio data as well.

Indeed, measurements of optical polarization and radio jet position angle at cm and mm scales have shown time varying behavior, ostensibly related to the binary nature of the system. At cm scales, it is possible to identify the 12 year cycle in the data (Tateyama & Kingham 2004). The amplitudes of the cycle seem modulated, but it would take a longer time interval of radio observations than is available to confirm or exclude the existence of a 60 year modulation period (Valtonen & Wiik 2012). The radio measurements at mm scales also show dramatic variations of the position angle of the jet at timescales compatible with the 12 year period (Agudo et al. 2012; Tateyama 2013). In addition, at the highest resolution scales, the OJ287 jet exhibits a feature resembling double streams, suggestive of a helix (Tateyama 2013).

5.3.1 A helical jet in OJ287

Based on these facts, in Paper V, a helical jet model was fitted to the optical magnitude and polarization and radio position angle data. The model successfully explains the observed optical magnitude and polarization angle variations, as well as the observed radio jet position angle changes at mm and cm wavelengths.

The model was used to produce a density map of the helix projected on the sky, covering the length scales of the expected mm and cm radio emission. This is depicted in Figure 5.3. The resemblance to observations in Tateyama (2013), shown in Figure 5.4, is evident. The specifics of the model are discussed in more detail in Section 6.5.

5.3.2 Secondary jet and short timescale periodicity

In the LV96 binary model, the secondary black hole has periodical collisions with the accretion disk and possibly also with denser clumps of plasma in the accretion disk corona. These collisions cause the secondary to accrete matter, and black hole accretion is intimately linked with launching of relativistic jets.

This recurring accretion suggests that the secondary may also be emitting relativistic jets. As the prevailing magnetic field in the system is likely provided by the accretion disk of the primary, the secondary jet should also be pointed in the same direction as the primary jet (McKinney et al.

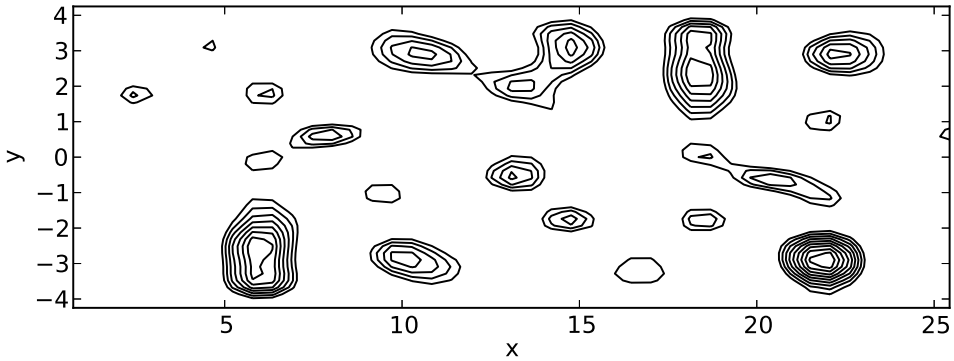

Figure 5.3: A simulated density map of the sky projection of the helical jet in OJ287, spanning several helix wavelengths. The axis of the jet is aligned with the positive x-axis. The unit on both x and y-axis is 0.04 mas, so that the point $x = 5$ ($x = 25$) corresponds to the distance scale of mm (cm) wavelength radio observations. Contours are linearly spaced from zero to maximum density with ten levels in total.

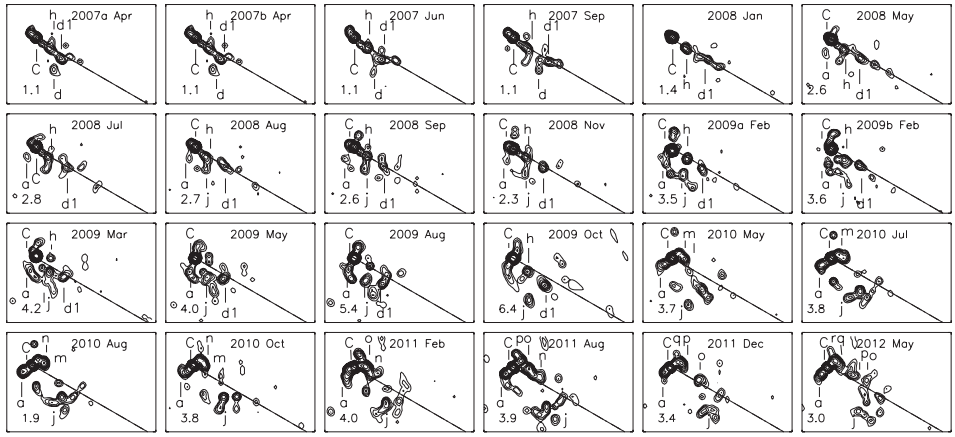

Figure 5.4: 15 GHz VLBA images of OJ287, from April 2007 to May 2012. The peak flux densities of the maps are indicated on the left side of the maps. Contour levels are 1, 2, 4, 8, 16, 32, 64, 128, 256, and 512 × 0.003 Jy beam^{1}. The letter C marks the jet radio core, and the solid line gives the direction of the jet. From September 2008 onwards, the two-streamed appearance of the jet is obvious. Image from Tateyama (2013).

2013). The natural question, then, is whether the secondary jet can have a luminosity high enough to be detected with the primary jet present.

The connection between black hole mass, spin and accretion rate with the luminosity of the jet has long been debated, and the behavior of the jet luminosity over this entire phase space is still not clear (Krolik & Piran 2012; McClintock et al. 2013). The initial analytic estimate in Blandford & Znajek (1977) for jet power P was

$$P \propto \chi^2 \dot{M}, \tag{5.27}$$

where $\chi = J/M^2$ is the dimensionless angular momentum of the black hole and $\dot{M}$ is the accretion rate. A recent result in Tchekhovskoy et al. (2010) is

$$P \sim k\Psi_{\rm tot}^2(\Omega_H^2 + \alpha\Omega_H^4 + \beta\Omega_H^6), \tag{5.28}$$

where $\Psi_{\rm tot}^2$ is the total poloidal magnetic field threading the event horizon, $\Omega_H = \chi/(2Mr_H)$ is the angular velocity of the black hole, $r_H = M + M[1-(\chi/M)^2]^{1/2}$ is the event horizon radius, $\alpha = 1.38$, $\beta = -9.2$ and k is a small constant depending on the field configuration. Here the fourth order coefficient α was obtained from an analytic solution, but the sixth order coefficient was found by fitting to numerical simulations. With numerical simulations Neilsen et al. (2011) found

$$P = 0.87\left(\frac{\Omega_H(\chi)}{\Omega_H(0.6)}\right)^2 L_{43}(M_8 B_4)^2, \tag{5.29}$$

where $L_{43} = 10^{43}$ ergs^{-1}, $M_8 = M/10^8\ M_\odot$ and $B_4 = B/10^4$ G. Sądowski et al. (2013) found a similar scaling with Ω_H, reaffirming the original result in Blandford & Znajek (1977). Thus, despite the lack of exact results, it is clear that the black hole spin is a crucial factor in the power of the relativistic jet.

The mass ratio of the OJ287 components is $\sim 1/100$, but the primary spin in the binary model is only $\chi_1 \sim 0.28$, obtained from fitting the model to the observed timings of the outbursts (Valtonen et al. 2010b,a). The secondary, however, experiences periodical accretion from a rotating shear flow in the primary's accretion disk. As shown in Paper II, this is likely to result in the secondary having a high spin value. If the secondary spin $\chi_2 \sim 1$, then by the previous discussion, and considering that the Doppler factors

are likely to be similar for both primary and secondary, the secondary can reasonably be expected to outshine a quiescent primary. This mechanism could also power the precursor outbursts mentioned in Section 4.3.

To directly observe the existence of a secondary jet in OJ287 requires observations at higher resolutions than are currently available. An indirect way to differentiate between the jets is periodicity analysis. Quasiperiodic variations in black hole sources have been linked with accretion disk rotational velocity near the innermost stable circular orbit (ISCO) of the disk (Merloni et al. 1999). The radius of the ISCO and the corresponding orbital and quasiperiodic oscillation frequencies depend on the black hole mass and spin. This modulation may then be observable as a re-emission in the jet. Observing these frequencies would allow detecting the presence of the secondary indirectly.

The ISCO on the equatorial plane of a Kerr–Newman metric is at a coordinate distance of (Bardeen et al. 1972)

$$r_{\mathrm{ISCO}} = \frac{GM}{c^2}\left(3 + Z_2 \mp \sqrt{(3 - Z_1)(3 + Z_1 + 2Z_2)}\right), \tag{5.30}$$

where a positive (negative) sign corresponds to a retrograde (prograde) orbit with respect to the black hole spin, and

$$Z_1 = 1 + (1 - \chi^2)^{1/3}[(1 + \chi)^{1/3} + (1 - \chi)^{1/3}] \tag{5.31}$$

$$Z_2 = \sqrt{3\chi^2 + Z_1^2}. \tag{5.32}$$

The orbital period P for a test particle on a prograde orbit at a coordinate distance r is (Bardeen et al. 1972)

$$P = 2\pi\left(\sqrt{\frac{r^3}{GM}} + \frac{GM}{c^3}\chi\right) = \frac{2\pi r_{\mathrm{Sch}}}{c}\left[\sqrt{2}\left(\frac{r}{r_{\mathrm{Sch}}}\right)^{3/2} + \frac{1}{2}\chi\right]. \tag{5.33}$$

The prograde ISCO for the primary is then at $r \sim 2.52 r_{\mathrm{pri}}$ and the corresponding orbital period is $P_1 \sim 70$ days assuming a primary spin of $\chi_1 \sim 0.28$. For the secondary, the ISCO is at $r \sim 0.618 r_{\mathrm{sec}}$ and the timescale is $P_2 \sim 3$ hours, assuming the maximal value (Thorne 1974) of $\chi_2 = 0.998$. Corrected for the redshift $z = 0.306$, the observed values become $P_1 \sim 100$ days and $P_2 \sim 4$ hours.

A periodicity of ~ 50 days in the optical data of OJ287 was proposed

in Wu et al. (2006) and further analyzed in Valtonen et al. (2012). In Paper IV, using new and independent data, this periodicity was confirmed to be statistically significant, and was proposed to be linked to the orbital timescale at the ISCO of the primary black hole.

The possible periodicity, P_2, related to the secondary ISCO has a much higher frequency, and likely is also weaker in amplitude. For a positive detection, an extended set of observations with high frequency and high signal–to–noise ratio is required. The observations should also be done when the primary is quiescent, or during a precursor outburst, during which the secondary is near maximum luminosity if the precursor model of Paper III is correct. An observation campaign capturing a precursor outburst with high frequency observations would make possible both the indirect detection of the secondary, or the secondary jet, and the verification of the precursor model.

Chapter 6

Summary of publications

The research articles of this thesis explore the OJ287 system with a variety of approaches, in the context of a binary black hole model. Paper I studies new optical data obtained from astronomical plate archives. In Paper II, the secondary outbursts and spin-up are analyzed on theoretical grounds. In Paper III, a more detailed analysis of the secondary outbursts is presented, along with new data. Paper IV contains a periodicity analysis of OJ287 data focusing on short periods. Paper V explores the likely case of the OJ287 jet being helical in nature. Here the work is presented, and the author's personal contributions to each article are discussed at the end of each section.

6.1 Paper I

Paper I documents the analysis of new OJ287 optical light curve data points found searching the Harvard College Observatory photographic plate archives. Plates containing OJ287 were located, and the modified Argelander method was used to visually estimate the brightness of OJ287 using comparison stars as a guide.

The new data points obtained in this manner span an interval from the late 1890's to the 1980's. In particular, data points for the outburst in 1900 were reported for the first time, and the rising part of the 1913 outburst was also documented for the first time. The new and existing data points for the 1913 outburst are shown in Figure 6.1, as well as the fiducial lightcurve of the impact outburst, from equation (4.10).

Using this data, it was found that the observational timing of the 1913 outburst at 1912.96 agrees well with the predictions in Valtonen et al.

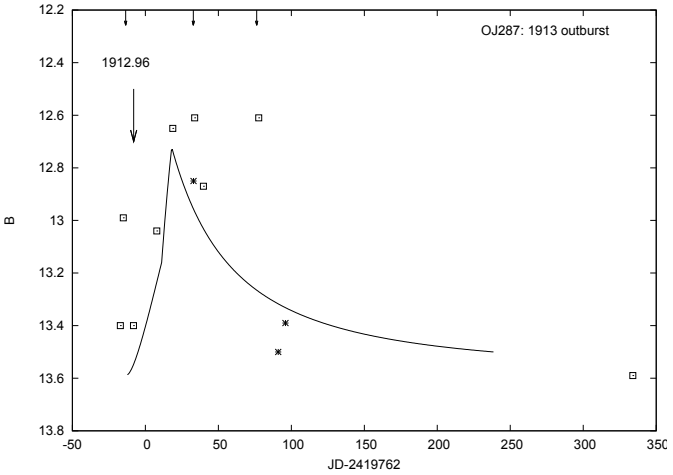

Figure 6.1: B-band light curve of the 1913 flare in OJ287, with the estimated timing of the flare (1912.96) indicated by an arrow. The new (old) data points are indicated by squares (stars). The solid line is the theoretical light curve from equation (4.10), scaled to a duration of approximately 46 days. The three small arrows indicate the timings of additional flares, separated by ~ 50 days, discussed in more detail in Paper I.

(2010b) and Valtonen et al. (2011b), and the outburst length is compatible with the LV96 prediction. The observations were compared to results from a numerical simulation of the OJ287 system. The simulations corroborate the observational fact that the 1913 outburst was caused by an accretion disk impact, while the 1900 outburst was likely a tidal outburst and caused by the increased accretion rate of primary. The simulated accretion rate of the primary black hole, together with the data and the theoretical outburst timings, are shown in Figure 6.2. The increase in the accretion rate of the primary matches the 1900 outburst very well, but the subsequent rises in the flux must be caused by the accretion disk impacts. The findings strongly support the need for precession in binary models of OJ287.

Author's contributions to the article were development of the simulation code used to calculate activity of OJ287 during the period spanned by the data, description of the code, and producing figures 5, 8 and 9 of the paper.

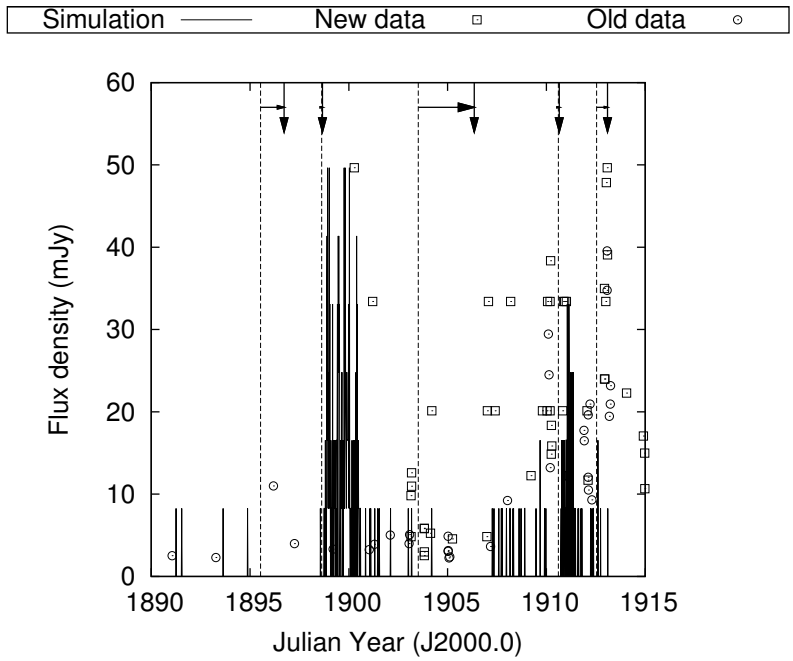

Figure 6.2: Simulated accretion rate of the primary black hole (vertical solid lines, arbitrary scale) compared with the new (old) data points indicated by squares (circles). The dashed vertical lines mark the accretion disk crossings by the secondary, and the vertical arrows mark the theoretical outburst times in the LV96 model. Horizontal arrows indicate the time delays between accretion disk impact and the outburst in the model.

6.2 Paper II

In Paper II, possible outbursts from the secondary component in OJ287 and mechanisms for the spin-up of the secondary were studied. First, precursor outbursts, thus far observed in 1993, 2004 and 2012, were described. These quick optical outbursts seem to happen slightly before the main outburst season after the secondary disk impact. A model was proposed, where these outbursts originate from the secondary component when it accretes matter from the corona of the accretion disk of the primary. This model is the same one that is used in Paper III.

The model requires that the secondary has a high spin that is aligned with the primary spin axis. This paper focuses on the possible astrophysical mechanisms that could have caused this result. First, in the paper, it was shown that the timescale for the secondary to obtain maximal spin is $\sim 10^8$ years. In this estimate, only accretion from the impacts with the primary's accretion disk were taken into account. Next, the effect of Lense–Thirring precession on the secondary spin alignment with the angular momentum vector of the primary accretion disk was examined. This effect causes the angular momentum vector of a test particle orbiting a spinning black hole to precess (Wilkins 1972). For black holes with accretion disks, this effect works to align the plane of the inner accretion disk perpendicularly to the black hole spin axis (Bardeen & Petterson 1975). During this process, called the Bardeen–Petterson effect, the viscous friction in the disk resisting this alignment causes a corresponding torque to be exerted on the black hole spin. In the case of OJ287, this would tend to align the secondary spin with the rotation axis of the primary accretion disk. In the paper, an alignment timescale of $\sim 10^7$ years was obtained. Finally, the timescale for the alignment of the secondary spin with the prevailing magnetic field direction in the OJ287 system was estimated to be $\sim 10^4$ years.

The results in the paper show that a high spin value for the secondary component in OJ287 is to be expected, supporting the precursor outburst model of Paper II and III. In addition, it was shown that the direction of the secondary spin is most likely determined by the magnetic field in the OJ287 system.

The author was solely responsible for the work towards the publication.

6.3 Paper III

Paper III presents new observations of OJ287 from 2010 to 2012 from several observatories. These data points span a new precursor outburst in March 2012, bringing the number of observed precursor outbursts to three.

The paper first describes in detail the observations done at Tuorla Observatory, Astronomical Observatory of Capannori, Astronomical Observatory of Jagiellonian University, Mount Suhora Observatory, University of Athens, Mount Cuba Observatory, Mount Abu Infrared Observatory, Liverpool Telescope and Kungliga Vetenskapliga Akademien Telescope.

Next, the known precursor outbursts were studied in detail. The pre-

cursors seem to happen when the secondary is at a certain distance above the level of the accretion disk of the primary. This is demonstrated in Figure 6.3, where the numerical orbit of the black hole binary is shown, together with the positions corresponding to the precursor timings. The theoretical possibilities for this coincidence were discussed, with tidal perturbation by the secondary as a cause for the precursors investigated in detail. Tidal perturbation was, however, ruled out by theoretical arguments and simulation results. Figure 6.4 shows the light curve of OJ287, compared with the simulated accretion flows and vertical escapes from the disk, which are a numerical proxy for the brightening of the primary jet. A particle was considered to have escaped from the disk when its vertical distance from the disk midplane $z = 0$ exceeded a limiting value of $4\sigma_z$, where $\sigma_z = \pi z_0/(2\sqrt{3})$ is the standard deviation of the disk vertical density distribution, and $z_0 = 260$ AU is the disk semiheight. The escaped particles are considered to have migrated to the black hole jet, as discussed in Chapter 5. The figure makes it clear that these processes cannot explain the precursor flares.

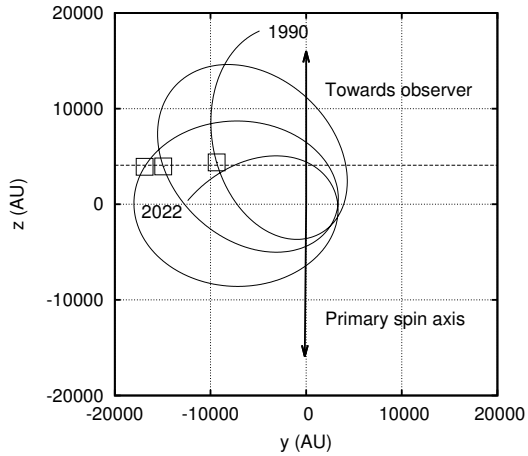

Figure 6.3: Relative orbit of the black hole binary in OJ287 projected to yz-plane. Positions along the orbit corresponding to the timings of the precursor flares are indicated by dotted squares. The primary spin axis and line of sight to Earth are indicated. The accretion disk of the system is in the xy-plane.

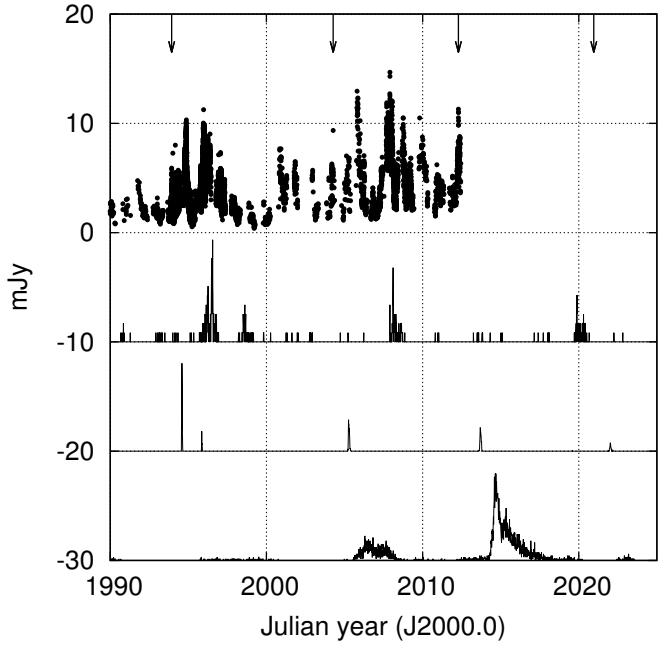

Figure 6.4: V-band light curve of OJ287 from year 1990 (top, in milli-Janskys), together with simulated accretion counts of primary and secondary black holes, and the disk vertical escape count (three lower panels, arbitrary scaling and units, offset by -10, -20 and -30, respectively). Note that the y-axis units are only relevant for the topmost panel. The three historical precursor outbursts, and the one predicted in Paper III, are indicated by arrows.

Instead, a model was constructed where the secondary collides with a cloud of plasma in the corona of the accretion disk of the primary. This collision would lead to increased accretion by the secondary black hole and corresponding increase in jet brightness. The collision scenario was investigated with numerical simulations and a theoretical estimate for the brightness of the secondary during the collision was derived. It was shown that the secondary can reach a brightness equal to or even greater than the primary.

Author's contributions to the paper include most of the writing, ex-

cluding the observational subsections in section 2, producing all figures, and producing the original theoretical estimates.

6.4 Paper IV

Paper IV presents a periodicity analysis of a largely independent set of optical measurements of OJ287. The data points were collected in 2004–2006, spanning two observation seasons and approximately 600 days. Significantly, the data contains several sections measured with high frequency.

Periodicities were searched both from the original data and data binned in one day bins by two methods: The Lomb–Scargle periodogram (LSP) (Lomb 1976; Scargle 1982), and the Weighted Wavelet Z-transform (WWZ) (Foster 1996). The statistical significance of the results obtained by the methods was then ascertained by bootstrapping analysis and, in the case of LSP, an analytic bound was also employed.

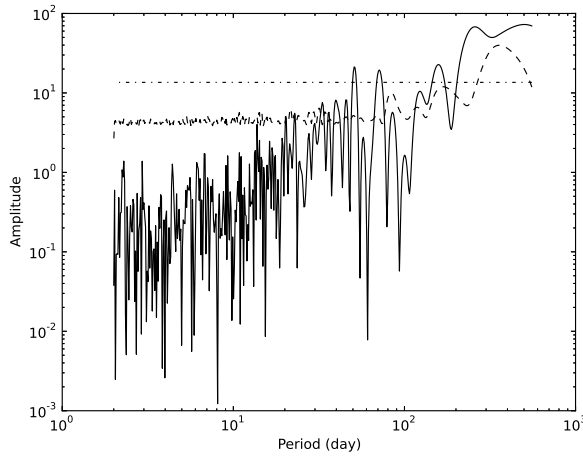

Figure 6.5: Lomb–Scargle periodogram of the entire data set, binned in one-day bins (solid line). Bootstrapped 3σ significance limit is shown by the dashed line, while the Baluev (2008) analytic significance limit is shown by the dash-dotted line.

The LSP yielded peaks at periods of 260, 70 and 50 days, illustrated in Figure 6.5. The WWZ method found a periodicity of 250 days, persisting

throughout the data. The 50 day period was also confirmed, but only found in the first season. The first half of the data, along with the WWZ statistic are shown in Figure 6.6, where the significance of the periodicity can be clearly observed. In the second season, a 70 day periodic component was detected by the WWZ method.

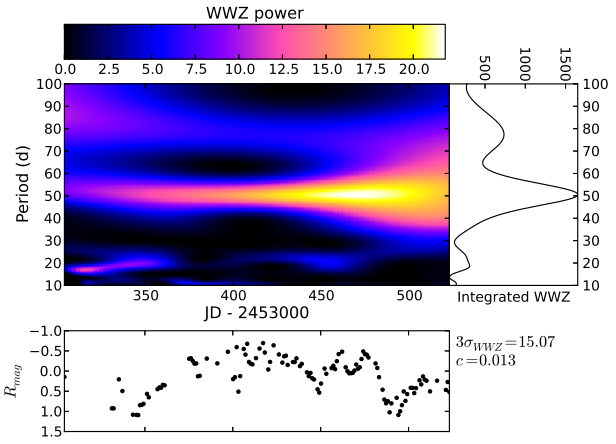

Figure 6.6: The WWZ statistic calculated for the first half of the data, binned in one-day bins (color plot). The WWZ statistic integrated through the data time span is shown on the right, while the input data is shown on the bottom.

The WWZ method was also used to search for higher frequency components in the two most frequently sampled parts of the data set. This yielded detections of periodicities of three and a half and seven days. However, the short time spans of the densely sampled sections of the data make these detections marginal.

The results were analyzed in the context of the binary black hole model. The 250 day period does physically correspond to the half-period around the primary black hole at a distance of $\sim 9r_{\mathrm{Sch}}$, which is just inside the distance at which the secondary typically impacts the primary accretion disk. In the paper, it is argued that the secondary modulation of the primary accretion flow may well cause this periodicity.

The 50 day period is close to the orbital half-period at the r_{ISCO} of the

primary. The paper proposes an argument, in which the found periodicity and its phase-wrapped light curve result from the accretion of spiral density waves in the primary accretion disk. This argument was enhanced by simulating an accretion disk with a spiral density wave with the same code used in Papers I and III. The resulting accretion curves were found to correlate reasonably well with the observations, as can be seen in Figure 6.7, lending credibility to the argument.

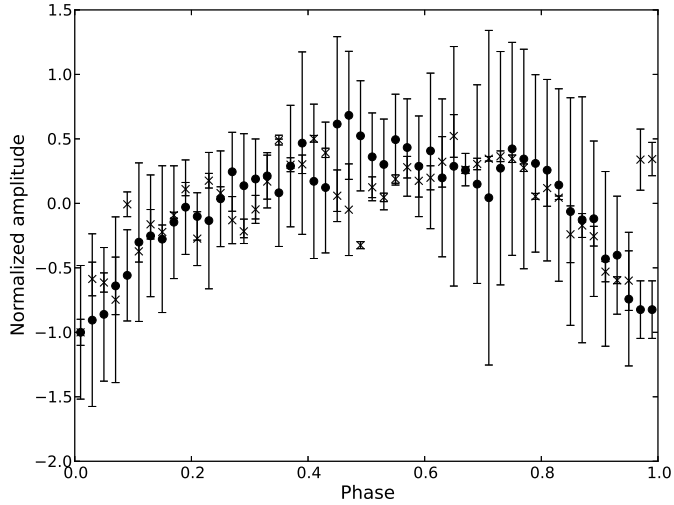

Figure 6.7: Observational data (points), and logarithm of the simulated accretion counts (crosses), phase wrapped with periods scaled to correspond to 50 days at r_{ISCO}, calculated with 50 bins. Normalized bin medians are shown, with 1σ error bars derived from normalized median absolute deviation (Feigelson & Babu 2012).

Author's contributions to the paper are writing majority of the text, development of the used periodicity search and simulation codes, data analysis and all figures of the paper except figure 9.

6.5 Paper V

In Paper V, a helical jet model was proposed to explain the complex nature of the radio jet of OJ287.

The model is based on a jet propagating in an orthogonal direction to the inner edge of the primary black hole's accretion disk. This is in line with the most recent numerical results (McKinney et al. 2013). As the secondary companion black hole perturbs the disk, the disk precesses with a combination of periods of 11.0 years and 116.6 years, as shown by numerical particle simulations. This precession causes the jet to be launched on a helical path.

The optical data was used to constrain the variations in the viewing angle caused by the helicity of the jet, fitting simultaneously the changes in brightness induced by the changing Doppler factor and optical polarization angle. This allowed solving for the half-opening angle θ of the helix cone and the minimum viewing angle ϕ_{min} of the cone axis. The best fit values were determined to be $\theta = 4^{\circ}$ and $\phi_{\mathrm{min}} = 1.8^{\circ}$, with a Lorentz gamma of $\Gamma = 14$. These results constrain the viewing angle and the helix cone opening angle. The time delay between the disk precession and optical polarization angle change was also determined, and found to be 1.4 years.

To solve for the helix wavelength, the resulting model was then applied to the mm and cm wavelength radio data to determine the time delay of the helix propagation. The best fit time delays were found to be 50 and 218 years, respectively, when the least number of multiples of the helix period was preferred. Using these results, the helix propagation velocity was calculated to be $0.85c$, corresponding to $\Gamma = 3.5$, and the wavelength to be 70 pc. The two differing Lorentz factors suggest that the jet either has a spine–sheath structure, with a fast jet having an opening angle $\theta = 0.8^{\circ} \pm 0.4^{\circ}$ (Jorstad et al. 2005) and a slow jet having an opening angle $\theta = 4^{\circ}$, or that the helical feature is a travelling oscillation. In the latter case, the bulk motion of the jet could be different from the model value of $0.85c$.

Author's contributions to the article are typesetting the draft, producing the code calculating the simulated figure 8, and a part of the theoretical calculations.

Chapter 7

Conclusions and future work

7.1 Conclusions

This thesis has focused on deepening our understanding of OJ287, a system that is scientifically important as a likely close binary of supermassive black holes. Such a binary is a sensitive probe for the correct theory of gravitation, independent of the more usual cosmological probes, such as the cosmological microwave background radiation or distant supernovae, and more sensitive than the binary pulsar of Hulse & Taylor (Hulse & Taylor 1975; Valtonen et al. 2011b). The binary, in a natural way, also probes the environment near both black holes, and as such is valuable for understanding the physical processes very close to a supermassive black hole.

One major theme in the papers comprising this thesis has been the role of the secondary black hole in the system. Papers II and III lay a theoretical basis for the observability and characteristics of the secondary emission and compare it to data from the precursor outbursts. In particular, in Paper II, it was determined that it is likely for the secondary black hole to have a high spin in a system like OJ287. In Paper III, this is used to argue for a model where the precursor outbursts originate from the secondary, instead of the primary black hole. In addition, the observable characteristics, such as timescales, of the secondary emission are derived. Paper IV adds to this analysis by directly searching one densely observed data set for possible signs of the secondary emission. The effect of the secondary is also discussed in Paper V, where the secondary is found to be the natural source for the helical behaviour of the relativistic jet of the primary.

Apart from the above, in Paper I, new historical data points have been used to further constrain possible binary black hole models, and to find the LV96 model agreeing well with the historical data. In Paper IV, several

periodicities higher in frequency than the already established 12 year and 60 year periods were confirmed. It was also demonstrated that these periods relate naturally to the physical periodicities in the binary black hole system. Finally, in Paper V, a helical jet model was successfully fit to the combined optical and radio data of the OJ287 system, with the parameters of the helix derived for the first time.

The introduction to this thesis is a somewhat comprehensive review of the characteristics of OJ287 and close binaries of supermassive black holes in general. In particular, the general relativistic orbital mechanics of a binary black hole are discussed in some detail, since most natural frequencies, in such a binary, are related to the orbit. The LV96 binary black hole model of OJ287 is discussed next, with a focus on the optical outbursts which are the most critical element of the model. Finally, the characteristics of a relativistic jet of a binary black hole are reviewed, with an emphasis on helical jets. The jet itself merits a dedicated mention being the primary source of observed radiation for a BL Lac system like OJ287, and the helical structure on the other hand is directly related to the binary character of the system.

7.2 Future work

OJ287 is an unique and important object and certainly merits further study. A natural continuation of the research done on the system so far is the collection of high quality data in all wavebands. Particularly high cadence optical data would be of great importance, partly due to the already existing length of the light curve, but also due to the fact that the majority of the models are most severely restricted by optical measurements. This, in turn, translates to sharper limits for estimates of physical parameters. Furthermore, the longer the light curve is, the more sure we can be of the perpetual nature of the 12-year and the 60-year periodicities.

A particular need exists for continuous high cadence (intraday) optical observations spanning at least several weeks. Such observations are, at the moment, possibly the best way to directly confirm the presence of the secondary black hole, and independently estimate its mass and spin. A campaign of this sort should preferably be timed to span a precursor outburst, or during a very low activity phase, to maximize the possibility of detecting a signal from the secondary black hole.

In addition to observations, there is also much work remaining in simulating the OJ287 system. A definitive full 3D general relativistic magnetohydrodynamics (GRMHD) simulation of the binary and the accretion disks therein remains to be done. Such a simulation would likely give many answers concerning the impact outbursts, characteristics of accretion and behaviour of relativistic jets in the system. On a smaller scale, a full 3D-MHD simulation of the accretion disk impact using the LV96 parameters would nicely complement the analyses in Lehto & Valtonen (1996) and Ivanov et al. (1998). More comprehensive simulations are also needed of the secondary impacts proposed as the source of the precursor outbursts in Paper III.

Other various, but rather specific, pieces of work also remain to be completed. In Lehto & Valtonen (1996), it is mentioned that the shocked plasma from the accretion disk impacts likely radiates optical line emission. The timing windows and the consequent limits for impact models have not been derived yet. Work towards this problem would also likely include radiative simulations of the shocked plasma to more completely understand the situation.

In the more distant future, a natural goal would be to apply spaceborne VLBI missions to separate the binary components and directly observe the binary behavior, a great scientific accomplishment. Achieving this is not entirely unlikely since the projected size of the binary orbit in the LV96 model is just outside current VLBI capabilities.

Appendix A

Appendices

A.1 Post–Newtonian coefficients

Section 3.3.3 introduced the Post–Newtonian terms $\vec{A}_i$ as perturbations to the usual Keplerian equation of motion in equation (3.62). To quantify these terms, we first note that they can be expanded to (Mora & Will 2004)

$$\vec{A}_i = A_i \vec{n} + B_i \vec{v}, \tag{A.1}$$

where $\vec{n} = \vec{r}/r$, $\vec{v} = \mathrm{d}\vec{r}/\mathrm{d}t$ and $\vec{r} = \vec{x_1} - \vec{x_2}$ is the binary relative position. The complete list of the coefficients A_i and B_i up to 3.5PN order is then (using $c = G = 1$) (Mora & Will 2004)

$$A_1 = 2(2+\eta)\frac{m}{r} - (1+3\eta)v^2 + \frac{3}{2}\eta\dot{r}^2 \tag{A.2}$$

$$\begin{aligned} A_2 = &-\frac{3}{4}(12+29\eta)\left(\frac{m}{r}\right)^2 - \eta(3-4\eta)v^4 \\ &- \frac{15}{8}\eta(1-3\eta)\dot{r}^4 + \frac{1}{2}\eta(13-4\eta)\frac{m}{r}v^2 \\ &+ (2+25\eta+2\eta^2)\frac{m}{r}\dot{r}^2 + \frac{3}{2}\eta(3-4\eta)v^2\dot{r}^2 \end{aligned} \tag{A.3}$$

$$A_{2.5} = \frac{8}{5}\eta\frac{m}{r}\dot{r}\left(\frac{17}{3}\frac{m}{r} + 3v^2\right) \tag{A.4}$$

$$
\begin{aligned}
A_3 = &\left[16 + \left(\frac{1399}{12} - \frac{41}{16}\pi^2\right)\eta + \frac{71}{2}\eta^2\right]\left(\frac{m}{r}\right)^3 \\
&+ \eta\left[\frac{20827}{840} + \frac{123}{64}\pi^2 - \eta^2\right]\left(\frac{m}{r}\right)^2 v^2 \\
&- \left[1 + \left(\frac{22717}{168} + \frac{615}{64}\pi^2\right)\eta + \frac{11}{8}\eta^2 - 7\eta^3\right]\left(\frac{m}{r}\right)^2 \dot{r}^2 \\
&- \frac{1}{4}\eta(11 - 49\eta + 52\eta^2)v^6 + \frac{35}{16}\eta(1 - 5\eta + 5\eta^2)\dot{r}^6 \\
&- \frac{1}{4}\eta(75 + 32\eta - 40\eta^2)\frac{m}{r}v^4 - \frac{1}{2}\eta(158 - 69\eta - 60\eta^2)\frac{m}{r}\dot{r}^4 \\
&+ \eta(121 - 16\eta - 20\eta^2)\left(\frac{m}{r}\right)^2 \dot{r}^2 \\
&+ \frac{3}{8}\eta(20 - 79\eta + 60\eta^2)v^4\dot{r}^2 \\
&- \frac{15}{8}\eta(4 - 18\eta + 17\eta^2)v^2\dot{r}^4
\end{aligned} \tag{A.5}
$$

$$
\begin{aligned}
A_{3.5} = &-\frac{8}{5}\eta\frac{m}{r}\dot{r}\left[\frac{23}{14}(43 + 14\eta)\left(\frac{m}{r}\right)^2 + \frac{3}{28}(61 + 70\eta)v^4\right. \\
&+ 70\dot{r}^4 + \frac{1}{42}(519 - 1267\eta)\left(\frac{m}{r}\right)v^2 \\
&\left.+ \frac{1}{4}(147 + 188\eta)\left(\frac{m}{r}\right)\dot{r}^2 - \frac{15}{4}(19 + 2\eta)v^2\dot{r}^2\right]
\end{aligned} \tag{A.6}
$$

$$
B_1 = 2(2 - \eta)\dot{r} \tag{A.7}
$$

$$
B_2 = -\frac{1}{2}\dot{r}\left[(4 + 41\eta + 8\eta^2)\left(\frac{m}{r}\right) - \eta(15 + 4\eta)v^2 + 3\eta(3 + 2\eta)\dot{r}^2\right] \tag{A.8}
$$

$$
B_{2.5} = -\frac{8}{5}\eta\frac{m}{r}\left(3\frac{m}{r} + v^2\right) \tag{A.9}
$$

$$
\begin{aligned}
B_3 = &\dot{r}\left\{\left[4 + \left(\frac{5849}{840} + \frac{123}{32}\pi^2\right)\eta - 25\eta^2 - 8\eta^3\right]\left(\frac{m}{r}\right)^2\right. \\
&+ \frac{1}{8}\eta(65 - 152\eta - 48\eta^2)v^4 + \frac{15}{8}\eta(3 - 8\eta - 2\eta^2)\dot{r}^4 \\
&\left.+ \eta(15 + 27\eta + 10\eta^2)\frac{m}{r}v^2 - \frac{1}{6}\eta(329 + 177\eta + 108\eta^2)\frac{m}{r}\dot{r}^2\right.
\end{aligned}
$$

$$- \frac{3}{4}\eta(16 - 37\eta - 16\eta^2)v^2\dot{r}^2\Bigg\} \tag{A.10}$$

$$\begin{aligned} B_{3.5} = \frac{8}{5}\eta\frac{m}{r}\Bigg[&\frac{1}{42}(1325 + 546\eta)\left(\frac{m}{r}\right)^2 + \frac{1}{28}(313 + 42\eta)v^4 \\ &+ 75\dot{r}^4 - \frac{1}{42}(205 + 777\eta)\frac{m}{r}v^2 + \frac{1}{12}(205 + 424\eta)\frac{m}{r}\dot{r}^2 \\ &- \frac{3}{4}(113 + 2\eta)v^2\dot{r}^2\Bigg], \end{aligned} \tag{A.11}$$

where $m = m_1 + m_2$ is the total mass of the system, $\eta = m_1 m_2/m^2$ is the symmetric mass ratio, $v = \|\vec{v}\|$ and $\dot{r} = \vec{v}\cdot\vec{r}/r$.

Section 3.3.3 also introduced the spin–orbit (SO), spin–spin (SS) and quadrupole–monopole (Q) interaction terms in equations (3.63) and (3.64). Written out, these read (Barker & O'Connell 1975, 1979; Kidder 1995)

$$\begin{aligned} \vec{A}_{\mathrm{SO}} = \frac{1}{r}\Bigg\{&6\vec{n}\left[(\vec{n}\times\vec{v})\cdot\left(2\vec{S} + \frac{\delta m}{m}\vec{\Delta}\right)\right] \\ &- \left[\vec{v}\times\left(7\vec{S} + \frac{3\delta m}{m}\vec{\Delta}\right)\right] + 3\dot{r}\left[\vec{n}\times(3\vec{S} + \frac{\delta m}{m}\vec{\Delta})\right]\Bigg\} \end{aligned} \tag{A.12}$$

$$\vec{A}_{\mathrm{Q}} = -q\chi_1^2\frac{3}{2}\frac{mm_1^2}{r^4}\left\{\left[1 - 5(\vec{s}_1\cdot\vec{n})^2\right]\vec{n} + 2(\vec{s}_1\cdot\vec{n})\vec{s}_1\right\} \tag{A.13}$$

$$\begin{aligned} \vec{A}_{\mathrm{SS}} &= -\frac{3}{r^4}\frac{1}{m\eta}\Big[\vec{n}(\vec{S}_1\cdot\vec{S}_2) + \vec{S}_1(\vec{n}\cdot\vec{S}_2) + \vec{S}_2(\vec{n}\cdot\vec{S}_1) \\ &\qquad - 5\vec{n}(\vec{n}\cdot\vec{S}_1)(\vec{n}\cdot\vec{S}_2)\Big] \\ &= -\frac{3\eta m^3}{r^4}\chi_1\chi_2\Big[\vec{n}(\vec{s}_1\cdot\vec{s}_2) + \vec{s}_1(\vec{n}\cdot\vec{s}_2) + \vec{s}_2(\vec{n}\cdot\vec{s}_1) \\ &\qquad - 5\vec{n}(\vec{n}\cdot\vec{s}_1)(\vec{n}\cdot\vec{s}_2)\Big] \end{aligned} \tag{A.14}$$

$$\vec{\Omega}_{\mathrm{SO}} = \frac{1}{r^2}\left(2 + \frac{3m_2}{2m_1}\right)\eta m(\vec{n}\times\vec{v}) = \frac{m\eta}{2r^2}\left(\frac{7 + \sqrt{1-4\eta}}{1 + \sqrt{1-4\eta}}\right)(\vec{n}\times\vec{v}) \tag{A.15}$$

$$\vec{\Omega}_{\mathrm{Q}} = \frac{m^2\eta}{r^3}q\chi_1\left(3(\vec{s}_1\cdot\vec{n})\vec{n} - \vec{s}_1\right) \tag{A.16}$$

$$\vec{\Omega}_{\rm SS} = \frac{m_2^2 \chi_2}{r^3} \left(3(\vec{s}_2 \cdot \vec{n})\vec{n} - \vec{s}_2\right), \tag{A.17}$$

where $\vec{S}_i = m_i^2 \chi_i \vec{s}_i$ are the spin angular momenta of the black holes, and we have adopted $\vec{S} = \vec{S}_1 + \vec{S}_2$, $\vec{\Delta} = m(\vec{S}_2/m_2 - \vec{S}_1/m_1)$ and $\delta m = m_2 - m_1$ from Kidder (1995). We have also introduced the parameter q, which parametrizes the black hole quadrupole momentum $Q_1 = q\|\vec{S}_1\|^2/m_i$. The equations are for body 1, and the equations for body 2 can be obtained by a switch of indexes. In GR $q = 1$, and solving q from observations is thus a test of the so-called *black hole no-hair theorem*. See Section 3.4.4, and Valtonen et al. (2010b) and Valtonen et al. (2011b) for tests with OJ287.

Bibliography

Abdo, A. A., Ackermann, M., Agudo, I., et al. 2010, ApJ, 716, 30

Abramowicz, M. A., Czerny, B., Lasota, J. P., & Szuszkiewicz, E. 1988, ApJ, 332, 646

Agudo, I., Marscher, A. P., Jorstad, S. G., et al. 2012, ApJ, 747, 63

Antoniadis, J., Freire, P. C. C., Wex, N., et al. 2013, Science, 340, 448

Antonucci, R. 1993, ARA&A, 31, 473

Arnett, W. D. 1980, ApJ, 237, 541

Bai, S. 1966, Radiation gas dynamics (Springer-Verlag)

Balbus, S. A. & Hawley, J. F. 1991, ApJ, 376, 214

Baluev, R. V. 2008, MNRAS, 385, 1279

Band, D. L. & Grindlay, J. E. 1985, ApJ, 298, 128

Band, D. L. & Grindlay, J. E. 1986, ApJ, 308, 576

Barack, L. 2009, Classical and Quantum Gravity, 26, 213001

Bardeen, J. M. & Petterson, J. A. 1975, ApJ, 195, L65

Bardeen, J. M., Press, W. H., & Teukolsky, S. A. 1972, ApJ, 178, 347

Barker, B. M. & O'Connell, R. F. 1975, Phys. Rev. D, 12, 329

Barker, B. M. & O'Connell, R. F. 1979, General Relativity and Gravitation, 11, 149

Begelman, M. C., Volonteri, M., & Rees, M. J. 2006, MNRAS, 370, 289

Benson, A. J. 2010, Phys. Rep., 495, 33

Bietenholz, M. F., Bartel, N., & Rupen, M. P. 2000, ApJ, 532, 895

Bini, D. & Damour, T. 2013, Phys. Rev. D, 87, 121501

Blanchet, L. 2006, Living Reviews in Relativity, 9, 4, URL (cited on 2014-02-01): http://www.livingreviews.org/lrr-2006-4

Blandford, R. D. & Payne, D. G. 1982, MNRAS, 199, 883

Blandford, R. D. & Znajek, R. L. 1977, MNRAS, 179, 433

Blumenthal, G. R. & Gould, R. J. 1970, Reviews of Modern Physics, 42, 237

Bondi, H. 1952, MNRAS, 112, 195

Bondi, H. & Hoyle, F. 1944, MNRAS, 104, 273

Bridle, A. H. 1982, in IAU Symposium, Vol. 97, Extragalactic Radio Sources, ed. D. S. Heeschen & C. M. Wade, 121–128

Broderick, A. E., Johannsen, T., Loeb, A., & Psaltis, D. 2013, ArXiv e-prints, [arXiv:1311.5564]

Bulirsch, R. & Stoer, J. 1966, Numerische Mathematik, 8, 1

Byrd, G. G., Sundelius, B., & Valtonen, M. 1987, A&A, 171, 16

Byrd, G. G., Valtonen, M. J., Valtaoja, L., & Sundelius, B. 1986, A&A, 166, 75

Böttcher, M. & Dermer, C. D. 2002, ApJ, 564, 86

Carrasco, L., Dultzin-Hacyan, D., & Cruz-Gonzalez, I. 1985, Nature, 314, 146

Carroll, S. 2004, Spacetime and Geometry: An Introduction to General Relativity (Addison-Wesley)

Chandrasekhar, S. 1943, ApJ, 97, 255

Chandrasekhar, S. 1983, The Mathematical Theory of Black Holes, The International Series of Monographs on Physics (Oxford: Clarendon Press)

Cohen, M. H. & Unwin, S. C. 1982, in IAU Symposium, Vol. 97, Extragalactic Radio Sources, ed. D. S. Heeschen & C. M. Wade, 345–353

Conway, J. E. & Murphy, D. W. 1993, ApJ, 411, 89

Craine, E. R. & Warner, J. W. 1973, ApJ, 179, L53

Detweiler, S. 2005, Classical and Quantum Gravity, 22, 681

Dickel, J. R., Yang, K. S., McVittie, G. C., & Swenson, Jr., G. W. 1967, AJ, 72, 757

Eisenhauer, F., Perrin, G., Brandner, W., et al. 2011, The Messenger, 143, 16

Fanaroff, B. L. & Riley, J. M. 1974, MNRAS, 167, 31P

Feigelson, E. & Babu, G. 2012, Modern Statistical Methods for Astronomy: With R Applications (Cambridge University Press)

Felice, A. D. & Tsujikawa, S. 2010, Living Reviews in Relativity, 13, 3, URL (cited on 2014-02-01): http://www.livingreviews.org/lrr-2010-3

Ferrarese, L. & Ford, H. 2005, Space Sci. Rev., 116, 523

Ferreira, J. & Pelletier, G. 1995, A&A, 295, 807

Feynman, R. P. 1964, Feynman Lectures on Physics. Volume 2: Mainly Electromagnetism and Matter (Addison-Wesley)

Foffa, S. & Sturani, R. 2013, Phys. Rev. D, 87, 064011

Foster, G. 1996, AJ, 112, 1709

Freire, P. C. C., Wex, N., Esposito-Farèse, G., et al. 2012, MNRAS, 423, 3328

Frohlich, A., Goldsmith, S., & Weistrop, D. 1974, MNRAS, 168, 417

Gallouin, L., Nakano, H., Yunes, N., & Campanelli, M. 2012, Classical and Quantum Gravity, 29, 235013

Gendre, M. A., Best, P. N., Wall, J. V., & Ker, L. M. 2013, MNRAS, 430, 3086

Ghisellini, G., Maraschi, L., & Treves, A. 1985, A&A, 146, 204

Ghisellini, G., Tavecchio, F., & Ghirlanda, G. 2009, MNRAS, 399, 2041

Ginzburg, V. L. & Syrovatskii, S. I. 1965, ARA&A, 3, 297

Goodman, J. 1993, ApJ, 406, 596

Gragg, W. B. 1965, Journal of the Society for Industrial & Applied Mathematics, Series B: Numerical Analysis, 2, 384

Gray, R. H. 1994, Icarus, 112, 485

Hardee, P. E. 1987, ApJ, 318, 78

Hardee, P. E. 2003, ApJ, 597, 798

Hardee, P. E. & Eilek, J. A. 2011, ApJ, 735, 61

Hardee, P. E., Walker, R. C., & Gómez, J. L. 2005, ApJ, 620, 646

Hawking, S. W. 1972a, Communications in Mathematical Physics, 25, 152

Hawking, S. W. 1972b, Communications in Mathematical Physics, 25, 167

Heidt, J., Nilsson, K., Appenzeller, I., et al. 1999, A&A, 352, L11

Heinz, S. & Sunyaev, R. A. 2003, MNRAS, 343, L59

Hellström, C. & Mikkola, S. 2010, Celestial Mechanics and Dynamical Astronomy, 106, 143

Homan, D. C., Kadler, M., Kellermann, K. I., et al. 2009, ApJ, 706, 1253

Horbatsch, M. W. & Burgess, C. P. 2012, J. Cosmology Astropart. Phys., 5, 10

Hugoniot, H. 1889, J. Ecole Polytechnique, 58, 1

Hulse, R. A. & Taylor, J. H. 1975, ApJ, 195, L51

Hunt, R. 1971, MNRAS, 154, 141

Israel, W. 1967, Physical Review, 164, 1776

Israel, W. 1968, Communications in Mathematical Physics, 8, 245

Ivanov, P. B., Igumenshchev, I. V., & Novikov, I. D. 1998, ApJ, 507, 131

Iwasawa, M., An, S., Matsubayashi, T., Funato, Y., & Makino, J. 2011, ApJ, 731, L9

Jacobson, T. 1999, Physical Review Letters, 83, 2699

Jauncey, D. L., Niell, A. E., & Condon, J. J. 1970, ApJ, 162, L31

Jorstad, S. G., Marscher, A. P., Lister, M. L., et al. 2005, AJ, 130, 1418

Katz, J. I. 1997, ApJ, 478, 527

Kellermann, K. I. & Pauliny-Toth, I. I. K. 1969, ApJ, 155, L71

Kellermann, K. I. & Pauliny-Toth, I. I. K. 1981, ARA&A, 19, 373

Khan, F. M., Holley-Bockelmann, K., Berczik, P., & Just, A. 2013, ApJ, 773, 100

Kidder, L. E. 1995, Phys. Rev. D, 52, 821

Kidger, M., Takalo, L., Mattei, J., et al. 1993, IAU Circ., 5909, 1

Kidger, M. R., Gonzalez-Perez, J. N., de Diego, J. A., et al. 1995, A&AS, 113, 431

Kidger, M. R. & Takalo, L. O., eds. 1994, Intensive monitoring of OJ 287. Proceedings.

Kino, M., Kawakatu, N., & Takahara, F. 2012, ApJ, 751, 101

Kirillov, O. N. & Stefani, F. 2013, Physical Review Letters, 111, 061103

Kozai, Y. 1962, AJ, 67, 591

Kramer, M., Stairs, I. H., Manchester, R. N., et al. 2006, Science, 314, 97

Kraus, J. D., Scheer, D. J., Dixon, R. S., Fitch, L. T., & Andrew, B. H. 1968, ApJ, 152, L35

Krolik, J. H. & Piran, T. 2012, ApJ, 749, 92

Landau, L. & Lifshitz, E. 1975, The Classical Theory of Fields, Course of Theoretical Physics No. 2 (Butterworth-Heinemann)

Lanyi, G. E., Boboltz, D. A., Charlot, P., et al. 2010, AJ, 139, 1695

Lehto, H. J. & Valtonen, M. J. 1996, ApJ, 460, 207

Li, K.-H., Xie, G.-Z., Bao, C.-X., & Hao, P.-J. 1986, Acta Astronomica Sinica, 27, 137

Lin, D. N. C., Pringle, J. E., & Rees, M. J. 1988, ApJ, 328, 103

Linfield, R. P., Levy, G. S., Ulvestad, J. S., et al. 1989, ApJ, 336, 1105

Livio, M. 1999, Phys. Rep., 311, 225

Lomb, N. R. 1976, Ap&SS, 39, 447

Lousto, C. O. & Zlochower, Y. 2013, Phys. Rev. D, 88, 024001

MacDonald, D. & Thorne, K. S. 1982, MNRAS, 198, 345

Makino, J. & Ebisuzaki, T. 1994, ApJ, 436, 607

Marscher, A. P. 1977, ApJ, 216, 244

Marscher, A. P., Jorstad, S. G., D'Arcangelo, F. D., et al. 2008, Nature, 452, 966

Mayer, L., Kazantzidis, S., Madau, P., et al. 2007, Science, 316, 1874

McClintock, J. E., Narayan, R., & Steiner, J. F. 2013, Space Sci. Rev.

McKinney, J. C. 2005, ApJ, 630, L5

McKinney, J. C. & Blandford, R. D. 2009, MNRAS, 394, L126

McKinney, J. C., Tchekhovskoy, A., & Blandford, R. D. 2013, Science, 339, 49

McNamara, B. R., Kazemzadeh, F., Rafferty, D. A., et al. 2009, ApJ, 698, 594

Medina, R. 2006, Journal of Physics A: Mathematical and Theoretical, 39, 3801

Meier, D. L. 2003, New A Rev., 47, 667

Merloni, A., Vietri, M., Stella, L., & Bini, D. 1999, MNRAS, 304, 155

Merritt, D. 2013, Dynamics and Evolution of Galactic Nuclei, Princeton Series in Astrophysics (Princeton University Press)

Merritt, D., Alexander, T., Mikkola, S., & Will, C. M. 2010, Phys. Rev. D, 81, 062002

Mikkola, S. & Aarseth, S. 2002, Celestial Mechanics and Dynamical Astronomy, 84, 343

Miller, J. S., French, H. B., & Hawley, S. A. 1978, in BL Lac Objects, ed. A. M. Wolfe, 176–187

Miller, R. H. 1976, Journal of Computational Physics, 21, 400

Milosavljević, M. & Merritt, D. 2003, ApJ, 596, 860

Mora, T. & Will, C. M. 2004, Phys. Rev. D, 69, 104021

Nagakura, H., Ito, H., Kiuchi, K., & Yamada, S. 2011, ApJ, 731, 80

Narayan, R. 2005, Ap&SS, 300, 177

Narayan, R. & Yi, I. 1994, ApJ, 428, L13

Neilsen, D., Lehner, L., Palenzuela, C., et al. 2011, Proceedings of the National Academy of Science, 108, 12641

Nemmen, R. S., Bower, R. G., Babul, A., & Storchi-Bergmann, T. 2007, MNRAS, 377, 1652

Nieppola, E., Hovatta, T., Tornikoski, M., et al. 2009, AJ, 137, 5022

Padovani, P. & Giommi, P. 1995, MNRAS, 277, 1477

Padovani, P. & Urry, C. M. 1990, ApJ, 356, 75

Pearson, T. J. & Readhead, A. C. S. 1988, ApJ, 328, 114

Penrose, R. & Rindler, W. 1987, Spinors and Space-Time: Volume 1, Two-Spinor Calculus and Relativistic Fields, Cambridge Monographs on Mathematical Physics (Cambridge University Press)

Perucho, M., Kovalev, Y. Y., Lobanov, A. P., Hardee, P. E., & Agudo, I. 2012, ApJ, 749, 55

Peters, P. C. 1964, Physical Review, 136, 1224

Peters, P. C. & Mathews, J. 1963, Physical Review, 131, 435

Pietilä, H. 1998, ApJ, 508, 669

Poisson, E. 2004, Living Reviews in Relativity, 7, 6, URL (cited on 2014-02-01): http://www.livingreviews.org/lrr-2004-6

Rankine, W. M. 1870, Philosophical transactions of the Royal Society of London, 160, 277

Rieger, F. M. 2004, ApJ, 615, L5

Rybicki, G. & Lightman, A. 1979, Radiative Processes in Astrophysics, Wiley-Interscience (Wiley)

Sakimoto, P. J. & Coroniti, F. V. 1981, ApJ, 247, 19

Savolainen, T., Homan, D. C., Hovatta, T., et al. 2010, A&A, 512, A24

Sądowski, A., Narayan, R., Penna, R., & Zhu, Y. 2013, MNRAS

Scargle, J. D. 1982, ApJ, 263, 835

Schutz, B. 1985, A First Course in General Relativity, Series in physics (Cambridge University Press)

Shakura, N. I. & Sunyaev, R. A. 1973, A&A, 24, 337

Shapiro, I. I. 1964, Physical Review Letters, 13, 789

Shaw, M. S., Romani, R. W., Cotter, G., et al. 2013, ApJ, 764, 135

Sigurdsson, S. & Hernquist, L. 1993, Nature, 364, 423

Sillanpää, A., Haarala, S., Valtonen, M. J., Sundelius, B., & Byrd, G. G. 1988, ApJ, 325, 628

Sillanpää, A., Takalo, L. O., Pursimo, T., et al. 1996a, A&A, 305, L17

Sillanpää, A., Takalo, L. O., Pursimo, T., et al. 1996b, A&A, 315, L13

Sitko, M. L. & Junkkarinen, V. T. 1985, PASP, 97, 1158

Smith, P. S., Balonek, T. J., Heckert, P. A., Elston, R., & Schmidt, G. D. 1985, AJ, 90, 1184

Snellen, I. A. G., McMahon, R. G., Hook, I. M., & Browne, I. W. A. 2002, MNRAS, 329, 700

Sotiriou, T. P. & Faraoni, V. 2012, Physical Review Letters, 108, 081103

Stein, W. A., Odell, S. L., & Strittmatter, P. A. 1976, ARA&A, 14, 173

Stella, L. & Rosner, R. 1984, ApJ, 277, 312

Strittmatter, P. A., Serkowski, K., Carswell, R., et al. 1972, ApJ, 175, L7

Sundelius, B., Wahde, M., Lehto, H. J., & Valtonen, M. J. 1997, ApJ, 484, 180

Svensson, R. & Zdziarski, A. A. 1994, ApJ, 436, 599

Takalo, L. O., Sillanpaeae, A., Nilsson, K., Kidger, M., & de Diego, J. A. 1994, A&AS, 104, 115

Tanaka, T. L. 2013, MNRAS

Tateyama, C. E. 2013, ApJS, 205, 15

Tateyama, C. E. & Kingham, K. A. 2004, ApJ, 608, 149

Tchekhovskoy, A., Narayan, R., & McKinney, J. C. 2010, ApJ, 711, 50

Thompson, J. R., Kraus, J. D., & Andrew, B. H. 1968, ApJ, 154, L1

Thorne, K. S. 1974, ApJ, 191, 507

Urry, C. M. & Padovani, P. 1995, PASP, 107, 803

Valtaoja, E., Teräsranta, H., Tornikoski, M., et al. 2000, ApJ, 531, 744

Valtonen, M., Kidger, M., Lehto, H., & Poyner, G. 2008a, A&A, 477, 407

Valtonen, M. & Sillanpää, A. 2011, Acta Polytechnica, 51, 060000

Valtonen, M. J. 2007, ApJ, 659, 1074

Valtonen, M. J., Ciprini, S., & Lehto, H. J. 2012, MNRAS, 427, 77

Valtonen, M. J. & Lehto, H. J. 1997, ApJ, 481, L5

Valtonen, M. J., Lehto, H. J., Nilsson, K., et al. 2008b, Nature, 452, 851

Valtonen, M. J., Lehto, H. J., Sillanpää, A., et al. 2006a, ApJ, 646, 36

Valtonen, M. J., Lehto, H. J., Takalo, L. O., & Sillanpää, A. 2011a, ApJ, 729, 33

Valtonen, M. J., Mikkola, S., Lehto, H. J., et al. 2011b, ApJ, 742, 22

Valtonen, M. J., Mikkola, S., Lehto, H. J., et al. 2010a, Celestial Mechanics and Dynamical Astronomy, 106, 235

Valtonen, M. J., Mikkola, S., Merritt, D., et al. 2010b, ApJ, 709, 725

Valtonen, M. J., Nilsson, K., Sillanpää, A., et al. 2006b, ApJ, 643, L9

Valtonen, M. J., Nilsson, K., Villforth, C., et al. 2009, ApJ, 698, 781

Valtonen, M. J. & Wiik, K. 2012, MNRAS, 421, 1861

Véron-Cetty, M.-P. & Véron, P. 2010, A&A, 518, A10

Villata, M. & Raiteri, C. M. 1999, A&A, 347, 30

Villata, M., Raiteri, C. M., Sillanpää, A., & Takalo, L. O. 1998, MNRAS, 293, L13

Villforth, C., Nilsson, K., Heidt, J., et al. 2010, MNRAS, 402, 2087

Vincent, F. H., Gourgoulhon, E., & Novak, J. 2012, Classical and Quantum Gravity, 29, 245005

Volonteri, M., Haardt, F., & Madau, P. 2003, ApJ, 582, 559

Wagoner, R. V. 1970, Phys. Rev. D, 1, 3209

Wald, R. M. 1984, General Relativity (University of Chicago Press)

Wang, J.-M., Watarai, K.-Y., & Mineshige, S. 2004, ApJ, 607, L107

Wehrle, A. E., Cohen, M. H., Unwin, S. C., et al. 1992, ApJ, 391, 589

Wenger, M., Ochsenbein, F., Egret, D., et al. 2000, A&AS, 143, 9

Wilkins, D. C. 1972, Phys. Rev. D, 5, 814

Will, C. 1993, Theory and Experiment in Gravitational Physics, 2nd edn. (Cambridge: Cambridge University Press)

Will, C. M. 2008, ApJ, 674, L25

Will, C. M. 2011, Proceedings of the National Academy of Science, 108, 5938

Will, C. M. 2014, ArXiv e-prints, [arXiv:1403.7377]

Williams, P. J. S. 1963, Nature, 200, 56

Worrall, D. M., Puschell, J. J., Jones, B., et al. 1982, ApJ, 261, 403

Wu, J., Zhou, X., Wu, X.-B., et al. 2006, AJ, 132, 1256

Yoshida, H. 1990, Physics Letters A, 150, 262

Younsi, Z., Wu, K., & Fuerst, S. V. 2012, A&A, 545, A13

Zdziarski, A. A. 1986, ApJ, 305, 45

Zensus, J. A., Hough, D. H., & Porcas, R. W. 1987, Nature, 325, 36